Production and morphological and microstructural characterization of bulk composites or thick films for the study of multiphysics interactions

Doctoral Dissertation
Doctoral Program in Materials Science and Technology (29th Cycle)

Production and morphological and microstructural characterization of bulk composites or thick films for the study of multiphysics interactions

By

Pietro Galizia

******

Supervisors:
Prof. Giovanni Maizza, Supervisor
Dr. Carmen Galassi (CNR-ISTEC), Co-Supervisor

Doctoral Examination Committee:
Dr. Algueró Miguel, CSIC of Madrid
Dr. Buscaglia Vincenzo, CNR-ICMATE of Genova
Prof. Palmero Paola, Politecnico di Torino
Prof. Onida Barbara, Politecnico di Torino
Dr. Vinai Franco, INRIM of Torino

Politecnico di Torino
2017

Declaration

I hereby declare that, the contents and organization of this dissertation constitute my own original work and does not compromise in any way the rights of third parties, including those relating to the security of personal data.

Pietro Galizia

2017

* This dissertation is presented in partial fulfillment of the requirements for **Ph.D. degree** in the Graduate School of Politecnico di Torino (ScuDo).

"Che non è impresa da pigliar a gabbo
Descriver bene questo grande intruglio,
Né da lingua che chiami mamma e babbo."

Pellegrino Artusi, 46. *Cuscussù,*
La Scienza in cucina e l'Arte di mangiar bene

-

“That is not a feat to underestimate
Well describing this big concoction,
Nor from a language that cries Mammy and Daddy. "

Pellegrino Artusi, 46. *Cuscussù,*

Science in the Kitchen and the Art of Eating Well

Acknowledgment

The PhD experimental activity was performed at the institute of Science and Technology for Ceramics Materials belonging to the National Research Council of Italy (CNR-ISTEC). I would like to acknowledge the support of Mr. Claudio Capiani (CNR-ISTEC) for conveying to me his skills on the samples preparation and kept my experimental activity practical and efficient without superfluous complications, Dr. Carlo Baldisserri (CNR-ISTEC) for introducing me in the electrophoretic deposition field, for having trained me on the using of his electrical gear for the electrophoretic deposition, and his kind suggestions that helped me to improve the produced manuscripts, Dr. Davide Gardini (CNR-ISTEC) for his support on the suspensions preparation and characterization, Dr. Floriana Craciun (CNR-ISC) and Dr. Francesco Cordero (CNR-ISC) for motivating me to study the Rietveld refinement and giving me an outstanding reference in the studied perovskitic structures, Dr. Mauro Mazzocchi (CNR-ISTEC) and Dr. Angelo Agostino (Turin University) for their kind lessons about the scanning electric microscopy and Rietveld refinement, respectively, Dr. Marin Cernea (INFM) for the preparation of nanopowders by chemical synthesis, the production of samples by spark plasma sintering, the recording of magnetic analyses, and kind lessons about the writing of articles, Mr. Daniele dalle Fabbriche (CNR-ISTEC) for his valuable technical assistance for the thermal treatments, Dr. Franca Albertini (CNR-IMEM), Dr. Franca Casoli (CNR-IMEM), Prof. Liliana Mitoseriu (UAIC), Dr. Cristina Elena Ciomaga (UAIC), Dr. Valentina Mihalache (INFM), Dr. Lucian Diamandescu (INFM), and Dr. Luca Nodari (CNR-ICMATE)for performing the magnetic characterizations, Ms. Ioana Veronica Ciuchi (CNR-ISTEC), Prof. Robertas Grigalaitis (Vilnius University), Dr. Maksimas Anbinderis (Vilnius University), and Dr. Juras Banys (Vilnius University) for recording the electric impedance spectra, Ms. Andreana Piancastelli (CNR-ISTEC), Dr. Chiara Zanelli (CNR-ISTEC), and Ms. Silvia Romano (CNR-ISTEC) for recording the XRD spectra, Ms. Guia Guarini (CNR-ISTEC) for recording the sedimentation curves, Mr. Cesare Melandri (CNR-ISTEC) and Mr. Sergio Tagliaferri for the machining, Dr. Roberto Cagliero (Politecnico di Torino) for the indentation analyses, Dr. Simona Ortelli (CNR-ISTEC) for the preparation of nanopowders, Dr. Piero Torelli (CNR-IOM) for the MOKE analyses, Mr. Silviu Preda (Romanian Academy), and Mr. Vasile Adrian

Surdu (Politehnica University of Bucharest) for their experimental training on the X-ray diffraction analysis.

Financial support from RITMARE the Italian flagship project, the ANTENNA project (contract n. 1466), the “Progetto Premiale − Tecnologie e Sistemi Innovativi per la Fabbrica del Futuro e Made in Italy” project funded by MIUR (Italian Ministry of Education, University and Research), the COST action (COST reference: -STRA1226-170614-08014), and the JECS Trust are gratefully acknowledged.

Abstract

The surge of interest in multifunctional materials over the past 15 years has been driven by their fascinating physical properties and huge potential for technological applications such as sensors, microwave devices, energy harvesting, photovoltaic technologies, solid-state refrigeration, and data storage recording technologies. Among the others, magnetoelectric multiferroic composites are a special class of advanced solid-state compounds with coupled ferromagnetic and ferroelectric ferroic orders which allow to perform more than one task by combining electronic, magnetic and mechanical properties into a single device component. The production and characterization of lead zirconate titanate (PZT)-cobalt ferrite composites was the main topic of the thesis.

During the PhD activity different ceramic processing and characterization technologies were studied and involved in order to optimize the produced materials as a function of the final microstructural and functional properties.

The synthesis of cobalt ferrite (CF) and niobium-doped lead zirconate titanate (PZTN) powders by solid state reaction method and *sol-gel* technique, to control the particle size distributions and their microstructural and functional properties through calcination and milling treatments has been addressed first, followed by the mixing of the PZT and CF powders to produce particulate composites. The dispersion of PZT and CF in a liquid media, to produce layered composites by depositing the particles by electrophoretic deposition was an objective of the work as well.

Key issues such as the lead loss during the sintering of PZTN-CF composites and the reaction between CF and titania have been addressed and have resulted in improvements in the sintering and characterization techniques leading to the production of fully dense PZTN-CF *dual-particulate composites*. In particular, the optimized sintering parameters have configured a new paradigm of ceramic sintering, which has been called *quite-fast sintering*, in respect to the traditional one, and the study of the PbO loss has led to propose an equation to calculate the PbO loss through XRD analysis. Further important achieved results were: the production of nanocobalt ferrite particles by *multi-step milling*, the correlation between the spin-canting angle with the microstrain and the average crystallite

size of nanocobalt ferrite particles, the understanding of the CF growth mechanisms, the extension of the Globus model from small ferromagnetic grains “having no defect inside” to *multiparallel-twinned overgrown* ones, the understanding of heating rate effect on the interface nucleation onset of the anatase-to-rutile transformation and the anatase particle size, and the reaction products between CF and rutile at 1200 °C at the variation of CF/rutile ratio.

Contents

List of Figures

List of Tables

Chapter 1

Introduction on multifunctional materials

Nowadays humankind is proving the frustrating experience of not being able to control the infinity of possibilities offered by technology. The huge technology development rate pushes faraway the limits giving us the freedom to move in many fields of human experience without the possibility to see the edge. This creates an imagination vacuum that forces us to play it by ear. It is like our giant has not grown so much to give us the possibility of lean your head out the submarine watchtower and peer into the horizon. But, we need to scream: land ahoy! e.g. a photographer can control the huge array of photography equipment, setting parameters, and software for post processing, only if he has a clear idea to reach/highlight before to shoot. In the same way a material scientist needs to have clear the breakthrough that he wants to do. This is valid either for a technological transfer, novel device development, engineering of a new material, or deeper chemical/physical understanding of materials. In this view, multifuctional materials are one “offshore” topic because they open a large array of new avenues for tailoring the functional properties through the choice, ratio, and microstructure of the constituents, their processing, and their application in the threshold of technology. Multifunctional materials perform more than one task by combining electronic, magnetic and mechanical properties into a single device component. The main driving force for the multifuctional materials production is the demand toward device miniaturization, and this trend has led to the “renaissance of magnetoelectric multiferroics” [1,2]. Magnetoelectric multiferroics are a special class of advanced solid-state compounds with coupled ferromagnetic and ferroelectric ferroic orders. Those materials are particularly appealing because they not only show the characteristic of the single ferroic orders where the electric field E, magnetic field H, and stress σ control the electric polarization P, magnetization M, and strain ε, respectively, but also because interactions between them lead to additional functionalities. So that in a magnetoelectric multiferroic, a magnetic field may control P or an electric field may control M. For example, these additional interactions, such as the magnetoelectric memory effects and magnetic switching of ferroelectric domain, could yield entirely new device

aradigms, such as electric field-controlled magnetic data storage. The latter give the possibility of multi-state memories called multiferroic random access multi-state memories (MFRAM) that will satisfy the demand for nonvolatile memory with low energy consumption for the high-performance mobile devices and will replace the interest for the ferroelectric random access memory (FeRAM) [3,4]. Moreover, the cross coupling effects that can occur between the order states facilitates the conversion between energies stored in magnetic and electric fields and it makes magnetoelectric multiferroics scientifically and technologically fascinating in terms of multifunctionality, integration and high performance AC/DC magnetic field sensors, microwave resonators tuned electrically, microwave phase shifter, microwave signal delay line, magnetic recording read heads, photovoltaic solar cells, gyrator, solid state cooling and other possible applications [4,5]. In the next future (within ten years) magnetoelectric multiferroics could be implemented into the emerging technologies, according with Gubbi et al. [6], such as wireless power, hybrid and private cloud computing, big data, internet of things, machine-to-machine communication services, mesh network, etc., and it is very plausible that they will contribute to fundamentally transform our society. Up to now not one single-phase multiferroic compound has been discovered to display large and technologically useful magneto-electric coupling at room temperature. Nevertheless, there is a growing activity in the search of novel single-phase multiferroics that could finally provide distinctive room-temperature magnetoelectric responses, and recent novel material - chemically designed to present such multiferroic phase boundary with enhanced ferroelectricity and canted ferromagnetism - promises new developments [7]. Anyway, this issue was circumvented through the “elegant solution” [5] of multiferroic composites. The composites offer substantially advantages including greater flexibility in designing the materials for specific applications and optimization of the magneto-electric coupling. In such composites, the magnetoelectric effect arises from the stress-mediation: an electric field induces ε in the ferroelectric phase, this strain is passed on the ferromagnet, where it changes M. Thus, the magnetoelectric effect is large if the coupling at the interface and its area are large. Multiferroic composites are developed in several different combinations by combining the magnetostrictive and piezoelectric materials with different connectivity, such as particulate composites, laminated composites, nanoparticulate thin films, nano pillar film structures, ultrathin films, and other Newnham multiferroic composites [8-12]. In particular, remarkable efforts have been done to develop layered bi-layer and multilayer multiferroic composites as thick or thin films [13]. Those structures lead to remarkable

magneto-electric coupling coefficients of a few $Vcm^{-1}Oe^{-1}$ because in this configuration the ferroic layer is a “full dielectric” which can be completely poled in the conventional way [14]. Moreover in the layered configuration it is possible to design the acoustic-wave coupling between ferromagnetic and ferroelectric layers by tailoring the geometrical parameters in order to minimize the mutual clamping [15]. However, the theoretical magnetoelectric coupling (about 5 $Vcm^{-1}Oe^{-1}$ [13]) is much higher than the real one because microcracks, defects, impurity phases and insufficient interface between the piezoelectric and magnetostrictive phase prevent mechanical transfers and thus good coupling. These issues come from the high-temperature co-firing or sintering processes due to atom interdiffusion and/or chemical reactions, different shrinkage, and thermal expansion mismatch between the piezoelectric and ferromagnetic phases. In any case, compared with their corresponding particulate composites, the layered ones exhibit higher magnetoelectric coupling due to elimination of leakage problems that occur when the concentration of the ferromagnetic phase with low resistivity in the particulate composite reaches the percolation threshold [16]. For that reason the layered composites were preferred with respect to the particulate ones and thoroughly investigated [16]. Even if, in the particulate composite the low resistivity makes the electric poling difficult and reduces the magnetoelectric effect because of the leakage problem, efforts were done in order to achieve high bulk density (99%), while avoiding chemical reactions, by spark plasma sintering (SPS) instead of conventional sintering. However, SPS method has intrinsic issues of repeatability and sample homogeneity. Further improvements on the particulate composites were obtained by employing wet-chemical processing (*e.g. sol-gel* method) which allows to achieve good dispersion of high concentration ferromagnetic particles in the ferroelectric matrix [16]. In principle, the strengths of particulate ceramic composites are low cost, simple production technology, higher strain mediated magneto-electric coupling (since electric order phase/magnetic phase interface density can be higher) and easy control of electrical and magnetic properties, if the ferroelectric phase and the ferromagnetic one are mixed in a favourable proportion under the percolation threshold of the ferromagnetic phase, which results fully separated within the composite (“full dielectric” condition) [17,18]. The above reasons support the efforts on the developing of magnetoelectric multiferroic particulate composites, but nowadays a lot of process issues and material characterization features are still lacking [19] and could justify the lower magnetoelectric performances of the particulate composites with respect to their corresponding layered configuration. Lead zirconate titanate, $Pb(Zr,Ti)O_3$ (PZT) near the morphotropic phase boundary, and

cobalt ferrite, $CoFe_2O_4$ (CF) are generally chosen as constituents for multiferroic composites owing to their remarkable piezoelectric and magnetostrictive coefficients, respectively. Many papers reported the magnetoeletric properties of said composites and summarily claim that PZT and CF do not react during the sintering process, and not enough attention is given to the densification, the phase formation, and the effects of the porosity on the ME coupling [20]. Sentences like: "densely sintered" are often reported with no actual density values being mentioned. Recently, 97% relative density was achieved by microwave-sintering of 0.8PZT+0.2CF particulate composites produced by a novel sol-gel route [21]. Anyway 3% of porosity for these materials is not so low since lead volatilization occurs at temperature higher than 900 °C where the vapour-phase PbO is not kept at its equilibrium value, as in the case of pores between PZT and CF grains. In fact, PbO loss is promoted, and in turns promotes, residual porosity to be present in the material, and decreases the piezoelectric and magnetostrictive response of the composite due to the formation of baddeleyite ZrO_2 and titania TiO_2 [19] and displacement reaction between titania and CF, respectively [19,22]. In order to avoid the PbO loss and the reactions at the PZT/CF interfaces, and to achieve fully densified PZT-CF composites based on dispersed cobalt ferrite in the PZT matrix, the quite-fast sintering was developed [19]. The quite-fast sintering consists in a conventional sintering where the process parameters are taken to the extreme; e.g. in the quite-fast sintering the heating rate is higher than 300 °C/h (instead to be lower than that limit), the sintering temperature is lower than conventional one, the soaking time is less than 30 min (instead to be larger than that limit), and the cooling rate is higher than 30 °C/min. Therefore this sintering process exploits (i) the faster firing to favour the sintering, and (ii) the lower sintering temperature and soaking time, together with the higher cooling rate, to reduce the lead volatilization. The strengths of quite-fast sintering in respect to the high pressure sintering (which allows considerable reduction in sintering temperatures [23]), spark plasma sintering (which allows considerable reductions in sintering temperatures and time [24,25]), two-step sintering (which allows reduction in sintering temperatures [26,27]), and flash sintering (which allows considerable reductions in sintering temperatures and time [28-30]), are: no carbon contamination, possibility to supply lead saturated atmosphere, easy control of the process, no overheating, and final homogenous microstructures. The reliability of the quite-fast sintering passes through the production of highly reactive starting powders. In fact, the quite-high heating rate can trigger the contribution of the high energy stored in the milled particles, to promote the sintering if such energy is not released by means of other processes before the

densification. It is well known that milled powders display an enhanced sinterability [31,32]. Thus, in order to exploit the faster firing and favour the sintering process, mechanically stressed particles should be employed. The milling treatment of the powders synthesised by solid state reaction has the advantages of high reproducibility, due to the high powders homogeneity, and easy scale-up production respect to the other synthesis methods, such as *sol-gel*, which also produces powders with high specific surface area (high reactivity).

Coming back to the incipit of this paragraph, the “land ahoy” of this work is the production of magnetoelectric multiferroic composites to answer to the request of “all-in-one universal solid-state element” [5] capable of mechanical actuation, multiple memory states, logic functions, sensing and photoactive properties. This research effort mainly aimed at improving the fabrication of particulate PZT–CF composites since this configuration has shown up to now the lowest magnetoelectric effect [33] even if in principle it should display higher magnetoeletric coupling. Thus the point, or the “route” (according with figurative speaking above), is to improve the technological features in order to avoid the percolation of the dispersed ferromagnetic phase into the ferroelectric matrix, increase the percolation threshold, and preserve the physical properties of each constituent by avoiding the chemical reaction, while producing fully dense bulk ceramic composites. The focused process steps are: the cobalt ferrite synthesis, and the milling and sintering treatments. Through the optimization of these steps, the chemical reactions were strongly limited and full dense “*dual-particulate ceramic composites*” were produced. The optimized sintering parameters configured a new paradigm of ceramic sintering, which was called “quite-fast sintering”, in respect to the traditional one. This kind of sintering has the advantage to be not expensive in terms of time and energy, together with the ability to produce nanostructured architectures. In parallel, the ability to manipulate microstructural features and the easy implementation in processing advanced heterostructured nano-materials and coatings by the electrophoretic deposition (EPD) technique [34] was used, for the first time, to produce layered PZT-CF composites.

1.1 Thesis structure

This thesis is organized as follows. In the second chapter (the first is the above introduction) a list of the employed production and characterization technologies is presented. A number of features will be emphasized in order to

highlight the key points that were investigated during the PhD activity or were particularly important for the achievement of objectives. In this section, for the didactic purpose some experimental result of the investigated materials (that will be recalled in the third chapter), and sometime also other materials that are better suited (these will be not recalled), are shown. The aim is to better explain the theoretic and technological features that were studied and exploited during the PhD activity. Due to the number of involved technologies, synthesised materials, different designed architectures of the produced composites, and combination between them, only the process parameters useful to make sure the understanding and readability of the production and characterization of the magentoelectric multiferroics are reported in the experimental section: the third chapter. Further as all the experimental details, eventually not reported in this thesis, can be found in the published papers and a foot note in the paragraph titles of the third chapter sends back to them. Thus in the third chapter, for each single phase (CF and PZT) a paragraph on the synthesis and one on the sintering will be shown. These results were important to characterize the produced starting particles and their behaviour (microstructural and functional development) *vs.* specific steps of ceramics process such as mechanical and thermal treatments. A great deal of attention is paid to the CF since, as opposed to PZT, where a lot of experiences and knowledge were developed, it was a novel material that was never studied or processed before in CNR-ISTEC. The study of titania was due to study the chemical affinity with CF since in the PZT-CF composites the lead loss allows the formation of titania and, in turn, CF/titania interfaces. Moreover the study of the CF-titania system introduces the production of magneto-dielectric composites a different class of multifunctional materials, respect to the magnetoelectric multiferroic composites. Magnetodielectric composites are mainly used in the telecommunication field and a brief focus is given in the “magnetodielectric composites” paragraph. At the end the conclusions: main conclusions and “secondary” ones are reported.

The flowchart can be summarised as:

1. Introduction →
2. Methodologies →
3. Results and discussion →
4. Conclusions

Chapter 2

Ceramic processes: brief discussion about the involved technologies

The ceramic processes are very variegated and can be very complex. There is not an only one process but it should be chosen as a function of an ensemble of outputs: materials, final shape, costs, environmental impact, CO_2 foot print, water consumption, etc. In literature there are a lot of extensive books on this topic or just focused on one issue only such as sintering rather than powders shaping or suspensions preparation, or just one technology. In this chapter, the main ceramic processes and characterization techniques that were used and studied during the PhD activity are discussed in order to highlights the main features which lead to the obtained results.

2.1. Powder synthesis

2.1.1 Solid state reaction (SSR)

The production of mixed metal oxides for multifunctional applications (such as titanates and ferrites) by SSR is carried out through the carbonates decomposition and the solid state reaction between the oxides weighted in stoichiometric amount. Being based on diffusion phenomena, the reaction yield, according with the Carter equation [35], is linearly proportional with the dwell time at temperature high enough to allow the reaction, and is inversely proportional to a power, *n*, of the equivalent radius of the reagent particles ($n = 2$ if the particle are spherical). For this reason, in comparison to starting micrometer-sized powders, nanosized oxides should allow a significant reduction of soaking time for the synthesis by solid-state reaction. In Fig. 2.1 (a) it can be seen that the reaction yield for the production of $CoFe_2O_4$, at 850 °C for 4 h, is 77% and 100% starting from micrometer- and nano-sized oxides, respectively. According to the phase diagram, in ambient atmosphere pure $CoFe_2O_4$ with cubic spinel structure can be stabilized from 740.5 °C, thus the difference in the reaction yield is due to the different particle size. Since the effect of temperature follows the Arrhenius law, the temperature is the most important parameter on the kinetic constant and can

largely hide the effect of other parameters such as the different particle size (Fig. 2.1 (b)) [31,36].

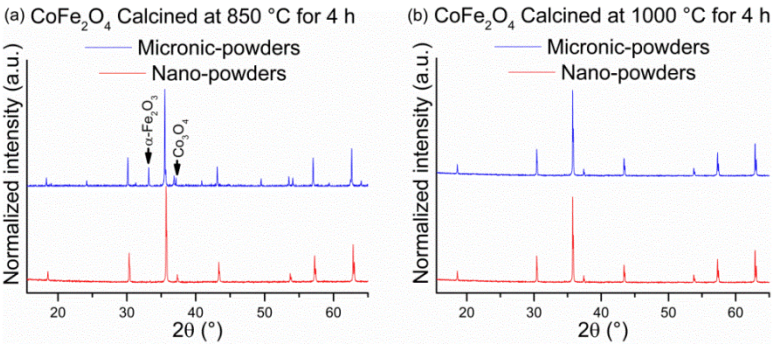

Fig. 2.1 $CoFe_2O_4$ powders synthesized starting from Co_3O_4 and Fe_2O_3 nanopowders (Aldrich 637025 and 544884, respectively) or micropowders (Alfa Aesar 45806 and Aldrich 310050, respectively) and calcined at (a) 850 °C for 4 h and (b) 1000 °C for 4 h.

Besides equilibrium and kinetic issues, the solid state reaction can result into hard agglomerates and partially sintered particles that require a properly designed milling step before cold consolidation and sintering (Fig. 2.2).

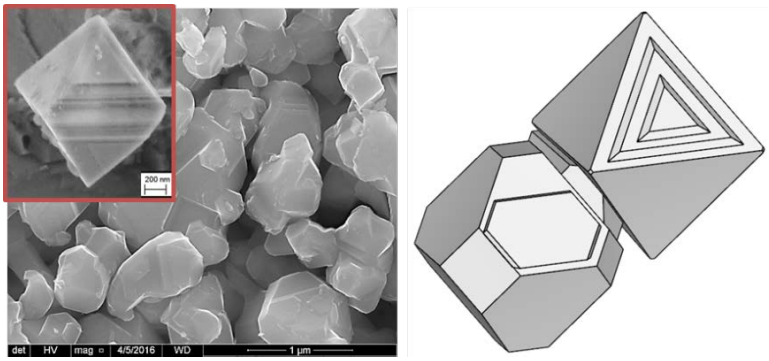

Fig. 2.2 $CoFe_2O_4$ powders calcined at 1050 °C for 4 h (left), and a graphical representation of some possible octahedron shapes build up starting from the crystal lattice refined from X-ray diffraction data (right).

2.1.2 *Sol- gel* synthesis

This technique provides a facile way for low cost and large scale production, which does not need expensive raw materials and complex equipment. Thanks to these features, the *sol-gel* technique can be addressed as “soft solution processing” [37] and is one of the synthesis methods by precipitation (*sol-gel* synthesis is often distinct from precipitation since, as it discussed in the following, gelation is

not included in precipitation. The precipitation occurs in three steps: (i) solution supersaturation, (ii) nucleation, and (iii) growth. (i) The supersaturation region can be reached by means of physical transformations, e.g. temperature or solvent evaporation, or chemical processes: addition of acids or bases. (ii) Within this region the system is unstable and precipitation occurs by segregating solute from the solution in order to minimize the Gibbs free energy. (iii) The nucleated solute clusters are dynamically stable and are driven, by the reduction of Gibbs free energy, to grow up to stable colloids (called "*sol*") and agglomerate, through short-range forces, such as Van der Waals attraction, hydrogen bond, and surface charges (see paragraph 2.1.3.), into 3D network (called "*gel*") [37,38]. Nucleation and growth, the latter related to the variation of solubility with particle radius, are inseparable processes, even though their speed can be controlled, to some extent, by modulating the critical size of nucleation, which is in turn a function of the interfacial energy, i.e. the smaller the interfacial energy, the smaller the critical size; or by controlling the concentration (*e.g.* growth of existing nuclei can occur below a critical supersaturation without formation of new nuclei) [39]. A *sol* is a colloidal suspension of solid particles so small that gravitational forces are negligible and interactions are dominated by short-range forces [40]. For the multicomponent solution the characteristic homogeneity should be kept during the separation of the solid content (*sol*) from the solution. The sediments and segregation (phase separation from the colloids) can be minimized through specific conditions, such as pH, which promotes their immobilization in a 3D network (*gel*) through the gelation of the solution. The gelation process begins with the colloidal flocculation in fractal aggregates which grow until they begin to impinge one on another in agreement with the percolation theory [40]. The final *gel* is a substance that contains a continuous solid skeleton enclosing a continuous liquid phase. Basically, all process parameters can influence the morphology the final precipitation products and also their microstructure can be affected [41]. In some cases the short-range forces induce nonuniform ordering of the particle aggregation into crystalloids with low fractal dimension instead of the flock structures characterized by high fractal dimension. Generally, flocks are produced through rapid aggregation, while if the repulsive barrier between the particles is reduced gradually, the sol may develop a "crystalline" ordered structure [40]. In order to better understand how small change of extrinsic parameters (i.e. pH, temperature, and molecular concentration) influence the particle size, morphology, defects, chemical composition, etc. during synthesis, electron micrograph of two different cobalt ferrite batches (nominally produced in the same way except for the post-firing time) are shown in Fig. 2.3 and Fig. 2.4. For

these samples, the *sol* precursor was prepared starting from iron nitrate, cobalt acetate and citric acid monohydrate as chelating agent. Ethanol, acetic acid and water were used as solvents. The iron nitrate and citric acid were dissolved in ethanol separately, at room temperature. The cobalt acetate was dissolved in ethanol, acetic acid and water. The solution of iron nitrate was added to the cobalt acetate solution and then, the citric acid solution was added to the mixture solutions of Fe and Co, to form a cobalt ferrite precursor *sol*. The as obtained sol was maintained under continuous stirring at 80 °C, for 4 h, to obtain the *gel*. After drying the gel at 120 °C, the resultant powder was treated at 700 °C, 1 h (Fig. 2.3) or 3 h (Fig. 2.4) in air, in order to synthesize $CoFe_2O_4$. From Fig. 2.3 and Fig. 2.4 it can be seen that not only the two batches are markedly different between them, but the same batch displays a different kinds of particles: nanometric or micronic single particles more or less elongated, agglomerates, aggregates, sintered aggregates with smoothed or facetted grains. This confirms that locally the process parameters cannot be easily controlled and can lead to an inhomogeneous product.

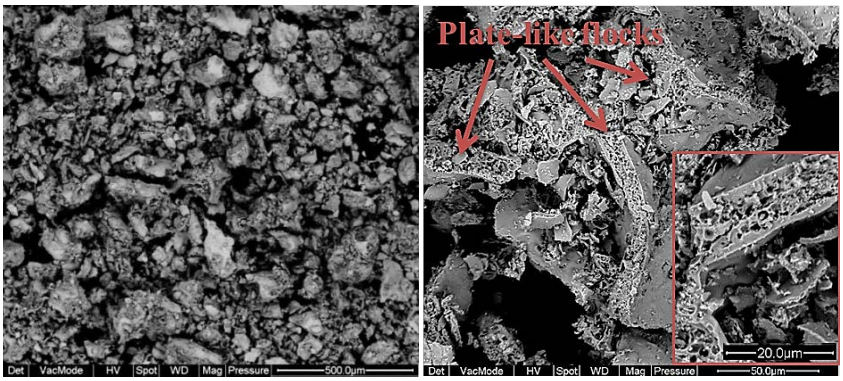

Fig. 2.3 Cobalt ferrite powders with high fractal dimension and high specific surface area synthesized by sol-gel method and post-fired at 700 °C for 1 h.

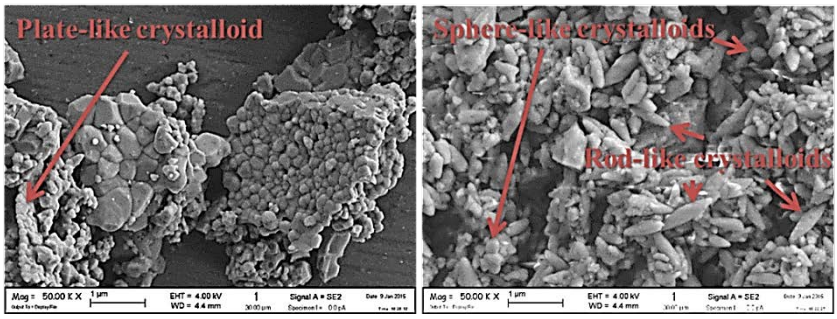

Fig. 2.4 Cobalt ferrite powders with low fractal dimension and low specific surface area synthesized by sol-gel method and post-fired at 700 °C for 3 h.

Generally, when the gelation process is not well controlled, the as synthesized powders cannot be employed in the ceramic processes since such inhomogeneity affects the microstructure of the final dense ceramic material. Moreover, if the kinetics of the *sol* formation are not well controlled, the formation of intermediate phases will require high calcination temperature to assist the long-range diffusion in the material and obtain a pure phase, which in turn leads to an incomplete densification due to the formation of strong aggregates that preserve the structure of the original polymeric *gel* network [42]. However, even if, after the post-firing process the desired phase was obtained with the right stoichiometry, a further milling step can remarkably improve the homogeneity in terms of particle size distribution and shape (Fig. 2.5). It must be taken into account that the milling treatment introduces a series of microstructural and morphological changes (discussed in the 2.2.1. paragraph) that should be considered in order to exploit the milled powders in the following steps of the ceramic process, e.g. slurry preparation, suspension stabilization, etero-coagulation, green consolidation, sintering, etc.

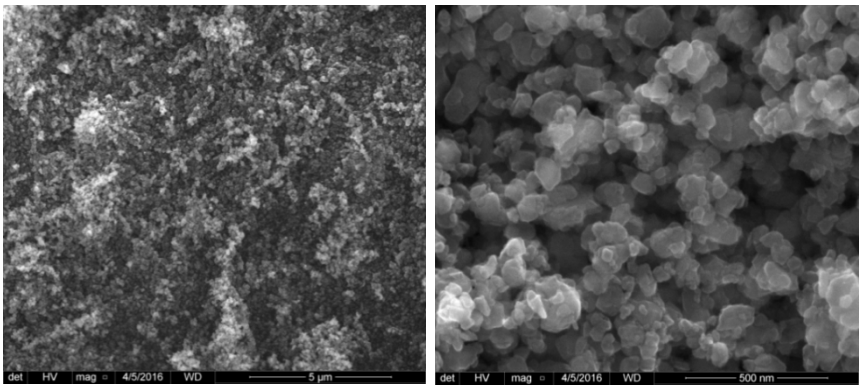

Fig. 2.5 Energetically milled cobalt ferrite powders synthesized by sol-gel method and post-fired at 700 °C for 1 h.

2.1.3 Suspensions

When a ceramic particle is immersed in a polar liquid medium there is a build-up of charge at the solid surface, due to different charging mechanisms such as: dissociation of surface functional groups, superficial dissolution of ions (e.g. sparingly soluble), adsorption of ions or polyelectrolytes, charges inclusion (e.g. clay). This surface charge influences the distribution of nearby ions in the polar medium, which rearrange in a double layer in order to neutralize it. The double layer is formed by an inner monolayer of counter-ions attached to the ceramic surface (the Stern layer), and a diffuse layer of ions and counter ions which form

an “ionic atmosphere” around the solid phase. These heterogeneous systems are affected by the pH value (and vice versa) and the surface charge density of the particles is characteristic of every particle-solvent system. In particular, the zeta potential (ζ) – the potential at the slip plane that separates the region of fluid (cloud of counterions) that moves with the particle from the rest of the fluid – can move from positive values to negative ones passing through the isolelectric point (ζ = 0) with the changing of pH. Thus, by measuring ζ vs. pH of a suspension it is possible to plot a representation of the surface charge behaviour and tailor its electrostatic stabilization (locating the suspension at a pH far from its isoelectric point). The selection of pH should be done keeping in mind that particles dissolution can occur at pH values too acid or basic. According with the Gouy Chapman model, ζ increases by decreasing the counterions valence and their concentration in the solution. Monovalent ions, with a large radius and possibly hydrated, produce a large diffusive layer and thus increase the repulsive forces since ζ value increases according to the following equation:

$$\zeta = \frac{4\,\pi\,e\,d}{\varepsilon} \qquad \text{Eq. 1}$$

where d is the thickness of the diffuse layer, e is the surface charge density, and ε is the dielectric constant of the liquid media. The suspended particles in a liquid media tend to agglomerate when the zeta potential is close to zero if some deflocculant is not added (DLVO theory). Stable suspensions can be produced by adding electrolyte polymers in order to increase the net charge and, above all, offer a steric hindrance. Anyway, some processes such as the electrophoretic deposition require a controlled destabilization of the suspension in order to allow the coagulation (deposition) of the particle at the working electrode (the electrode characterized by opposite charge of the particle) despite the high stability and high ζ value allow the mass transport (electrophoresis) [43].

2.1.4 Core@shell particles

Core-shell structures with a large well defined interface area are particularly interesting for the production of multifunctional ceramics [44]. Through those structures it is possible to tailor the magnetodielectric properties as well as the magnetoelectric ones. In particular, exploiting the core-shell structures, where the magnetostrictive phase is the core and the piezoelectric phase is the shell, an enhanced magnetoelectric effect is expected due to the possibility of increase the

magnetostrictive an enhanced magnetoelectric effect is expected due to the possibility to increase the magnetostrictive phase volume fraction up to the optimum value (about 0.5 [17]) avoiding its percolation into the bulk magnetoelectric composite. In Fig. 2.6 and Fig. 2.7 a model of the desired magnetoelectric structure and an experimental example are shown, respectively. In order to achieve this goal the milling step after the core-shell particle production cannot be performed, thus the synthesis process must be properly controlled and optimized. This is not an easy goal to achieve since the process needed further steps after the synthesis of particles with narrow size distribution. In fact, the synthesized particles, which will be the core, after washing, are coated with a shell of amorphous hydrous ceramic oxide obtained by hydrolysis of a solution of its peroxide complex and slow heating a low temperature (less than 100 °C). To obtain a shell of a perovskitic phase (owing to the remarkable piezoelectric properties) a suspension of carbonate/oxide nanoparticles with a proper pH – that should promote the etero-coagulation – is slowly added to the suspension of the core-shell particles that must have an opposite surface charge in order to allow the etero-coagulation. If the carbonate oxide nanoparticles preferentially adhere on the shell surface, and the shell was not dissolved, the solid phase is finally separated, washed, and freeze-dried. At this point a thermal treatment is performed in order to promote the reaction between the shell and the etero-coagulated nanoparticles, thus the formation of the perovskite phase, and avoid the reaction between the core and the formed perovskitic shell.

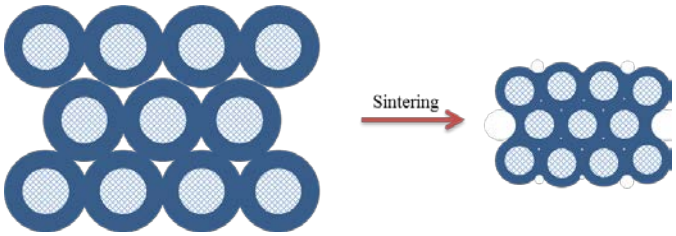

Fig. 2.6 Schematic drawn of compacted core-shell particles (left) and the dense microstructure obtained after sintering.

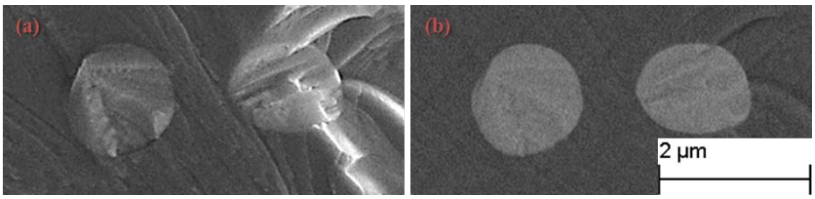

Fig. 2.7 (a) Secondary electron image and (b) back-scattered electron image of fracture surface of sintered $0.89(Na_{1/2}Bi_{1/2})TiO_3+0.11BaTiO_3@CoFe_2O_4$.

2.2 Powder treatments

2.2.1 Milling

A key step in the ceramic technology is the milling treatment. Through comminution (crushing and grinding) it is mainly possible to (i) decrease the mean particle size, (ii) change the particle size distribution, (iii) change the particle morphology, and (iv) disperse the aggregates. All these powder characteristics influence the powder morphological, microstructural and functional properties (Fig. 2.8), thus their applications (e.g. catalysis, and "greentech" [45-50]), and the next steps of ceramic processing (e.g. shaping [51-54] and sintering [31,55]). Particle size distribution strongly affects, first of all, the powder jamming and cold compaction, and then the microstructural and sintering behaviour [55]. In the first panel of Fig. 2.9, it can be seen that the milling effects are different depending on the different synthesis conditions of $CoFe_2O_4$. Then, the different effects caused by the milling treatment on crystal microstructure, such as the crystallite size, affect the microstructure evolution during the sintering (in the second panel of Fig. 2.9 it is shown the multi parallel twinning overgrowth is enhanced by the power of milling treatment [31]). Finally, in the last panel of Fig. 2.9, it can be seen how the magnetic properties of the bulk $CoFe_2O_4$ keep memory of the milling treatment.

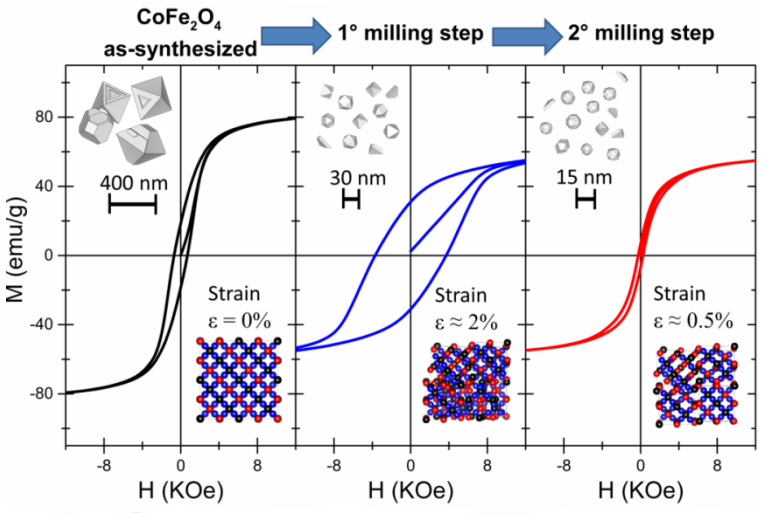

Fig. 2.8 Magnetization vs. magnetic field strength plots of as-calcined $CoFe_2O_4$ and the milled one and two times. The particle size and the microstrain of each step (calculated through Rietveld analysis) is shown, since these two parameters have a considerable weight on the magnetic hysteresis shape.

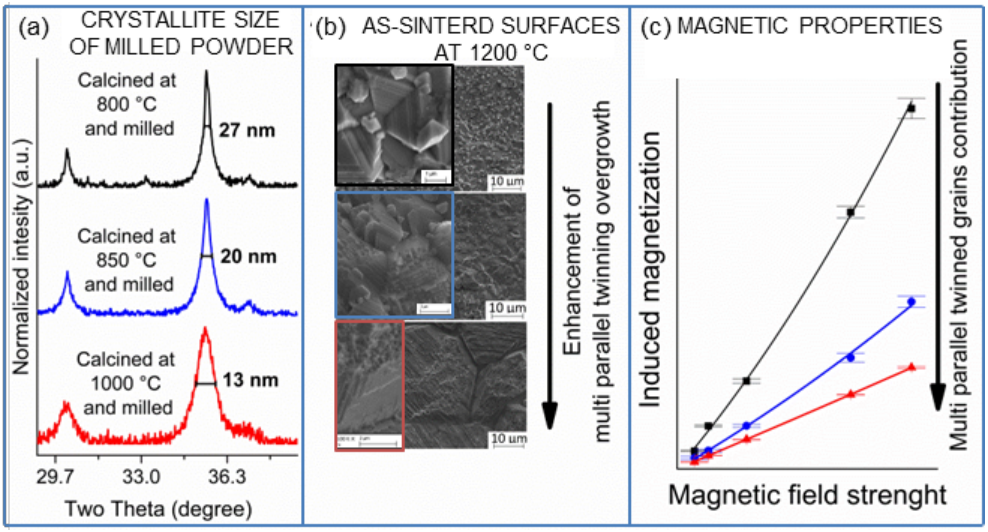

Fig. 2.9 Milling treatment effect on the crystal structure of $CoFe_2O_4$ powders (a) and its knock-on effect of the microstructure evolution during the sintering process (b) and the correlation with the final magnetic properties (c).

In order to optimize the milling process the following features have to be treated: (i) description of the milling media kinetics; (ii) nature and quantification of the interactions between the milling media and the powder; (iii) deformation phenomena occurring in one powder particle interacting with a milling media (fracture, welding, oxidation, mechanical induced phase transformation, etc.); (iv) physical phenomena occurring inside the powders (diffusion, heating, work hardening (Fig. 2.8), lattice defects nucleation (Fig. 2.8), oxidation, recovery, etc.). In the following the planetary ball mill is taken as example since it is often used in ceramic process, mechanical alloying, oxide-dispersion-strengthening, etc. The planetary milling (Fig. 2.10) consists of a sun disc rotating at angular speed Ω on which the jar, of radii r, is rotating in the opposite direction towards the sun disc (at angular speed ω). (i) Once the angular speeds are set the trajectories of milling media in the mill are determined. In particular the arc length of the jar, L, where the milling media are oriented towards the exterior of the mill, is given by:

$$L = r \cdot arccos\left(-\frac{r}{a}\left(1-\frac{\omega}{\Omega}\right)\right) \qquad \text{Eq. 2}$$

where a is the distance between the centre of the sun disc and jar. In the complementary arc length the resultant of the forces on milling media is oriented

towards the centre of the mill. (ii) Once a milling media has left the *L* arc of jar it can follow three types of trajectory: “chaotic” (low ω/Ω ratio); “impact + friction” (higher ω/Ω ratio); “friction” (very large ω/Ω ratio) [56]. The terms “impact” and “friction” refer to the two force components normal and tangential to the mill surface, respectively. Thus the mill can be designed for specific purpose depending upon the value of ω/Ω ratio. These trajectories are defined within the milling media do not come into contact with each other. In this scenario (high amount of milling media) several layers of milling media are subject at different effective *r* values and the two force components change layer by layer. Moreover in this scenario the milling media-powder interactions do not involve in impact but occur during sliding or rolling of the milling media. However, the theoretical power transferred to the powders is always proportional to the intensity of the single milling media-particle interaction Ω^2 and to the frequency ω of such event, but there is also a critical ω/Ω ratio above which a reduced grinding action is expected [56].

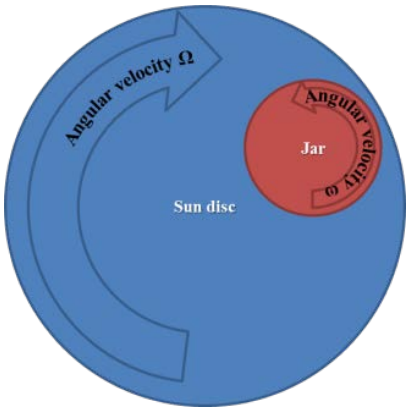

Fig. 2.10 Schematic draw of a planetary milling. For the Fritsch Pulverisette 6 (available at CNR-ISTEC), the effective diameter of main disk is 121.6 mm and transmission ratio planetary disk / grinding bowl is 1 : -1.82.

The (iii) and (iv) points together with the previous ones determine the milling efficiency. In fact, not only the frequency and the energy of the interactions influence the milling efficiency but also the mechanical behaviour and the microstructural characteristic of the powder play an important role [57]. An ensemble of microstructural defects can reduce the particle strength (Fig. 2.11). The milling efficiency can be studied through the particle size density distributions obtained before and after a milling treatment (Fig. 2.12). The particle

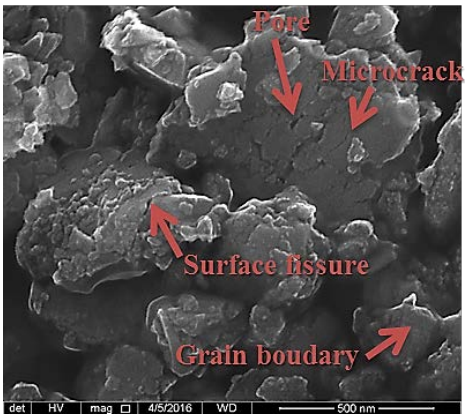

Fig. 2.11 Defects can reduce the resistance of the particles.

size, weighted on the equivalent spherical diameter (d_{nl}) and on the volume (d_{nV}), can be calculated as follow [58]:

$$d_{nl} = \frac{\sum_{i=1}^{n} d_i N_i}{\sum_{i=1}^{n} N_i} \qquad \text{Eq. 3}$$

$$d_{nV} = \sqrt[3]{\frac{\sum_{i=1}^{n} d_i^3 N_i}{\sum_{i=1}^{n} N_i}} \qquad \text{Eq. 4}$$

where q is the density distribution value of the particles having diameter d. Generally, like in a non-normal distribution, the d_{nl} value is smaller than the d_{nV}, which attributes greater weight to bigger particles (volume is proportional to the cube of the diameter). Thus, these two statistical parameters refer to "two" population of the particle distribution: the smaller particle (d_{nl}), and the larger ones (d_{nV}). By checking their values it is possible to make some qualitative and quantitative consideration about the milling efficiency. Thus, in the inset of Fig. 2.12 the slope of the d_{nl} (solid lines) and d_{nV} (dashed lines) values with respect to the milling time (t) allows the separation of the effect of milling on the finer and coarser particles. In fact, from the ratio between the milling efficiency on the finer particles ($\Delta d_{nl}/\Delta t$), and coarser ones ($\Delta d_{nV}/\Delta t$) [31]:

$$R = \frac{\Delta d_{nV}/\Delta t}{\Delta d_{nl}/\Delta t} \qquad \text{Eq. 5}$$

it is possible to determine whether the particle size distribution becomes narrower or wider with the milling time (t). If the value of *R* is higher than 1, then the distribution is narrower, the opposite if *R* is lower than 1. In this way it is possible to assess each milling step in terms of its efficiency with respect to the "two" particle populations and tailor the milling treatment towards decreasing the mean values rather than particle size distribution broadening by changing milling parameters such as the milling media size or mass, ω/Ω ratio, etc.

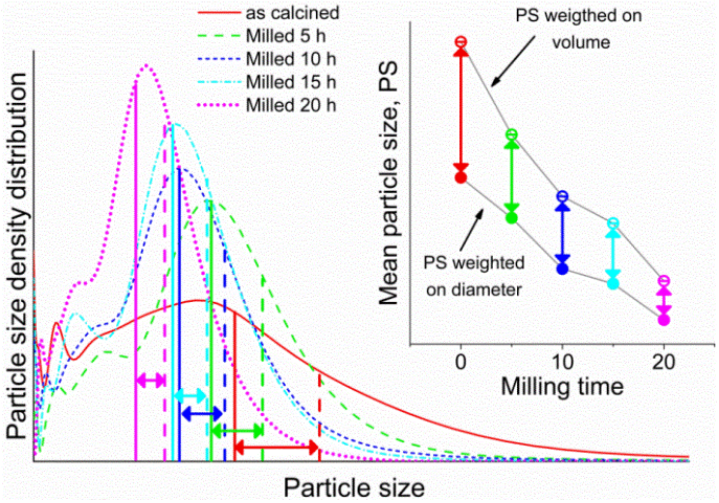

Fig. 2.12 Particle size density distribution of as calcined $CoFe_2O_4$ powders (solid red line), after milling time of 5 h (dash green line), 10 h (short dash blue line), 15 h (short dash dot cyan line), and 20 h (short dot magenta line). The solid line and the dashed one under the particle size density distribution curves indicate the mean particle size weighted on equivalent spherical diameter (d_{nl}), and on volume (d_{nV}), respectively. In the inset the corresponding d_{nl} (solid symbols) and d_{nV} (open symbols) values vs. milling time are shown.

2.2.2 Mixing

Inhomogeneous mixing between different powders (i.e. reactant particles for solid state synthesis, different phases for the production of composites, or different granulometric powder fractions of the same batch), can lead to a failure, for example, of reaction yield of the synthesis, a change of the products (locally the different stoichiometry can stabilize another phase), a bad dispersion and/or distribution of the different constituents of a bulk composite, a differential shrinkage during densification, etc. These issues are more frequent when a mechanical mixing is performed in dry conditions. In Fig. 2.13 an example of

multicomponent particle mixed by 3D turbula machine is shown. After mixing the different particles are separately agglomerated: cobalt ferrite forms spherical agglomerates completely separated from the facetted particles of silica. This degree of mixing influences the phase dispersion in the green sample where the agglomerate of cobalt ferrite and silica is in the order of 10^2 μm, even if the primary particles are submicrometric. In order to improve the dispersion of the phase, or, more in general, the homogeneity, wet mixing followed by an oppropriate drying method such as rota vapor, spray drying, and freeze drying, can be performed (Fig. 2.14).

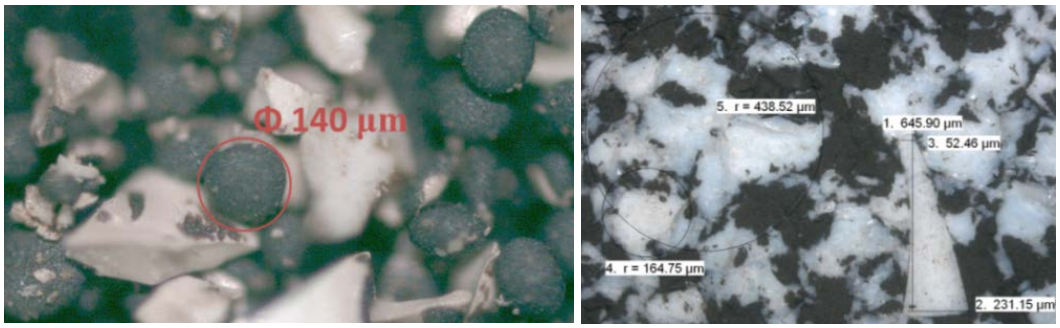

Fig. 2.13 Optical micrographs of (left) $CoFe_2O_4$ (black) and amorphous SiO_2 (white) powders mixed in a weight ratio of 80:20, respectively, by 3D turbula mixing, and (right) surface of the green sample.

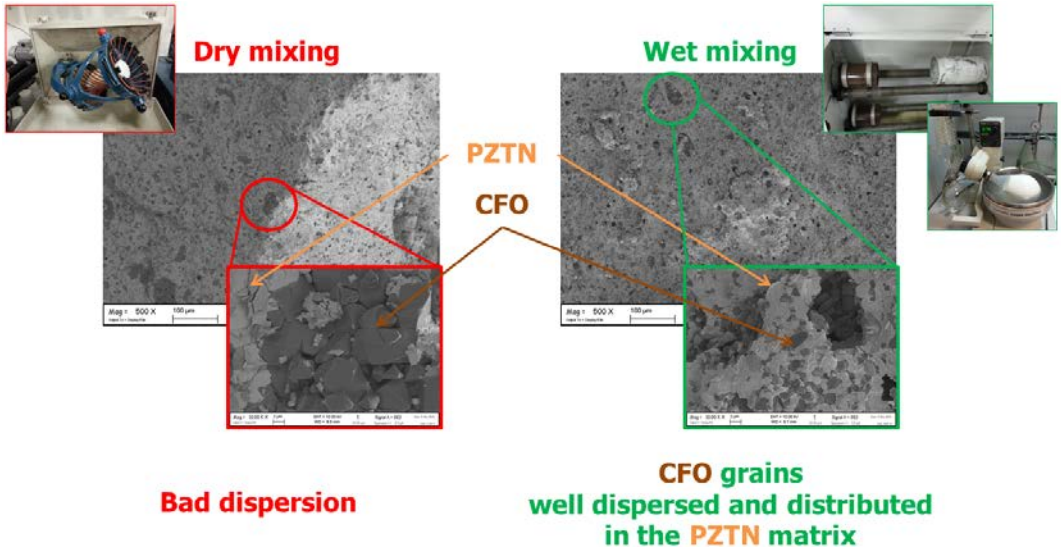

Fig. 2.14 Comparison of dry/wet mixing influence on the sintered microstructure of (1-x)Nb-doped lead zirconate titanate (PZTN) – (x)cobalt ferrite (CFO) composite, with x = 26 mol%.

2.2.3 Cold consolidation

The cold compaction of powders allows for the optimization of the production of both traditional and advanced ceramics, since the sentence: “the green body with higher green relative density results in higher final relative density” is generally true [55]. In this process, the geometrical and mechanical characteristics of the ceramic powders affect the transition between a loose ceramic powder and a dense green body, which is based in two phases: (i) granule sliding and rearrangement, and (ii) granule deformation [53]. The cold consolidation is typically performed by linear press, which can be single or double action. Both kind of linear pressure forming techniques produce a density distribution inside the green body (the density distribution obtained with double pressure forming technique is more uniform than that obtained with the single action device [54]). In order to reduce the density gradients, after the liner pressing an isostatic pressing can be performed. The isostatic pressing can close the cracks formed due to the “slip and stick” or “end-capping” during the extraction from the die. Some powders are difficult to compact. This can happen especially with the nano- and/or work-hardened powders, since their poor ability to arrange plastic deformation during compaction remarkably increases the elastic response of the spring back. In fact, it is well known that the cold compaction of ceramic powders is driven by plastic volumetric strain, e_V^p, through the following equation [51]:

$$\rho = \frac{\rho_0}{1 + e_V^p} \qquad \text{Eq. 6}$$

where ρ_0 is the initial density, and the plastic strain values are between $-1 < e_V^p \leq 0$. This equation means that if the powders are not able to activate plastic deformation after the break-point pressure, $e_V^p = 0$, the final density will be equal to the initial one, since a strong elastic release of deformation occurs at unloading [52]. In order to increase the compression characteristics and the cohesion between the particles, *i.e.* improve the flowability of the powders, they can be granulated with solvent/water solution containing a binder (e.g. PEG, PVP, etc.). Although the granules of the same powders are often more easily compacted, the binder burnout could introduce defects that are not eliminated during the sintering process. Other key characteristics of the powder - which can influence the microstructure of the green pellet - are their shape and size distribution. These parameters influence the packing density and the size and shape of the pores in the green body and thus the microstructure development during sintering. These parameters are more difficult to control and optimize

according with the Furnas model, but in practice a standard deviation of about 1.4-2.4 should lead to a packing density of 65-69% [57].

2.2.4 Sintering

Sintering is a fundamental technological step to manufacture almost all ceramics (e.g. except geopolymers [59-61]) and many metals) from compacted powder particles [62-65]. During the sintering process the powder compacts densify with accompanying dimensional changes resulting in mechanical strengthening, possible gastight microstructures and improved thermal conductivity. Several sintering techniques today are available and they allow the control of many microstructural and macroscopic features of different material classes. To satisfy the technological demands of specific final microstructures (for example, very tight tolerances of grain and pore size, compositional architecture, etc.), it is important to choose the right sintering process and then optimize the processing condition and powder characteristics, such as sintering temperature, time, atmosphere, application of load, powder purity, additives, pore formers, particle size distribution and others. Each parameter can be varied to meet the tolerance requirements. For example, it well known that ceramic barium titanate can have wide differences in grain size, depending on exact composition and processing conditions [66]. In Fig. 2.15 (a) a typical strontium barium titanate microstructure is shown. It consists in bimodal grain population peaked at 2 μm and 20 μm (occasional giant grains, some of them visible to the naked eye, are present) with pores at the grain intersection and inside the large grains. By changing the sintering atmosphere, from air (Fig. 2.15 (a)) to argon (Fig. 2.15 (b)), a remarkable decrease of grain size (< 500 nm), and an entirely homogeneous microstructure without coarse grains was obtained.

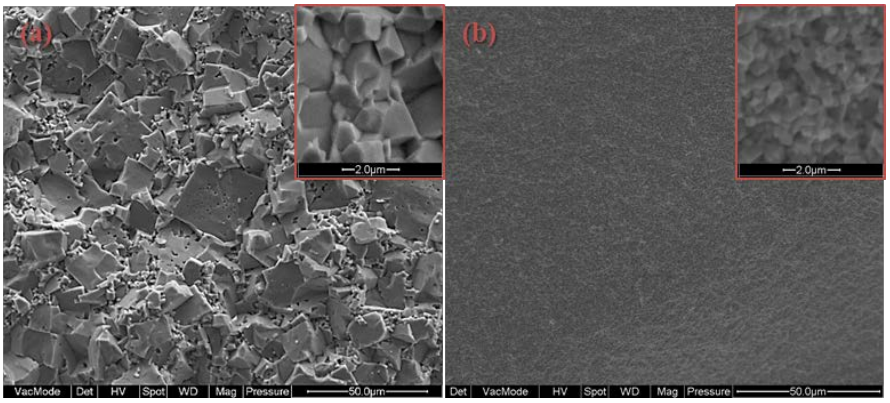

Fig. 2.15 Fracture surface of $Ba_{0.6}Sr_{0.4}TiO_3$ densified at 1250 °C for 2 h (a) in air, and (b) in argon atmosphere.

Another way to produce nanostructured microstructures is the quite-fast sintering [19]. This sintering technique consists in a conventional sintering where the process parameters are taken to the extreme; *e.g.* in the quite-fast sintering the heating rate is higher than 300 °C/h (instead to be lower than that limit), the sintering temperature is lower than the conventional one, the soaking time is less than 30 min (instead to be larger than that limit), and the cooling rate is higher than 30 °C/min. In Fig. 2.16, a comparison of the different heating profiles between the conventional sintering and the quite-fast sintering is shown. This sintering process exploits (i) the faster firing to favour the sintering (especially for the nanopowder and/or energetically milled powders, since the high heating rate can trigger the contribution of the energy stored in particles in enhancing the sintering, thus reducing the energy released by means of other processes before the densification) and (ii) the lower sintering temperature and soaking time, together with the higher cooling rate, to reduce the grain growth and other parasitic phenomena such as solid or gas phase decomposition, recrystallization, displacement reactions in multiphasic system, etc. The strengths of quite-fast sintering respect to the high pressure sintering (which allows considerable reduction in sintering temperatures [23]), spark plasma sintering (which allows considerable reductions in sintering temperatures and time [24,25]), two-step sintering (which allows reduction in sintering temperatures [26,27]), and flash sintering (which allows considerable reductions in sintering temperatures and time [28,29,30]) are: no carbon contamination, possibility to supply a controlled atmosphere through pack source (Fig. 2.17), easy control of the process, no overheating, and final homogenous microstructures.

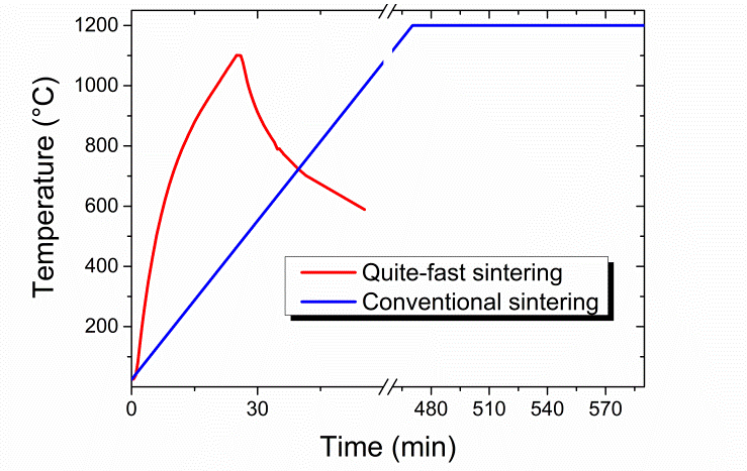

Fig. 2.16 Heating profile of quite-fast sintering (red curve, T_{max} = 1100 °C) and conventional sintering (blue curve, T_{max} = 1200 °C).

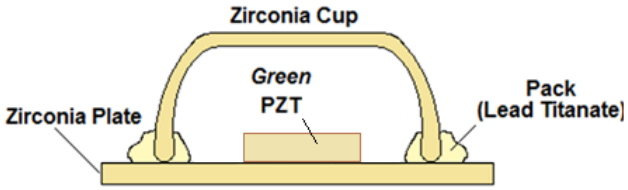

Fig. 2.17 Scheme of a green sample of lead zirconate titanate (PZT) surrounded by lead-based powders, called pack (a mixture of PbO and ZrO_2 or $PbTiO_3$ powders), in order to provide a positive vapor pressure in a closed zirconia cup and contain the lead loss. Similar scheme, but with different composition pack, can be used to prevent the loss of other volatile elements such as Na, Bi, etc.

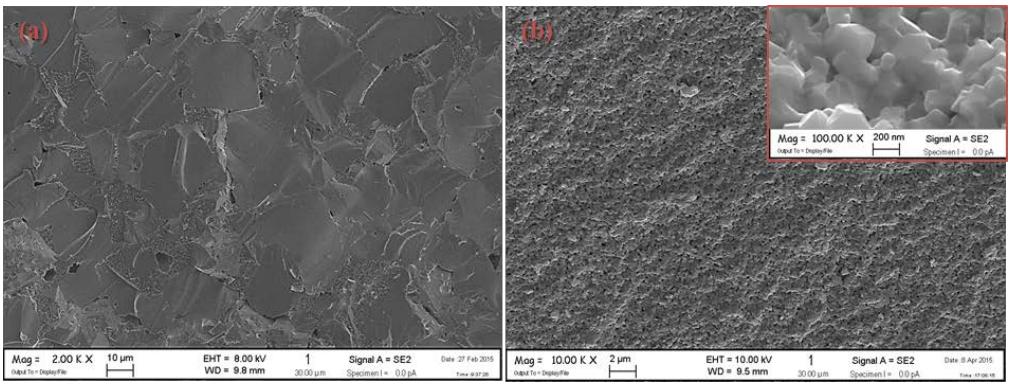

Fig. 2.18 Fracture surface of $CoFe_2O_4$ sintered by (a) conventional sintering, and (b) quite-fast sintering. Their heating profile is that shown in Fig. 2.16.

The quite-fast sintering results particularly convenient for the sintering of multifunctional ceramic composites where avoiding the reactions that can have a detrimental effect on the functional properties of the final component is fundamental [19]. The benefits of the quite-fast sintering are especially important when particles are nanosized. It is well known by the Herring's scaling law,

$$\left(\frac{r_1}{r_2}\right)^m = \frac{t_1}{t_2} \qquad \text{Eq. 7}$$

that nanoparticles (i.e. r_1 = 100 nm) achieve the same densification state of micronsize particles (i.e. r_2 = 10 μm) in a time, t_1, 10^6 or 10^8 times smaller than t_2 (the time spent by microparticles), if the integer m corresponds to a volume diffusion (m = 3) or surface/grain boundary diffusion (m = 4) transport mechanism, respectively [67]. The driving force is the gradient pressure between

the inner and the outside of the particle (Kelvin-Laplace law) and mass flow follows the Fick's first law, which diffusion coefficient depends on the transport mechanism and follows the Arrhenius law. Thus the rates (v) of the different transport mechanisms depend on both particle size and temperature as is shown in Fig. 2.19

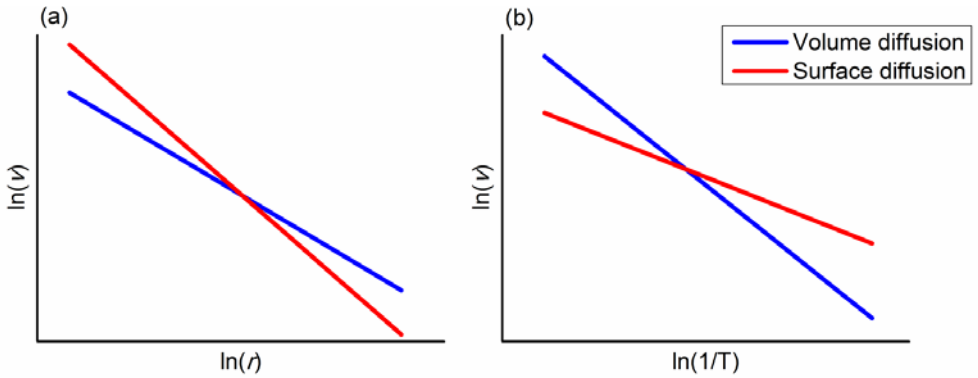

Fig. 2.19 Natural logarithmic plots of transport mechanisms velocity, v, *vs.* (a) particle radius, r, and (b) inverse of temperature, T^{-1}.

High temperature ramp (such as in the quite-fast sintering, Fig. 2.16) may reduce the time the system stays in the T region where surface diffusion prevails over grain boundary diffusion. This latter transport mechanism contributes to both sintering and densification. While the small starting particle size exploits superficial diffusion mechanism at low temperature which drives matter from the particle surface to the neck region, but not to densification. This combination enhances the densification and avoids the particles coarsening (Fig. 2.20). For this reason quite-fast sintering could give better results in terms of final densification and control of grain size, although a lower sintering temperature is set.

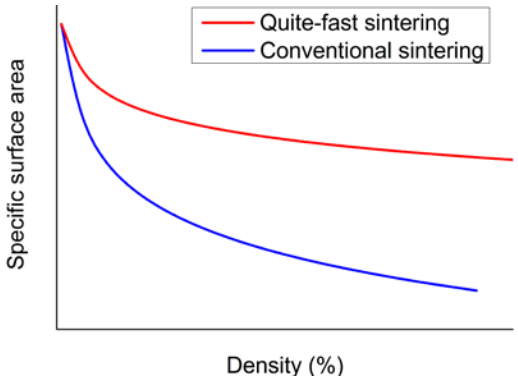

Fig. 2.20 Reduction of specific surface area vs. densification.

2.2.5 Electrophoretic deposition (EPD)

Amongst the great variety of methods for the film preparation, electrophoretic deposition (EPD) is gaining increasing interest due to its versatility and high potential for scaling up to large volumes. Actually, it might even become an alternative to the evaporative coating processes to tailor nano- or microstructures of ceramic and composite coatings [68]. Moreover, this technique is widely used in the industry to obtain coatings of practically any dimensions and complex shapes (from fasteners to car bodyworks), microelectronic substrates, piezoelectric devices and sensors, among others [69]. Indeed, the EPD is an attractive processing technique for ceramics, including novel additive manufacturing approaches [70], both the kinetics of film growth and the adhesion/robustness of the deposit are influenced by several processing parameters. Different dispersing liquids and stabilizers can be used for the preparation of stable and standardized ceramic suspensions suitable for EPD, which is performed by applying an electric field between two electrodes immersed into the suspension (Fig. 2.21). When an electric field is established between the two electrodes, the electrically charged colloidal particles travel to and accumulate on the electrode with opposite polarity (called working electrode) to that of the surface charge they carry (proportional to ζ, Eq. 1). According with the Hamaker equation [71]:

$$m = C_s \mu S E t \qquad \text{Eq. 8}$$

the deposited mass per unit area (m) depends linearly with the suspension concentration (C_s), electrophoretic mobility (μ), imposed electric field (E), deposition area (S), and deposition time (t). Thus concentrated suspensions are needed to improve density and speed up the coagulation of the particles on the working electrode. This requirement is in conflict with the required stable suspension and force to increase the complexity of the suspension formulation which contains not only particles and ions, but also deflocculants, surfactants, binders, gelling agents, etc. chosen also in order to allow the particle coagulation at the working electrode (which occurs via double-layer distortion and thinning) and better control the following processing steps such as the drying (in particular the Marangoni effect). This large number of parameters makes a rich set of deposition conditions available and justifies the trial-and-error approach which dominates the experimental work in this area.

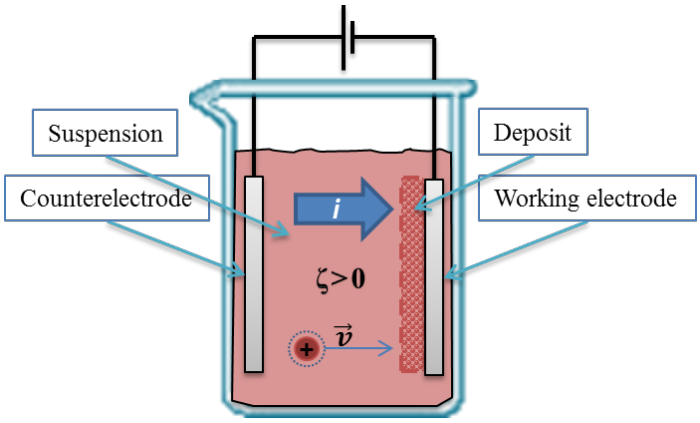

Fig. 2.21 Basic draft of a cathodic deposition using a plane-parallel geometry EPD cell.

2.2.6 Electroding and Poling

These processes are necessary, first of all, to induce piezoelectric characteristics to the ferroelectric ceramic and then to collect/send the electrical signal. The electroding can be done by metal sputtering (e.g. gold or Pt/Pd-alloy) or by screen printing a metal paste (e.g. silver or platinum). Both techniques display side effects, in fact, owing to the semiconductor nature of the ceramics (also the ferroelectric one, of course they are characterized by a wide bandgap), any metal contact injects a certain number of charges into the Schottky barrier affecting the thermodynamics of ferroelectrics and generating a modified ferroelectric layer at the interface [72]. The thickness of that layer is proportional to the defect state density e.g. oxygen vacancies or Schottky defects, and can reache a sizable screening depth. Sputtered electrodes are mechanically fragile, since the metallic clusters are physically laid. For this reason silver pastes are preferred. The latter consist in a mixture of silver particles bumpy dispersed in a glass frit that causes a drop of the applied voltage. The above side effects are enhanced when a magnetic phase, which is often slightly conducting, is present. Another collateral effect of the conductive paste is the clamping that constrains the lateral expansion of the piezoelectric layer under the electrode. This effect increases at the increasing of the paste thickness to piezoelectric thickness ratio [73,74]. Once the electrodes are deposited on the sample has its it is possible to proceed with the poling in order to align the electric dipoles along the applied electric field and retain a net permanent macroscopic electric dipole (the remanent polarization); the applied electric field is then removed and the ions distribution of the sample riches its metastable equilibrium. In order to avoid the dielectric breakdown and stimulate, under a lower electric field, the ferroelectric domain

walls rearrangement up to the saturation polarization, the sintered and electroded sample is placed in a holder immersed in a bath of silicone oil about 120 °C for ceramics based on lead titanate zirconate solid solution. The applied electric field to pole a ferroelectric ceramic is in the order of 2-4 kV/mm and is removed after a dwell time at temperature plus the time spent to cool down the system (sample immersed in the oil bath) at a temperature far from the above temperature (typically 50 °C is enough for ferroelectric ceramics). In Fig. 2.22 (c) one of the worst scenarios (where all the side effects are boosted) is shown. In case of particulate ceramic composites with a dispersed magnetic phase the requirement for “full dielectric” can be no longer applicable if the ferromagnetic phase is not fully separated within the composite. This means that the percolation of magnetic phase does not make it possible to pole the sample due to leakage current of ferromagnetic phase [17,18].

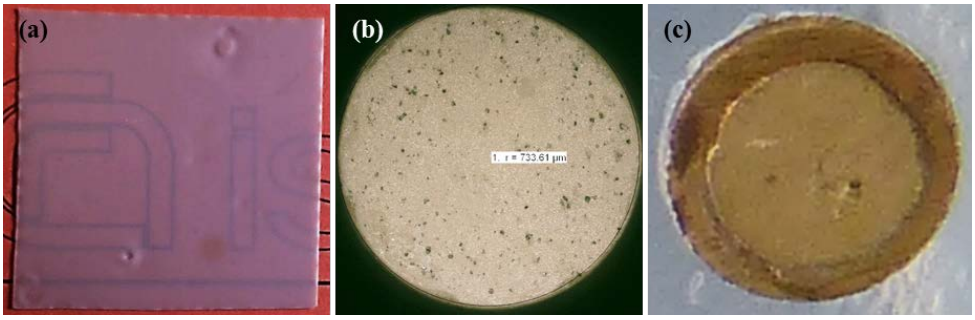

Fig. 2.22 (a) Sintered tape of Nb-doped lead zirconate titanate (PZTN) characterized by a thickness of t = 70 μm; (b) PZTN disk (ϕ 1.5 mm) obtained from the tape; (c) PZTN disk sputtered with gold, poled, and glue on a brass disk (ϕ 2 mm, t = 0.3 mm).

2.3 Morphologic-microstructural characterization

The compositional and microstructural analyses is covered by several techniques. The Scanning Electron Microscopy (SEM) coupled with the Energy Dispersive X-ray Analysis (EDXA) and the X-ray diffraction analyses (XRD) were the main involved techniques. The former allows the morphological and compositional characterization of fracture surfaces (Fig. 2.7), as-sintered surfaces (Fig. 2.9 (b)), and powders (Fig. 2.11); the XRD analysis permits a deep understanding of the microstructural properties (Fig. 2.1 and Fig. 2.9 (a)). Through these two techniques it is possible to determine - within their resolution limit and chemical-physical constraints - the phases, the microstructure, the crystal structure and grain size and phases distribution, in order to investigate the influence of the technological processes on the products, or to characterize the

morphology and microstructure of the material (in Fig. 2.23 an example of image analysis is shown).

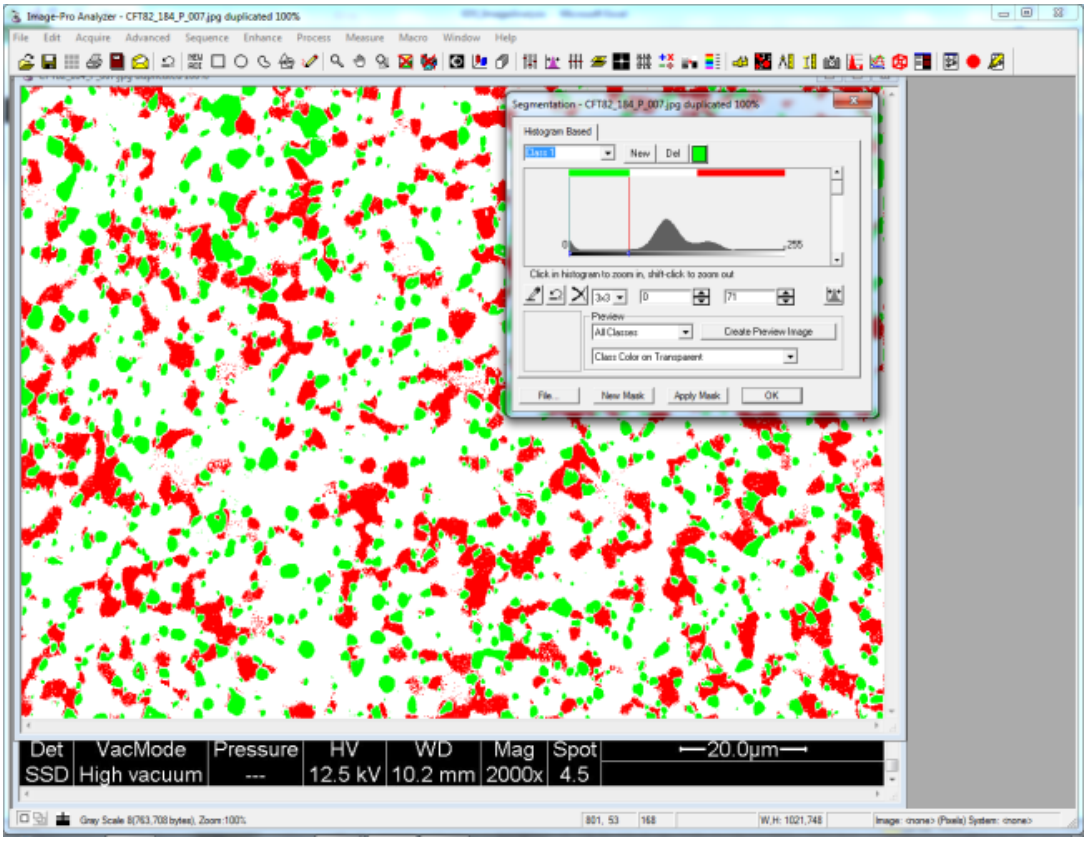

Fig. 2.23 Window of Image-ProAnalyzer 7.0 software took during an image analysis of back-scattered electron micrograph of a polished surface. In particular, through the grayscale histogram (in the inset) it was possible quantify the pores (grey colour), $CoTiO_3$ and Fe_2O_3 (the white colour), and $CoFe_2O_4$ (red colour) amount.

The quantitative XRD phase analysis, using both Rietveld refinement (by using the GSAS-II software [75]) and Reference Intensity Ratio method (RIR), gives results accurate within ~±3wt.% at the 95% confidence level [76]. The accuracy decreases at the increasing of the temperature due to the larger oscillation of the atoms around their average position in the crystal structure. The thermal agitation results in intensity from the peak maxima being redistributed into the peak tails. It does not broaden the FWHM of the diffraction peak, but it does broaden the integral breadth of the diffraction peak. Even if the signal-to-noise ratio decreases at the increasing of temperature, high-temperature XRD

analysis can give a lot of information about the crystal structure especially when a transformation occurs (Fig. 2.24).

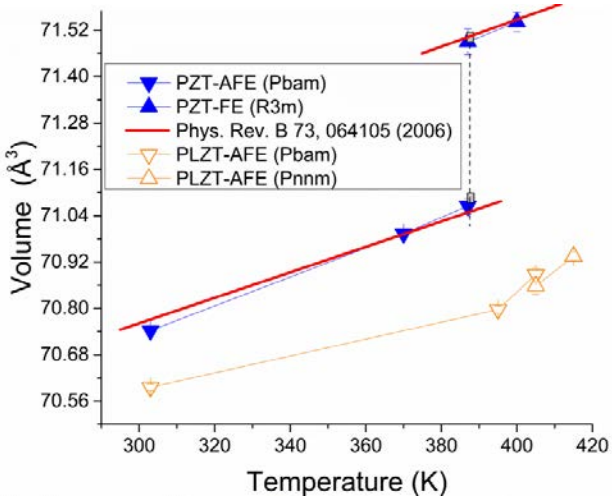

Fig. 2.24 Crystal volume of $PbZr_{0.954}Ti_{0.046}O_3$ (PZT) and $Pb_{0.97}La_{0.02}Zr_{0.954}Ti_{0.046}O_3$ (PLZT) *vs.* temperature [77]. FE and AFE refers to ferroelectric and antiferroelectric behaviour displayed by crystal lattice with R3m and Pbam symmetry, respectively.

For the EDXA, X-ray spatial resolution (the theoretical straight line distance between the incidence point of an electron and its final resting position) depends on the specimen density and overvoltage, and can be estimated through the Kanaya & Okayama's equation:

$$r(\mu m) = \frac{2.76 \times 10^{-2} A E_0^{1.67}}{\rho Z^{0.89}} \qquad \text{Eq. 9}$$

where ρ is the density of the material (g/cm^3), Z is the atomic number, A is the atomic mass and E_0 is the accelerating voltage (keV). An example of EDXA analysis is shown in Fig. 2.25 where the ions diffusion profile, after thermal treatment, was characterized in a thick layered composite which consists in a perovskite $Ba_{0.5}Sr_{0.5}Co_{0.8}Fe_{0.2}O_{3-\delta}$ membrane on a porous alumina substrate [78]. This technique cannot be used to analyze the chemical composition of nanograins embedded into a nanostructured composite. For example, it is not possible to asses if there was an interdiffusion between the two compositions by EDXA analysis in a nanostructure obtained by spark plasma sintering starting from a mixture of soft

and hard ferroelectric perovskites (Fig. 2.26). In fact, using the above equation, the X-ray spatial resolution is

$$r = \frac{2.76 \times 10^{-2} \times 64.4 \times 15^{1.67}}{7.9 \times 27.2^{0.89}} \approx 1\ \mu m \qquad \text{Eq. 10}$$

which covers an ensemble of different nanograins.

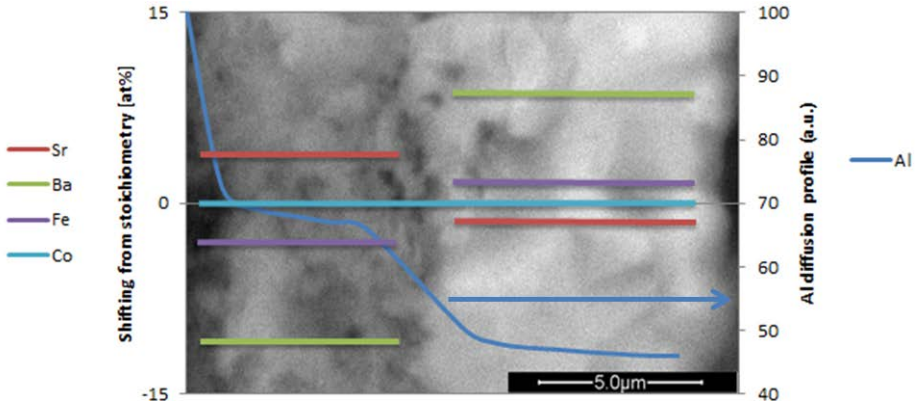

Fig. 2.25 EDAX analysis performed on cross section of thick laminated composite.

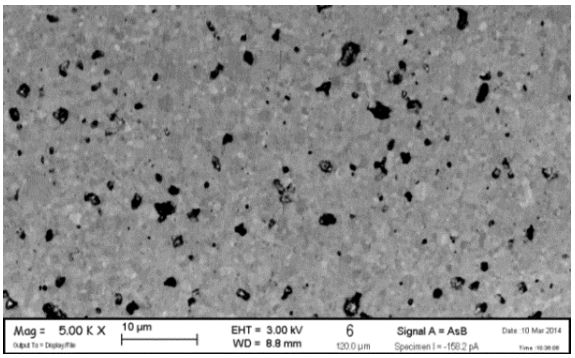

Fig. 2.26 Back-scattered electron micrograph on polished surface of sintered sample by spark plasma sintering starting from a perovskitic powders mixture (50/50 wt%) of PZTN ($Pb_{0.988}(Zr_{0.52}T_{i0.48})_{0.976}Nb_{0.024}O_3$) powder with PZTNMML ($[Pb(Li_{0.25}Nb_{0.75})]_{0.06}[Pb(Mg_{0.33}Nb_{0.67})]_{0.06}[Pb(Zr_{0.50}Ti_{0.50})]_{0.88}O_3$+ 0.7 wt% MnO_2) powder.

For the granulated materials the SEM analysis is the only direct method to measure the particle size – even if the sample preparation is an issue; the particles must be well dispersed and, when the aspect ratio is high, they averagely display their largest side when are deposited on the surface of the sample holder. Sedimentation tests and dynamic light scattering analysis give further information about their behaviour in suspension and size, e.g. as function of their concentration, kind of solvent, and kind/amount of dispersant and binder, or just

the sedimentation kinetic (Fig. 2.27). In fact, although the above analysis should be performed in condition of suspension stability where the particles are completely dispersed and their concentration is low (< 5%), the results shown that particle can be more or less agglomerated (Fig. 2.27).

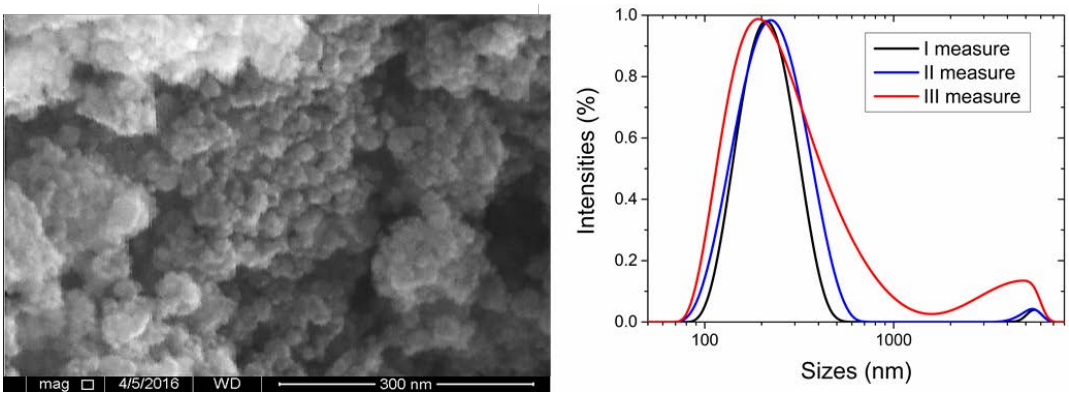

Fig. 2.27 SEM micrograph of planetary milled $CoFe_2O_4$ and related dynamic light scattering analyses, separated by a gap of three minutes, of water suspension with 0.001 wt% of solid content.

A remarkable contribution for the study of the ceramic materials is given by the analyses as a function of temperature. Generally speaking, the thermal analysis cover an ensemble of techniques that measure the physical properties as a function of the settled temperature profile, or determine the release/adsorbed heating amount as a consequence of a physical or chemical transformation. The main thermal analysis were the thermogravimetric analysis (TGA) coupled with the differential scanning calorimetry (DSC).

2.4 Functional characterization

2.4.1 Magnetic characterization

The susceptometer (Sartorius susceptometer YSZ 02C) is based on the interaction between a permanent magnet and the sample placed directly above the magnet the sample. The measured interaction is the change in weight ΔF_z which in turn is correlated to the gradient of the ambient magnetic induction as follows:

$$\frac{\partial B_z}{\partial z} = \frac{\Delta F_z}{m_s} \qquad \text{Eq. 11}$$

where m_s is the magnetic dipole moment of the permanent magnet, B_z is the component of the magnetic induction in the vertical direction and the gradient is evaluated at a distance Z_0 between the center of mass of the permanent magnet and the bottom surface of the sample where there is the maximum field strength to which the sample is subjected by the magnet alone [79]:

$$H_{max} = \frac{m_s}{2\pi Z_0^3} \qquad \text{Eq. 12}$$

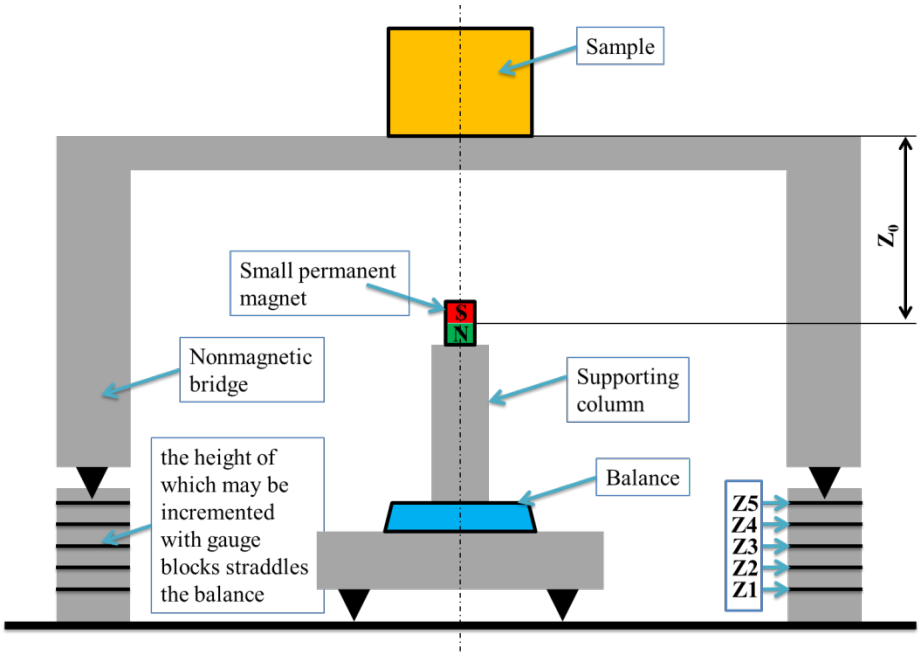

Fig. 2.28 Schematic view of the susceptometer. The sample is placed on the bridge, directly above the magnet at a distance of Z_0. In the case of Sartorius susceptometer YSZ 02C, the distance Z_0 is equal to 18 mm, 20 mm, 27 mm, 35 mm, and 43 mm for Z1, Z2, Z3, Z4, and Z5, respectively.

The maximum value of H_{max} is 2700 A/m (33.9 Oe) when Z_0 is 18 mm. Under this condition of small magnitude of magnetic field strength, the induced magnetization along the z-axis is proportional to H_{max} by the susceptibility, χ, according to the Rayleigh law [31]:

$$\chi H_{max} = \chi_i H_{max} + \alpha H_{max}^2 \qquad \text{Eq. 13}$$

where χ_i is the corresponding field-independent susceptibility, called initial susceptibility, and α is the Rayleigh coefficient. In the equilibrium of magnetic

forces, the permanent magnetization, $M_{p,z}$, and the magnetization induced by the earth's field strength, $\chi H_{E,z}$, can simply be added as terms separate from the induced magnetization by the permanent magnet (Fig. 2.29) [80]:

$$F_z = \frac{3\mu_0 \chi m_s^2}{64\pi Z_0^4} I_a + \frac{\mu_0 (\chi H_{E,z} + M_{p,z}) m_s}{4\pi Z_0} I_b \equiv F_a + F_b \qquad \text{Eq. 14}$$

where I_a and I_b are constants calculated as volume integral with the origin placed in the center of the magnet. The Eq. 14 is a good approximation to first order [79].

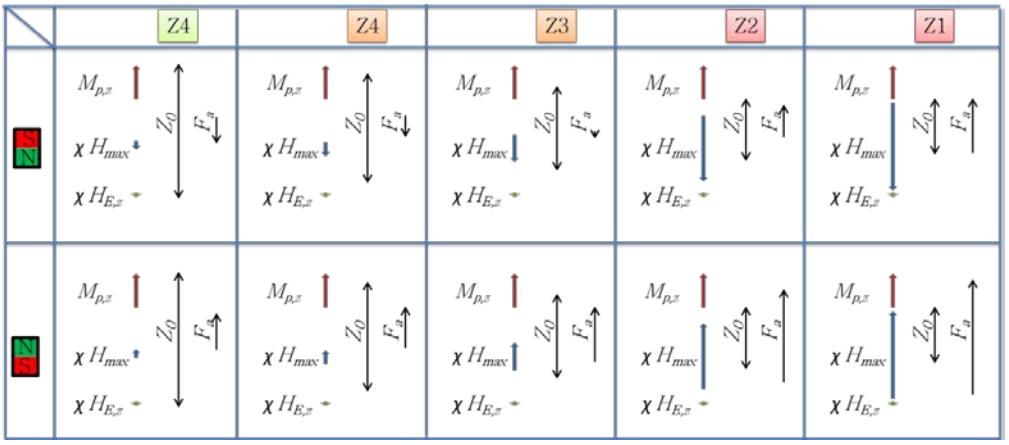

Fig. 2.29 Graphical representation of vectors of the induced magnetization χH_{max} and $\chi H_{E,z}$ by the permanent magnet (H_{max}) and by the earth's field strength ($H_{E,z}$ = 50 A/m ≈ 0.6 Oe), respectively, the permanent magnetization of the sample ($M_{p,z}$), and the weight, F_z, feel by the balance as function the five different distances from the permanent magnet, and its two orientations: [S|N] and [N|S].

In practice, with the susceptometer it is possible to: (i) measure the initial susceptibility and its dependence with the magnetic field in the low field strength range, (ii) measure the permanent magnetization, and (iii) characterize the magnetic behaviour: diamagnetic ($\chi < 0$), paramagnetic ($\chi > 0$), ferrimagnetic ($M_{p,z} \neq 0$). In order to better characterize the magnetic properties, especially the ferro- ferri- antiferro-magnetic and superparamagnetic ones, large magnetic field strength is required. One of the most used magnetometers is the surperconducting quantum interference devices (SQUID). Although the SQUID devices have seen a large degree of improvement, they are basically based on a Josephson junction (superconductor–insulator–superconductor) measurement head and can achieve a

sensibility of 10^{-10} Am^2 (10^{-7} emu) for the measure of the magnetization. By plotting the mass magnetization (M) as a function of field strength in the range between $\pm H > 10^4$ Oe, generally, it is possible to measure the saturation and remnant magnetization (M_s and M_r respectively), the coercive field (H_c) characteristic of the magnetization ($M(H)$) hysteresis loop and other magnetic parameters such as anisotropy and susceptibility.

2.4.2 Electrical characterization

Generally ceramic materials are good insulators or rather they have a dielectric behaviour in an electric field. For the purpose of this thesis work the relevant properties are: (i) the dielectric permittivity and its dispersion in frequency; it depends on the way the material acquires a dipole moment in a static or alternated electric field. (ii) The tangent of the imaginary-to-real part ratio of the dielectric permittivity measures the energy dissipated when the material is subjected to an alternate electric field. (iii) The frequency and intensity of the piezoelectric vibration modes are correlated to the material piezoelectric properties and its geometrical shape ((Fig. 2.30 (c-f))). The vibrational spectrum is complex depending on the sample geometry. e.g. for an axial symmetric sample (a disk) the vibrational spectrum depends on the a diameter-to-thickness ratio, d/t, and the main vibration mode (thickness extensional, radial mode, and planar expander-disk resonance) maximally or minimally excited [81]. Thus the piezoelectric parameters values, determined by piezoelectric resonance as function of the characteristic frequencies (ensemble of anti-resonance: minimum impedance frequency, and resonance: maximum impedance frequency) extracted from the impedance spectrum, can only be calculated for the ceramic materials with a well-defined and suitable geometry. Moreover the piezoelectric materials should present small losses, i.e. the maximum value of the phase angle should approach 90° (loss less condition). (iv) The ferroelectricity study; the last but not the least, since it should be performed before the poling and thus before the collecting the resonance curves of the sample in the |Z|-phase format. In fact, the resonant frequencies can appear only in a poled sample (if polycrystalline). The above mentioned properties can be investigated through the impedance analyser (HP 4194A, Hewlett-Packard) as a function of frequency in the 100 Hz – 1 MHz range and temperature, 230 K – 1200 K. The piezoelectricity can also be investigated by applying a sinusoidal mechanical load, (according with the standard, 0.25 N of amplitude at 110 Hz) by using a d_{33}-meter (S 5865, Sinocera). In order to have a reliable measure, the sample should have an axial symmetry

and exhibit only a piston-type surface displacement, with a dominant single thickness extensional mode. A disk with $d/t > 20$ is generally a good assumption [81]. The large disk diameters allow to reduce the disk edge contribution to the thickness extensional resonance (TER) and resulted in more smoothed spectrum of vibrational modes near the TER.

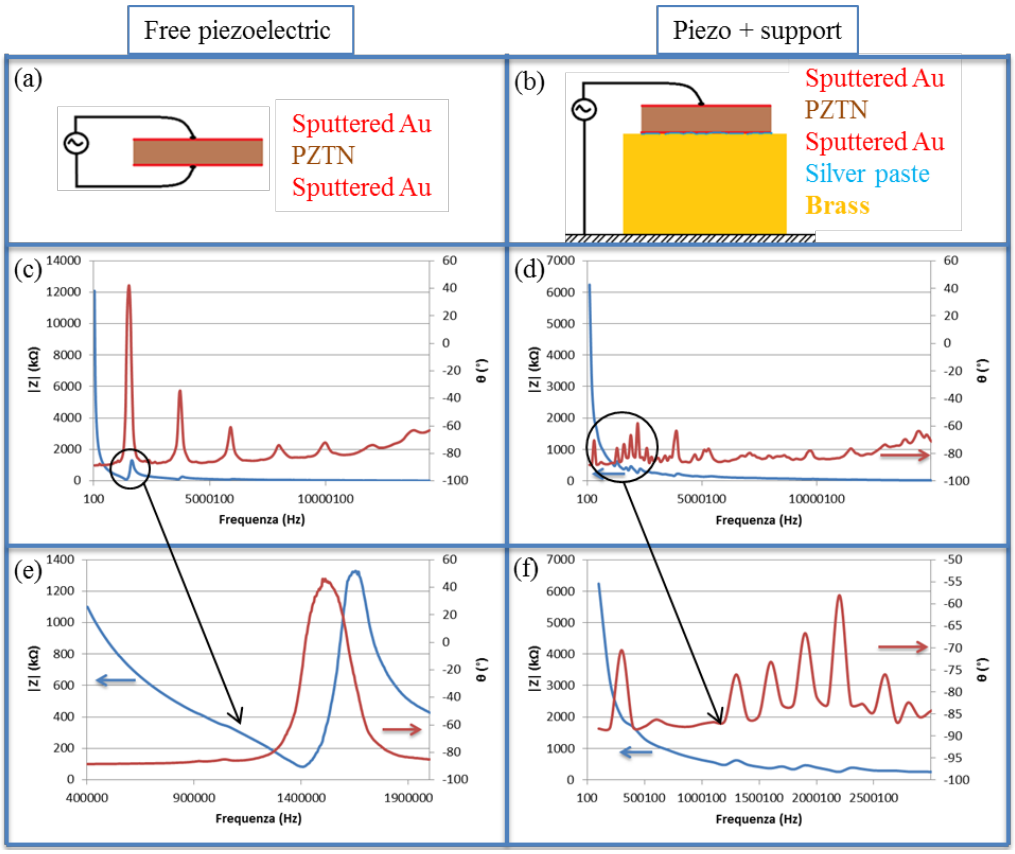

Fig. 2.30 (a and b) Basic setup scheme of the impedance analysis performed on free piezoelectric disk (Fig. 2.22 (b)) and the same free piezoelectric disk glued in a brass disk (Fig. 2.22 (c)). (c-f) Impedance and phase angle vs. frequency. This figure shows a method to determine the resonant characteristics of a piezoelectric element. In particular, the examination of characteristics of Nb-doped lead zirconate titanate (PZTN) ceramic glued on a support can contribute to reducing the resonant frequency. The main methods to reduce the resonant frequency are: (i) glue the disk on a support; (ii) modifying the d/t ratio; (iii) add a mass.

The ferroelectric properties are investigated through the macroscopic electric field dependence of the polarization ($P(E)$) hysteresis loops. The measurements are based on the pulse switching methods on a Sawyer-Tower circuit where the

ceramic sample (a capacitor of unknown capacity, C_x) is in series with a large measurement capacitor integrating current, $C_0 >> C_x$. When an AC signal (produced by a waveform generator, and then amplified by a high voltage amplifier) is applied the reference capacitor C_0 is charged by the same amount of charge as the sample. The nonlinear ($P(E)$) loops are obtained by collecting in an oscilloscope the charge (C_0V_0), divided by the sample area, as function of the applied voltage. The main physical properties that can be measured are the saturation polarization, P_s, the remnant polarization P_r and the coercive electric field E_c.

Chapter 3

Results and discussion

3.1 Ferromagnetic materials[1]

3.1.1 Cobalt ferrite (CF) powders

Spinel $(A)[B]_2O_4$ cobalt ferrite, with the following general structure formula:

$$(Co_{1-i}^{2+}Fe_i^{3+})\left[Co_{i/2}^{2+}Fe_{(2-i)/2}^{3+}\right]_2 O_4^{2-} \qquad \text{Eq. 15}$$

was synthesized using different ceramic processes and conditions that are summarized in Table 1. The parameter *i*, in the Eq. 15, is known as degree of inversion and describes the fraction of the tetrahedral sites (A) (coordination number of four) and octahedral sites [B] (coordination number of six) occupied by Fe^{3+} and Co^{2+} cations, respectively. The reaction yields, η, were calculated with the following equation [31]:

$$\eta = \frac{I_{CoFe_2O_4}(311)}{I_{CoFe_2O_4}(311) + I_{\alpha-Fe_2O_3}(104)} \qquad \text{Eq. 16}$$

where $I_{CoFe_2O_4}(311)$, and $I_{\alpha-Fe_2O_3}(104)$ are the highest diffraction peaks of the spinel cobalt ferrite (ICDD-PDF No. 22-1086) and hematite (ICDD-PDF No. 33-0664), respectively. Eq. 16 can be considered a good approximation since the

[1] The results of this research are reported in the papers:

P. Galizia, C. Baldisserri, C. Capiani, C. Galassi «Multiple parallel twinning overgrowth in nanostructured dense cobalt ferrite» *Mater. Design* 109 (2016) 19-26.

M. Cernea, P. Galizia, I. V. Ciuchi , G. Aldica, V. Mihalache, L. Diamandescu, C. Galassi «$CoFe_2O_4$ magnetic ceramic derived from gel and densified by spark plasma sintering» *J. All. Comp.* 656 (2016) 854-862.

P. Galizia, M. Cernea, V. Mihalache, L. Diamandescu, G. Maizza, C. Galassi « Easy batch-scale production of cobalt ferrite nanopowders by two-step milling: structural and magnetic characterization» *Mater. Design* (Accepted 2017)

mass absorption of the two phases is only slightly different. It can be seen that *sol-gel* synthesis allows to reduce the calcination temperature for equal reaction yield. On the other hand *sol-gel* synthesis is less reliable than solid state synthesis, as shown by the higher reaction yield obtained with a smaller soaking time. This unexpected result is due to the difficulty to control the gelation which can lead to flocks or crystalloids. The former are characterised by high specific surface area and reduced interdiffusion distance, conversely for the latter. For the same reason it was possible to achieve η = 100 % starting with nanosized raw materials calcined at 850 °C for 2 h, and only η = 80 % and 93 % starting with micrometric raw materials even if the calcination time was longer: 4 h and 12 h , respectively. It is worth highlighting that the field of stability is [740.5 °C, 1451.5 °C] for stoichiometric cobalt ferrite (Fig. 3.1), and at least an error of 2 wt% should be taken into account in the weighing of Co_3O_4 powder (-0.13 g for each theoretical gram) in order to stabilize the hematite at 850 °C.

Besides small crystallite size (76 nm), the synthesized cobalt ferrite displays coarse, partially sintered, and low-reacting powders already upon reaction at 700 °C, with agglomerate size as large as 60–80 μm (Fig. 2.3 and Fig. 2.4), which requires a milling step prior to cold consolidation. In Table 2 the milling parameters together with the powder characteristics are shown. Planetary milling proved to be quite efficient in reducing crystallite, particle, and agglomerate size.

Table 1 Correlation between sample ID, process synthesis method and parameters, and reaction yield (η). In the sample ID the subscripts: $_{sg}$, $_{ss}$, $_{(n)}$, and $_{(\mu)}$, refer to *sol-gel* synthesis, solid state synthesis, nanosized raw materials, microsized raw materials, respectively.

Sample ID	**Synthesis method**	**Calcination temperature (°C)**	**time (h)**	**η (%)**
$CF_{sg}7^{1}$	Sol-gel	700	1	96
$CF_{sg}7^{3}$	Sol-gel	700	3	91
$CF_{ss(n)}7^{4}$	Solid state reaction	700	4	80
$CF_{ss(n)}8^{4}$	Solid state reaction	800	4	91
$CF_{ss(n)}8^{4+2}$	Solid state reaction	800	2	93
$CF_{ss(n)}8_5^{2}$	Solid state reaction	850	2	100
$CF_{ss(n)}10^{4}$	Solid state reaction	1000	4	100
$CF_{ss(\mu)}8_5^{4}$	Solid state reaction	850	4	80
$CF_{ss(\mu)}8_5^{4+8}$	Solid state reaction	850	8	93
$CF_{ss(\mu)}10_5^{4}$	Solid state reaction	1050	4	100

Size reduction displayed a quite unexpected trend, as both the crystallite size and the agglomerate size resulted smaller for the powder treated at higher temperature. This result was justified using the Weibull statistic and Hertz theory for the contact of elastic bodies [31]. The higher probability of critical defects, as well as to the higher stresses concentrated into the larger particles during the milling treatment, cause the particles fracture into smaller pieces. In fact, it is well known that the breakage rates are exponentially correlated to the particle diameter, and depend on the minimum energy which can be stored in the particle without breakage [82,83].

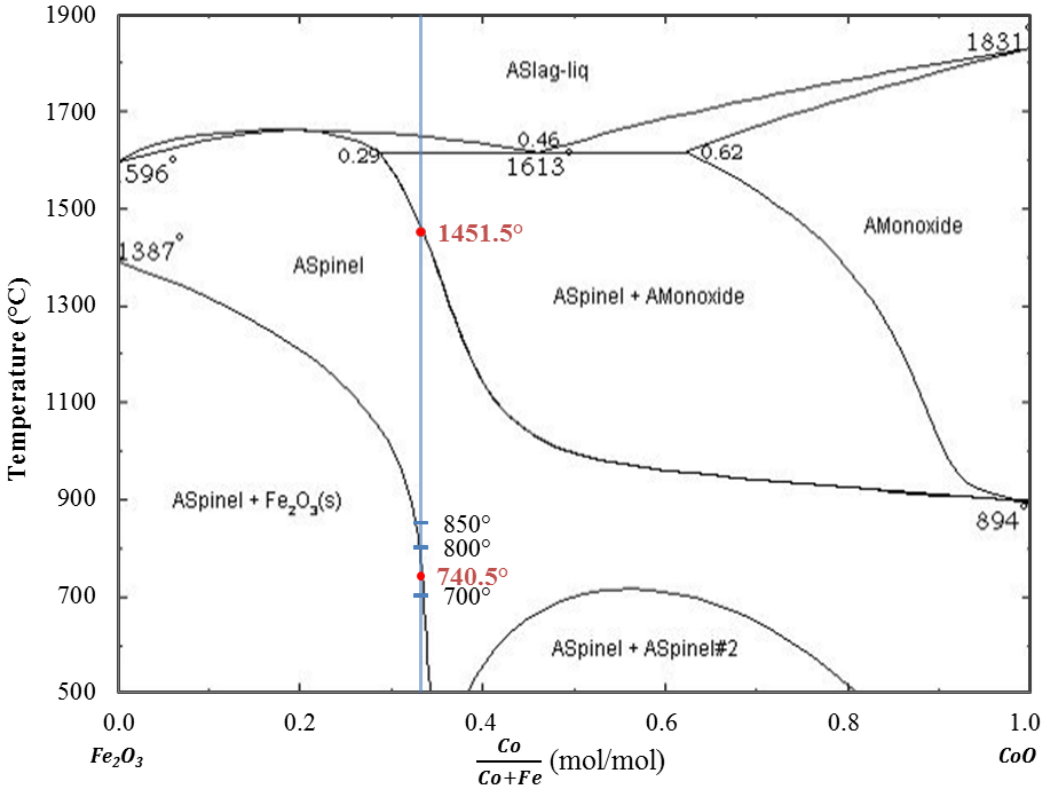

Fig. 3.1 Phase diagram of Fe – Co – O_2, p(O_2) = 0.21 atm, system.

The extrinsic (d_{nl}, d_{nV}, crystallite size: D) and intrinsic (i) effects of milling treatments on the cobalt ferrite strongly affect its magnetic properties. In particular the coercivity (H_c) value is mainly affected by the crystallite size (Fig. 3.3). The maximum H_c value was reached when D became close to the single-domain limit, about 28 nm. For smaller D values, H_c approaches to zero and should be zero under the supeparamgentic limit (about 6 nm).

The trend of coercivity *vs.* temperature is influenced by the effective anisotropy (K_{eff}) which in turn is strongly affected by both strain level and crystallite size, according with the following equation [84]:

$$K_{eff} = \sqrt{K_1^2 + K_s^2} \qquad \text{Eq. 17}$$

where K_1 is cubic anisotropy costant, and K_s is the stress anisotropy. The former can be estimated through a nonlinear fitting of magnetic hysteresis ($M(H)$) near the saturation ($0.97\ M_s < M < M_s$) according with the following equation [85]:

$$M = M_s\{1 - 8/105\ [K_1/(M_sH)]^2 - 4/105\ [K_1/(M_sH)]^3\} + \kappa H \qquad \text{Eq. 18}$$

Table 2 Correlation between sample ID, planetary milling set-up, and powder characteristics. All the powders were milled using a Fritsch Pulverisette 6 machine, stainless steel jar, spherical zirconia milling media, and a rotational speed of 400 rpm. The crystallite size (D) and strain (ε) were calculated through the Rietveld refinement (stopped when $\chi^2 < 1.18$).

Sample ID	**Milling time (h)**	**Jar radius (cm)**	**Milling media (mm)**	**Balls/ Powder (wt/wt)**	**Strain, ε (%)**	**Crystallite Size, D (nm)**	**d_{nl} (µm)**	**d_{nV} (µm)**	**R (Eq.5)**
$CF_{sg}7^1$	0	-	-	-	-	-	-	-	-
$CF_{sg}7^1$-25	25	32.5	1	5.5	-	25	-	-	-
$CF_{sg}7^3$	0	-	-	-	-	-	-	-	-
$CF_{sg}7^3$-25	25	32.5	1	12.6	-	10	-	-	-
$CF_{ss(n)}8^{4+2}$	0	-	-	-	-	76	25.4	35.5	-
$CF_{ss(n)}8^{4+2}$-5	5	37.5	5	10.5	-	59	22.4	28.6	2.3
$CF_{ss(n)}8^{4+2}$-10	10	37.5	3	10.5	-	55	18.8	23.9	1.3
$CF_{ss(n)}8^{4+2}$-15	1	37.5	2	10.5	-	36	17.5	22.0	1.5
$CF_{ss(n)}8^{4+2}$-20	20	37.5	1	10.5	-	27	14.8	17.7	1.6
$CF_{ss(n)}8_5^2$	0	-	-	-	-	71	28.7	38.4	-
$CF_{ss(n)}8_5^2$-25	25	37.5	1	5.5	-	20	12.7	18.2	1.3
$CF_{ss(n)}10^4$	0	-	-	-	-	>100	29.4	34.7	-
$CF_{ss(n)}10^4$-25	25	37.5	1	6.5	-	13	11.0	16.1	1.0
$CF_{ss(\mu)}8_5^{4+8}$	0	-	-	-	0.1	>100	-	-	-
$CF_{ss(\mu)}8_5^{4+8}$-12	12	37.5	5	11.2	2.0	31	-	-	-
$CF_{ss(\mu)}8_5^{4+8}$-40	28	37.5	1	14.0	0.6	12	-	-	-
$CF_{ss(\mu)}10_5^4$	0	-	-	-	0.0	>100	-	-	-
$CF_{ss(\mu)}10_5^4$-12	12	37.5	5	11.2	2.1	33	-	-	-
$CF_{ss(\mu)}10_5^4$-40	28	37.5	1	14.0	1.2	9	-	-	-

In the above Eq. 18, κH is the forced magnetization, also called the paramagnetism-like term, caused by an increase in the spontaneous magnetization itself and proportional to high-field susceptibility, κ. The stress anisotropy is related to the residual strain as:

$$K_s = \frac{3}{2}\lambda\varepsilon E \qquad \text{Eq. 19}$$

Fig. 3.2 Photo-reportage of the multi-step (two-step) planetary milling of cobalt ferrite powders: 1°) stainless steel jar (r = 37.5 mm) filled with zirconia milling media (ϕ = 5 mm); 2°) addition of $CF_{ss(\mu)}8_5^{12}$ powder; 3°) fixing planetary milling system; 4) setting planetary milling parameters; 5°-9°) $CF_{ss(\mu)}8_5^{12}$-12 powder recovery; 10°) stainless steel jar (r = 37.5 mm) filled with zirconia milling media (ϕ = 1 mm); 11°) addition of $CF_{ss(\mu)}8_5^{12}$-12 powder and pure ethanol; 12°) setting planetary milling parameters; 13°-15°) $CF_{ss(\mu)}8_5^{12}$-40 powder recovery.

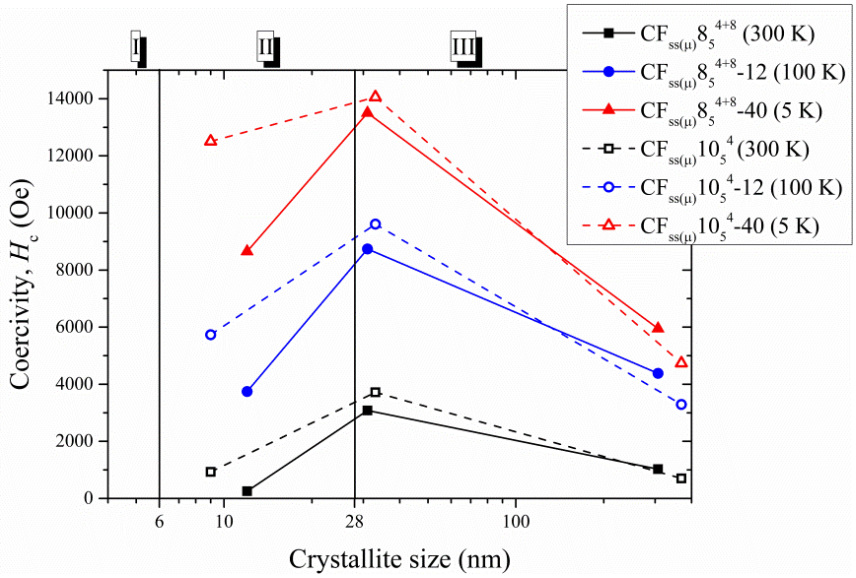

Fig. 3.3 H_c dependence on crystallite size at various temperatures for: $CF_{ss(\mu)}8_5^{4+8}$ series (solid lines) and $CF_{ss(\mu)}10_5^{4}$ series (dashed lines). The superparamagnetic region, the single domain region, and the multi-domain region are labeled with I, II, and III, respectively.

where λ and E are the average magnetostriction constant and the Young's modulus, respectively. From the temperature dependence of the coercive field (Fig. 3.4) it can be seen that the first milling treatment increases the uniaxial anisotropy as the H_c *vs.* T experimental points are very well fitted by $H_c = a - bT^{3/4}$ which describes the behaviour of many randomly oriented single-domain magnetic particles presenting uniaxial anisotropy ($K_s >> K_1$) [86]. The second milling treatment further reduces the exponential coefficient and the temperature dependence of coercivity could be expressed in terms of $T^{1/2}$, i.e., $H_c = a - bT^{1/2}$, indicating that CF nanoparticles may form a system with the easy directions of the particles oriented parallel to the magnetic field [86], as expected, since for smaller particles, coherent rotation is predominant whereas for larger particles the development of domain walls is favourable [87].

The milling treatment, by changing the extrinsic properties, acts also on the magnetic moment of the powders. In particular, from the Fig. 3.5, it can be seen a significant departure from the Néel-type collinear magnetic order (spin-canting angle, ϕ = 0 °) at the decreasing of the crystallite size and increasing of strain level. This causes the cation distribution rearrangement (i) as result of the physical state of cobalt ferrite: size (D) and strain (ε). Thus the spin-canting angle can be written in function of D and ε, as follows:

$$\phi \propto c\phi_0\left[\left(e^{t/D}-1\right)+\left(e^{\gamma\varepsilon}-1\right)\right] \qquad \text{Eq. 20}$$

where ϕ_0 is the value of spin-canting angle at i = 0, t is the thickness of dead layer, and c and γ are constants. It was found that: for the powders milled only one time ($CF_{ss(\mu)}10_5^4$-12), with crystal size close to the single domain limit (Fig. 3.3), the strain contribution accounts for 76 % in moving from the Néel model, and its weight drops to 31 % after the second milling step ($CF_{ss(\mu)}10_5^4$-40) where the powders are less able to arrange microstrain and display a crystallite size close to the superparamagnetic limit (Fig. 3.3).

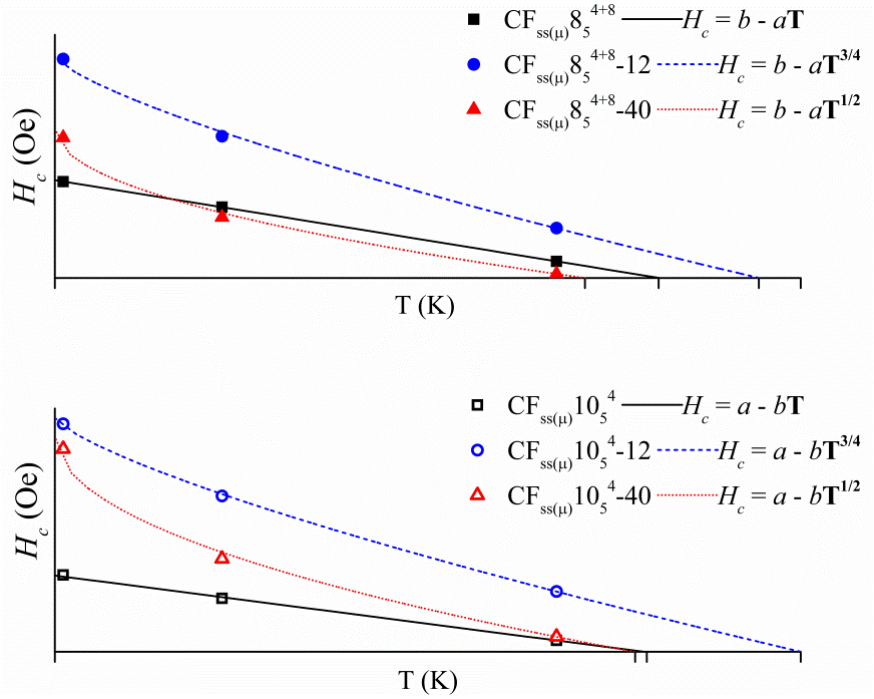

Fig. 3.4 Variation of the coercive force (H_c) with temperature (T) for $CF_{ss(\mu)}8_5^{4+8}$ and $CF_{ss(\mu)}10_5^4$ series.

Another main role is played by the magnetic inhomogeneity such as the twinning boundaries, which act as pinning centers for the hindrance of magnetic domain wall movement across the easy axes [31]. Also the density and the characteristic of such magnetic inhomogeneity can by changed by the milling treatment. In particular, through the milling treatment it is possible to decrease the amount of the planar inhomogeneities (average half width of the magnetic inhomogeneities, r_0, larger than domain wall width, δ_B) such as the high amount of twinning boundaries that are present in the as calcined powders (Fig. 2.2). At

the decreasing of the twinning boundaries amount an increase of magnetic inhomogeneities with the size smaller than the domain wall width (thin planar inhomogeneities, $r_0 < \delta_B$) occurs. This change can be checked through the H_c(T)/M_s(T) ratio, which is linearly correlated to $K_1^{3/2}$(T)/M_s^2(T), and $K_1^{1/2}$(T)/M_s^2(T) when the coercivity is controlled by $r_0 > \delta_B$, or $r_0 < \delta_B$, respectively [84].

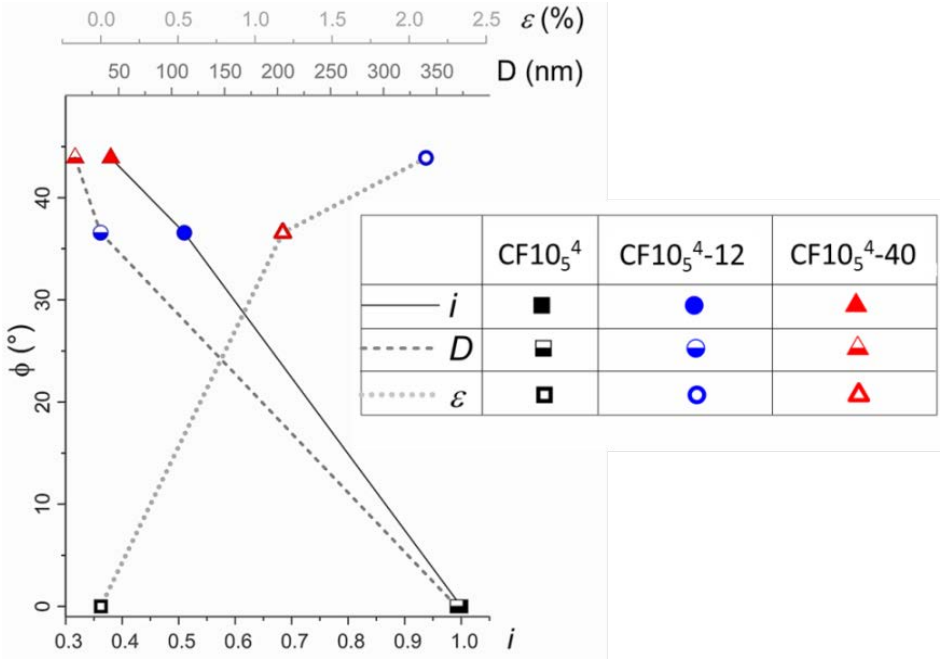

Fig. 3.5 The variation of spin-canting angle ϕ with i (solid line); and the variation of ϕ angle as function of the measured crystallite sizes and strains (dashed line with half-open and open symbols, respectively).

3.1.1 CF bulks

All the above powder properties (i.e. amount of unreacted precursors, crystallite size, strain level, particle size density distribution broadening, etc.) can improve or hinder the next ceramic process steps. For the production of dense bulk ceramic, the high energy of nanopowders adsorbed during the milling treatment, as strain or increased specific surface area, can lead to a better sinterability and higher final density. On the other hand the nano- and/or work-hardened $CF_{ss(\mu)}8_5^{4+8}$-40 and $CF_{ss(\mu)}10_5^4$-40 powders, since their poor ability to arrange plastic deformation, display bad cold compaction behaviour with the onset of lamination that will lead to the cracking during the sintering treatment, especially if done at high heating rate (Fig. 3.6). It is worth to notice that the

pieces of the sample sintered by quite fast sintering (Fig. 3.6 (a)) display a full density in contrast of 97.5 ±0.5 % achieved by the sample sintered in conventional way (Fig. 3.6 (c)). After granulation with water the milled powders showed behaviour similar to the as-calcined ones both during shaping and sintering. Although it was easier to shape the granulated powders, and the green samples did not show any lamination, the final densities were lower: 95.5 ±0.5 %.

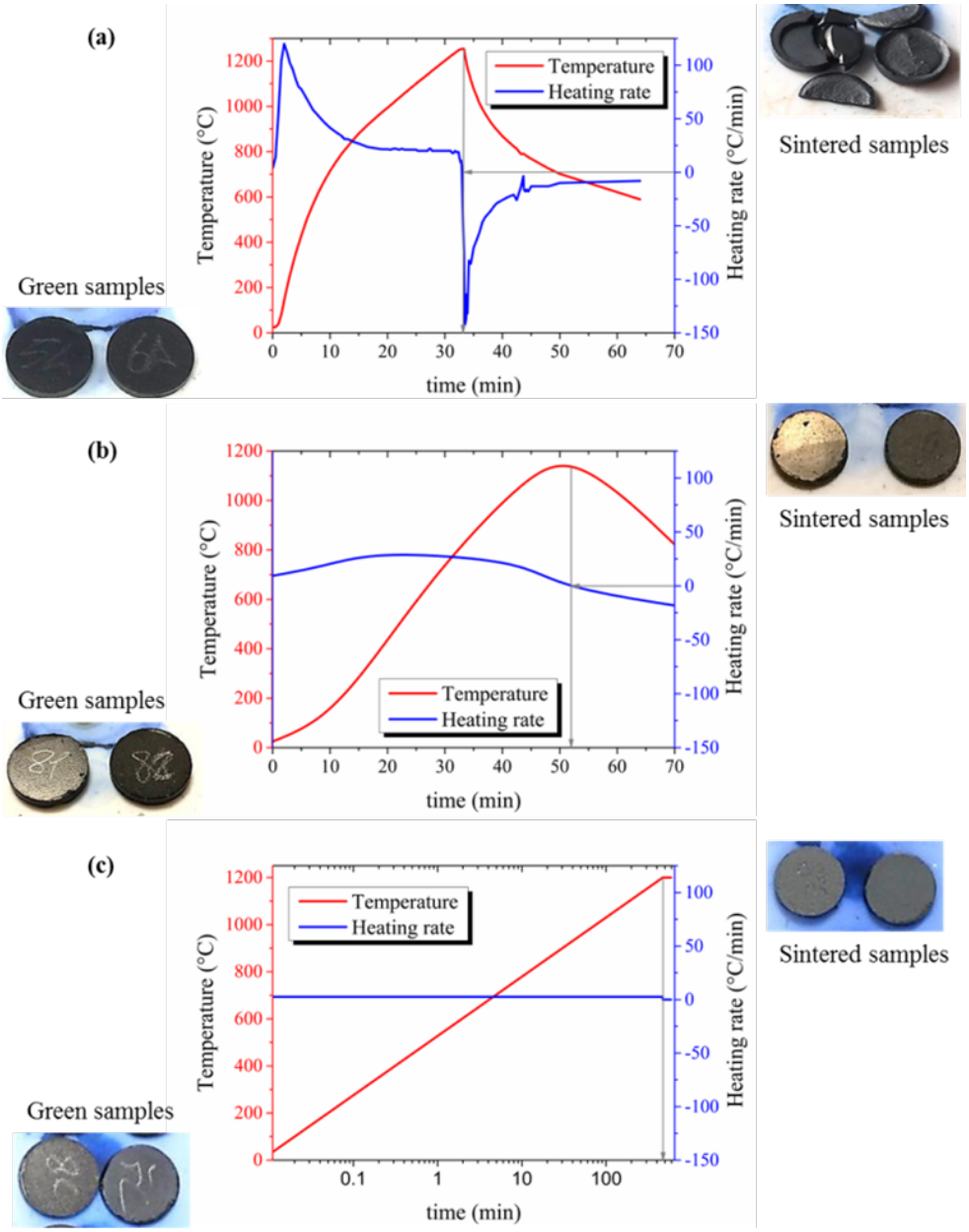

Fig. 3.6 (a and b) quite-fast sintering and (c) conventional sintering of $CF_{ss(\mu)}8_5^{4+8}$-40 and $CF_{ss(\mu)}10_5^{4}$-40 powders.

In order to exploit the high energy contained inside the milled nanopowders and avoid the lamination during the extraction of the green body from the die linear pressing, the Spark Plasma Sintering (SPS) can be the right process, since a load is kept during all the sintering process for a very short time (Fig. 3.7).

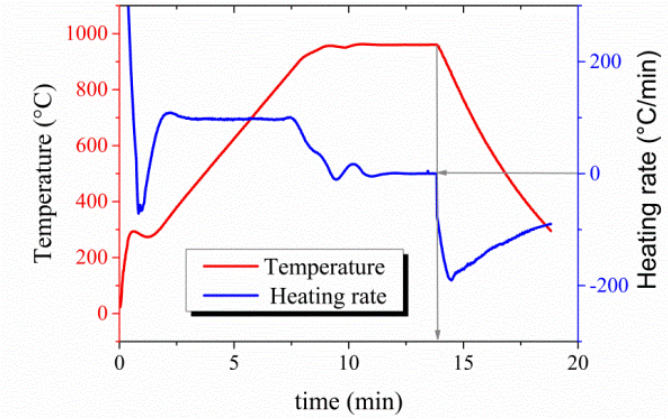

Fig. 3.7 Temperature and heating rate profiles collected by FCT/Germany SPS equipment and applying a pulsed current (on: 0.003 s; peak: 1600 A and 5 V). A pressure of 63 MPa was applied on the sample with thickness of about 2 mm and diameter of 20 mm.

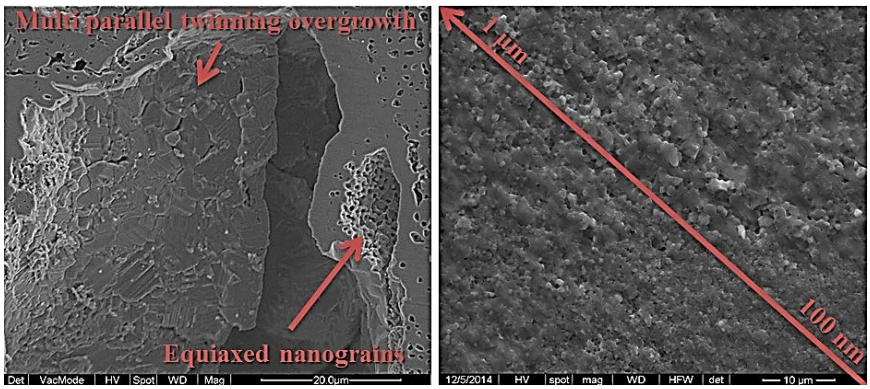

Fig. 3.8 Electron micrographs of a polished surface (left) and a fracture surface (right) of dense cobalt ferrite sintered by SPS at 950 °C for 5 min (Fig. 3.7) using $CF_{sg}7^3$ powders (Fig. 2.4).

Owing to the very short sintering time and low temperature the starting powders should be as homogenous as possible. In fact, each inhomogeneity of the starting powder will result in an inhomogeneity in the final microstructure (Fig. 3.8). By using the milled powders, it is possible to increase the homogeneity as well as the sinterability at lower temperatures. i.e. $CF_{sg}7^1$ powders sintered by SPS at 950 °C for 5 min (Fig. 3.7) get a relative density of 96.9 ±0.1%; $CF_{sg}7^1$-25

powders sintered by SPS at 830 °C for 5 min get a relative density of 99.2 ±0.2%. This remarkable result: 99% of relative density at 830°C for 5 min was not achieved with $CF_{ss(n)}10^4$-25 which get only 96%. Further, in order to get high density values unreacted starting oxides must be avoided. In particular, the unreacted Co_3O_4 results into oxygen evolution during sintering and consequently can leave spherical pores (Fig. 3.9), according to the following reactions:

$$2Co_3O_4 + 6Fe_2O_3 \rightarrow 6CoFe_2O_4 + O_{2(g)} \qquad \text{Eq. 21}$$

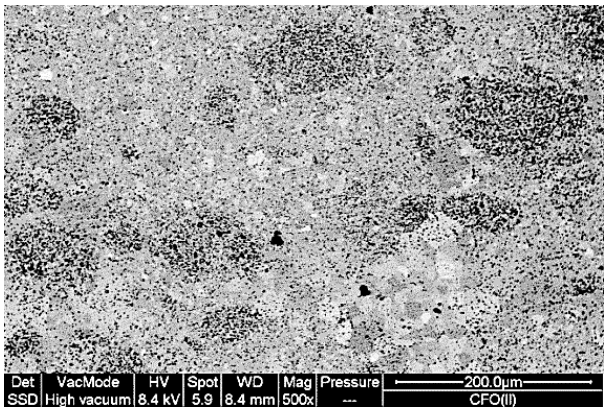

Fig. 3.9 Back-scattered image of polished bulk cobalt ferrite sintered at 1240 °C for 2 h starting with $CF_{ss(n)}7^4$ powders.

By starting with homogeneous powders, such as $CF_{sg}7^1$-25 (Fig. 2.5), and $CF_{ss(n)}10^4$-25 (Fig. 3.10), it was possible to tailor the microstructure evolution during sintering by setting different heating profiles. In particular, it was used the two-step sintering in order to simulate the high densification at low temperatures (those used in the SPS), and the quite fast sintering in order to exploit the high reactivity of the milled powders, and the conventional sintering for comparison. The heating profiles are shown in Fig. 3.11. It was found that there was no densification by two-step sintering at 830 °C for both powders (Fig. 3.12 and Fig. 3.13), even if the heating rate to reach the maximum temperature is comparable with that of SPS. The densification was improved with the two-step sintering at 950 °C and a relative density of 83% and 93% was achieved with the $CF_{ss(n)}10^4$-25 and $CF_{sg}7^1$-25 powders, respectively. Good densification was achieved with both quite-fast sintering and conventional sintering. In particular, by the quite fast sintering $CF_{ss(n)}10^4$-25 and $CF_{sg}7^1$-25 powders achieve 96.2 ±0.2% and 96.3 ±1.3%, respectively. Relative densities close to that achieved by conventional sintering: 94.9 ±0.3% and 97.7 ±0.6%, respectively. From the Fig. 3.12 (SEM morphology of the CF sintered microstructures from *sol-gel* powder) and Fig.

3.13 (SEM morphology of the CF sintered microstructures from SSR powder) it can be seen that microstructure evolution is slightly different: (i) after the two-step heating treatment the $CF_{sg}7^{1}$-25 sample displays euhedral nanograins (about 150 nm) with octahedral crystal habit, while $CF_{ss(n)}10^{4}$-25 sample displays anhedral grains with a wide particle size distribution: 10 nm – 400 nm. (ii) The microstructure obtained by quite-fast sintering is an intermediate between the euhedral grains and the multiparallel-twinned overgrown grains [31] for $CF_{sg}7^{1}$-2 sample (Fig. 3.12), and a mixture of euhedral and multiparallel-twinned overgrown grains for the $CF_{ss(n)}10^{4}$-25 sample (Fig. 3.13). (iii) After conventional sintering both samples display the same microstructure that consists in multiparallel-twinned overgrown grains.

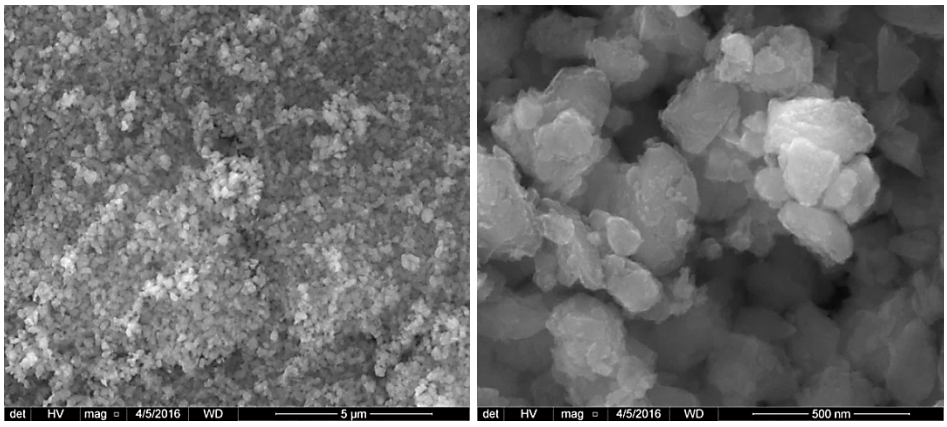

Fig. 3.10 SEM images of $CF_{ss(n)}10^{4}$-25 powders

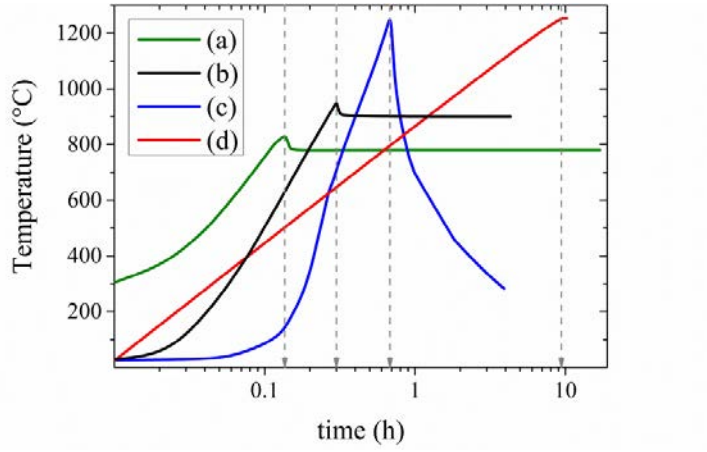

Fig. 3.11 Heating profile of (a) two-step sintering with peak at 830 °C and 17 h of soaking time at 780 °C; (b) two-step sintering with peak at 950 °C and 4 h of soaking time at 900 °C; (c) quite-fast sintering at 1250 °C; and (d) conventional sintering at 1250 °C for 2 h.

The microstructure evolution, and in particular, the amount of multiparallel-twinned grains (in the following, their volume fraction, measured by image analysis, is indicated with G_{MPT}) was tailored using cobalt ferrite powder with different starting crystallite size. G_{MPT} of 0.830, 0.958, and 0.997 vol/vol was obtained after sintering at 1200 °C for 2 h the $CF_{ss(n)}8^{4+2}$-20, $CF_{ss(n)}8_5^{2}$-25, and

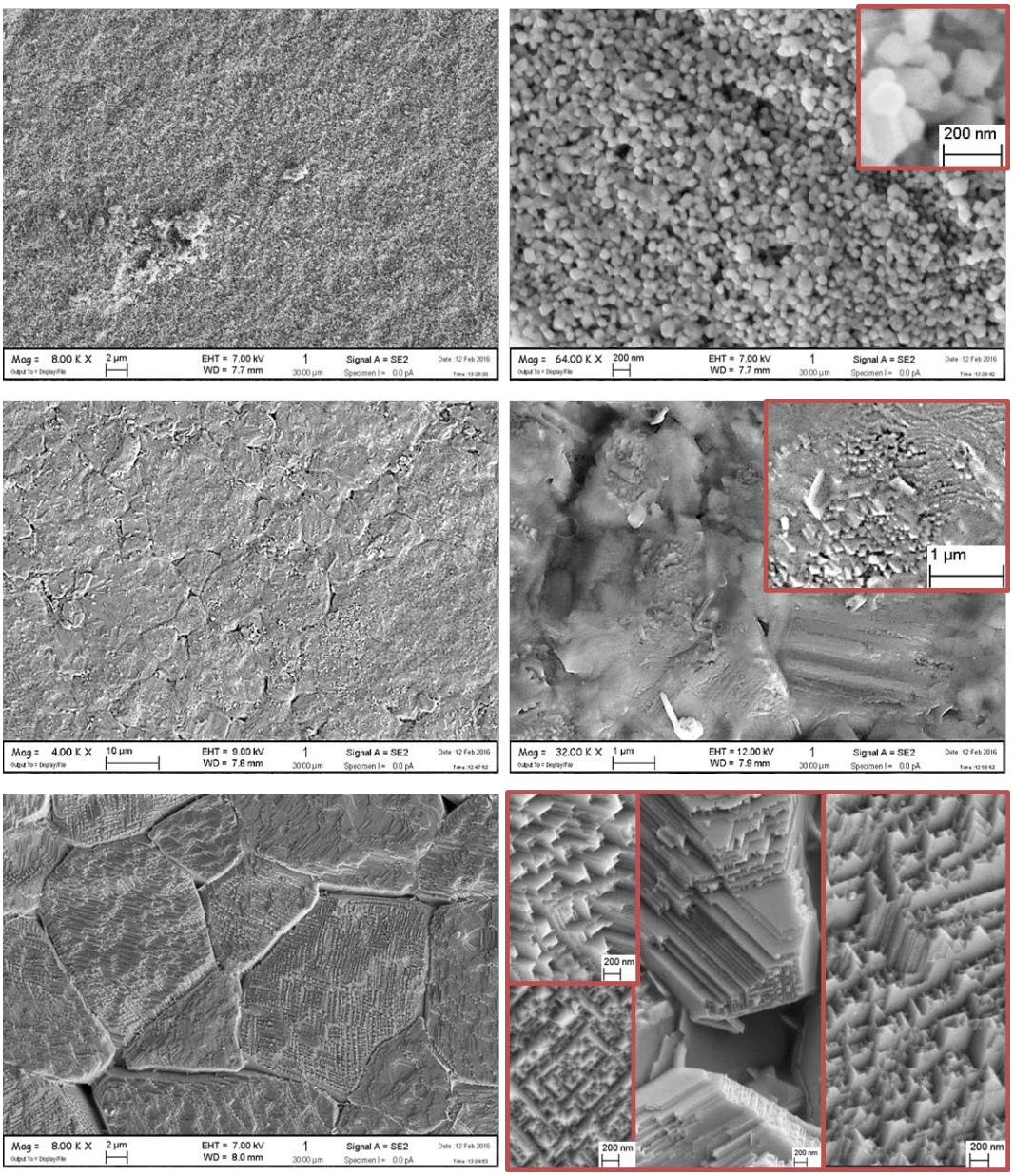

Fig. 3.12 SEM images of $CF_{sg}7^{1}$-25 powders sintered by two-step sintering 830°C+780°Cx4h (first row); quite-fast sintering at 1250°C (second row); and conventional sintering at 1250°Cx2h (third row).

$CF_{ss(n)}10^4$-25 powders, respectively. A correlation is evident between the reactivity/granulometry of cobalt ferrite particle with the tendency to multi parallel twinning overgrowth during sintering [31]. An important result was achieved by studying the magnetization at low magnetic field strength of the above sintered samples with different G_{MPT} values. In Fig. 3.14 (a) the results of the total magnetization read by the susceptometer at different

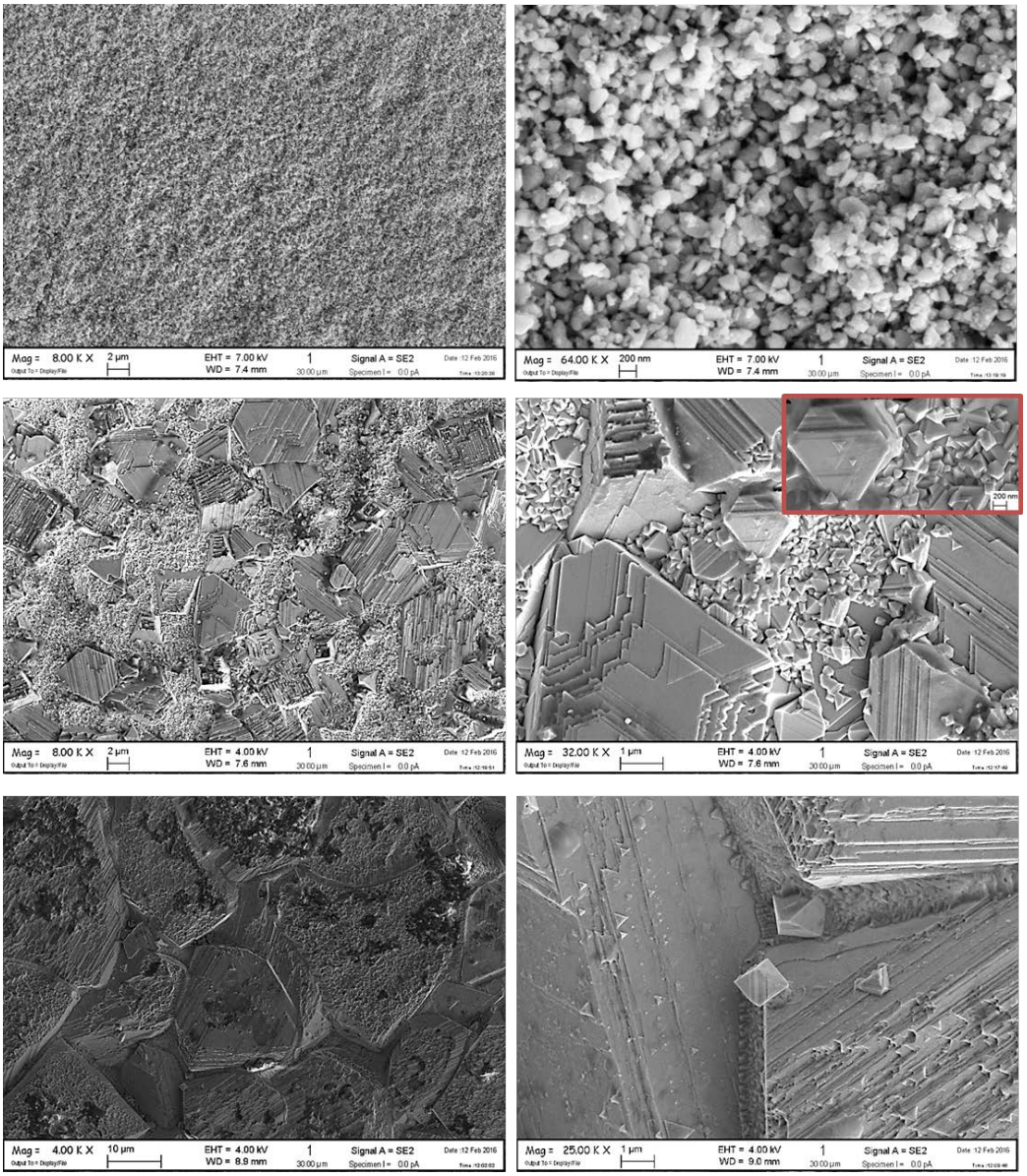

Fig. 3.13 SEM images of $CF_{ss(n)}10^4$-25 powders sintered by two-step sintering 830°C+780°Cx4h (first row); quite-fast sintering at 1250°C (second row); and conventional sintering at 1250°Cx2h (third row).

distances (*alias* different magnetic field strength) is plot as fitting of experimental data by the Rayleigh law (Eq. 13). Fig. 3.14 (a) shows that the induced magnetization decreases as G_{MPT} increases. In particular, the sample with the highest G_{MPT} (0.997) displays the lowest χ_i (0.3) and a weak contribution of the field-dependent term of susceptibility (αH, α = 1.6 x 10^{-6} m A^{-1}). A remarkable increase of both χ_i and α, up to 0.9 and 9.2 x 10^{-5} m A^{-1} respectively, was achieved by reducing G_{MPT} down to 0.83. In order to show the effect of G_{MPT}, χ_i, and αH contribution on the measured susceptibility according to the field intensity, the Fig. 3.14 (b) was constructed showing the total volume susceptibility ($\chi = \chi_i + \alpha H$) vs. field intensity (H) and the volume fraction of multiparallel-twinned grains (G_{MPT}). It can be seen in Fig. 3.14 (b) that there is a linear correlation between χ_i and G_{MPT} (the line at H = 0 on the G_{MPT}-χ_i plane). In particular, χ_i decreases as G_{MPT} increases. The contribution αH on the measured susceptibility is negligible, $\chi_i \approx \chi$, at G_{MPT} = 0.997 (the gray line almost parallel to the G_{MPT}-H planes, and perpendicular to the G_{MPT}-χ_i planes), but it increases with decreasing G_{MPT} as can be seen from the increase of the slope projected by the gray curves on the H-χ_i plane. In particular the ratio of the αH term to the χ at the field intensity of 2700 A m^{-1} ($\alpha H/\chi_{2700}$) is 0.01, 0.15, and 0.22 when G_{MPT} is equal to 0.997, 0.958, and 0.83, respectively [31]. The reduction, about 67%, of the effective volume susceptibility proofs that multiple parallel twinning enhances the hard magnetic behaviour and suggests an extension of Globus model. In fact, the variation of χ_i can be explained on the basis of Globus model based on the assumption that domain walls are pinned at grain boundaries and reversible wall motion is caused by wall bulging under application of a magnetic field until a critical value, H_{cr}, is reached (Fig. 3.15 (a)) at which the wall gets unpinned [88]. In this model the linear correlation between the initial susceptibility (χ_i) and the mean grain diameter (D_m) is expressed as:

$$\chi_i = \frac{2\pi M_s^2 D_m}{K} \qquad \text{Eq. 22}$$

where K is the global anisotropy, composed of the magnetocrystalline anisotropy and the magnetoelastic anisotropy, and M_s is the saturation magnetization. According to this model χ_i is proportional to the average grain diameter (D_m). But in the case of cobalt ferrite, such model has to be extended to the case where the domain walls are pinned at twinning boundaries and D_m can be interpreted as the distance between the twinning boundaries (t), i.e. the span of the domain wall (Fig. 3.15 (b)). Since, in spite of the fact that the grain size increases with increasing calcination temperature, the initial susceptibility decreases owing

to multiple parallel twinning overgrowth [31]. From the experimental linear correlation Fig. 3.14 (b), it is possible to calculate the different contribution of multiple-twinned grains on the total initial susceptibility (χ_i) and the Rayleigh coefficient (α) using the mixing rule:

$$\chi_i = aG_{MPT} + b(1 - G_{MPT}) \qquad \text{Eq. 23}$$

$$\alpha = cG_{MPT} + d(1 - G_{MPT}) \qquad \text{Eq. 24}$$

where *a*, *b*, *c*, and *d* are constants whose values are 0.3, 3.9, 1.6 x 10^{-6} $A^{-1}m$ and 5.3 x 10^{-4} $A^{-1}m$ respectively. In this way it is possible to estimate the magnetic behaviour as a function of whole G_{MPT} domain [0,1] (Fig. 3.16). Therefore, in order to apply the Globus model to the macroscopic magnetization of a spinel ferrite, it is not enough to simply measure the sample's grain size, but the contribution of multiple parallel twinning must be taken into account. When $D_m > t$, the multiparallel-twinned grains are less susceptible to the applied magnetic field while the other grains (having not so high a density of twin boundaries in the volume of the grain) display higher susceptibility. These results are quite important because suggest the possibility of producing bulk cobalt ferrite characterized by a nano-sagenite network where the distance between the twin boundaries is comparable to, or lower than, a single domain (Fig. 3.17). The possibility of tuning the magnetic behaviour from a multidomain to a single domain scale allows bulk cobalt ferrite to be competitive with its nanoparticles, while keeping the advantages of bulk ceramics [31]. This powerful feature substantially increases the versatility of spinel ferrites in their applications, because the production and manipulation issues related to nanoparticles are completely avoided, and may offer unprecedented opportunities in the integration of nanostructures bulk spinel ferrites with applications in electronics, spintronic devices, data storage and silicon-based technologies [31]. Fig. 3.16 suggests that it is possible to separate though magnetic way the multiparallel-twinned grains (χ_i = 0.28; α = 3x10^{-6} $A^{-1}m$) from the equiaxed ones (χ_i = 3.6; α = 5x10^{-4} $A^{-1}m$), which present a remarkably different magnetic susceptibility.

The multiple parallel twinning growth of cubic spinel crystals can be an interesting phenomenon worthy of further investigation in view of the joint enhancement of strength and toughness. In fact, it is well known that one of the methods for toughening ceramics is the addition of plate-like particles in order to

dissipate energy by toughening mechanisms like cracks blunting, cracks deflecting, and daughter crack formation. Unfortunately, up to now it had not got success to proof such toughening mechanism in multiparallel-twinned overgrown dense cobalt ferrite. On the contrary, as it can be seen from the Fig. 3.18, it seems that the crack propagation requires more energy when the microstructure is based on small equiaxed grains.

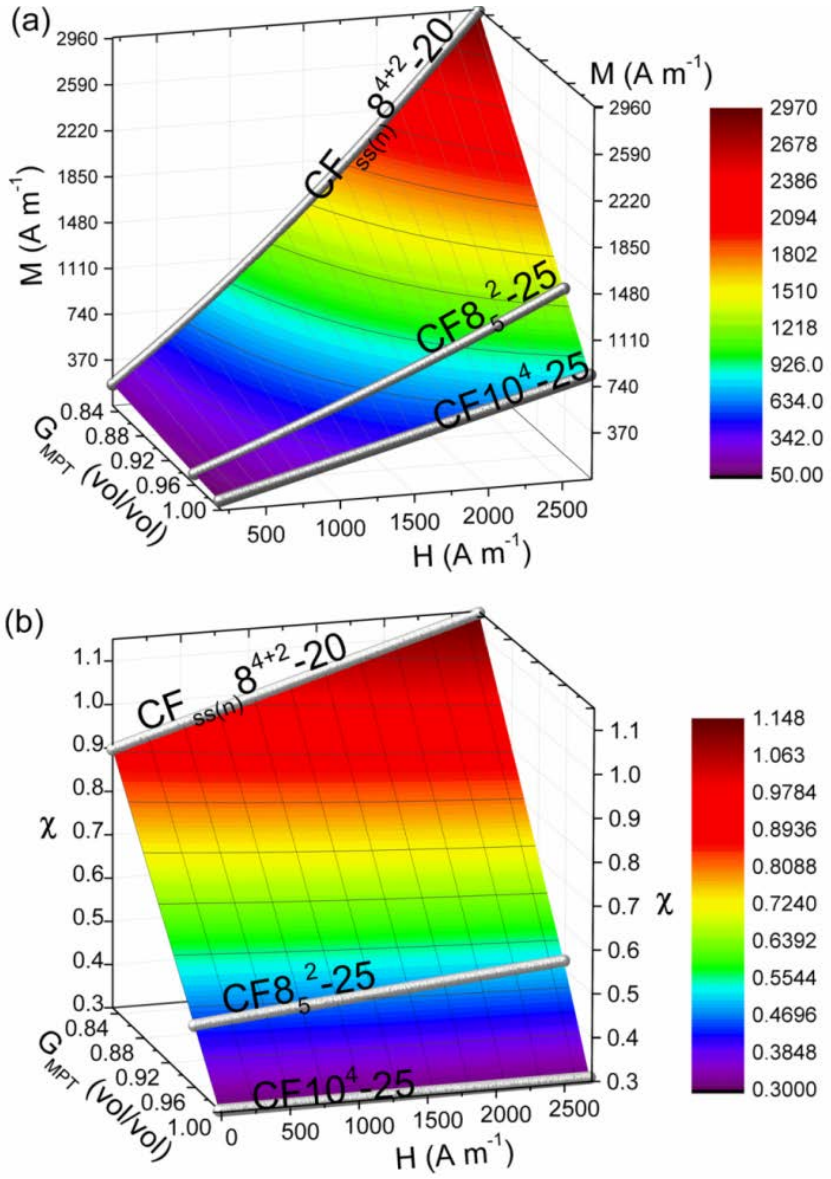

Fig. 3.14 Plot of (a) magnetization ($M = \chi H$) and (b) volume magnetic susceptibility ($\chi = \chi_i + \alpha H$) as a function of magnetic field strength (H), and multiparallel-twinned grains volume fraction (G_{MPT}).

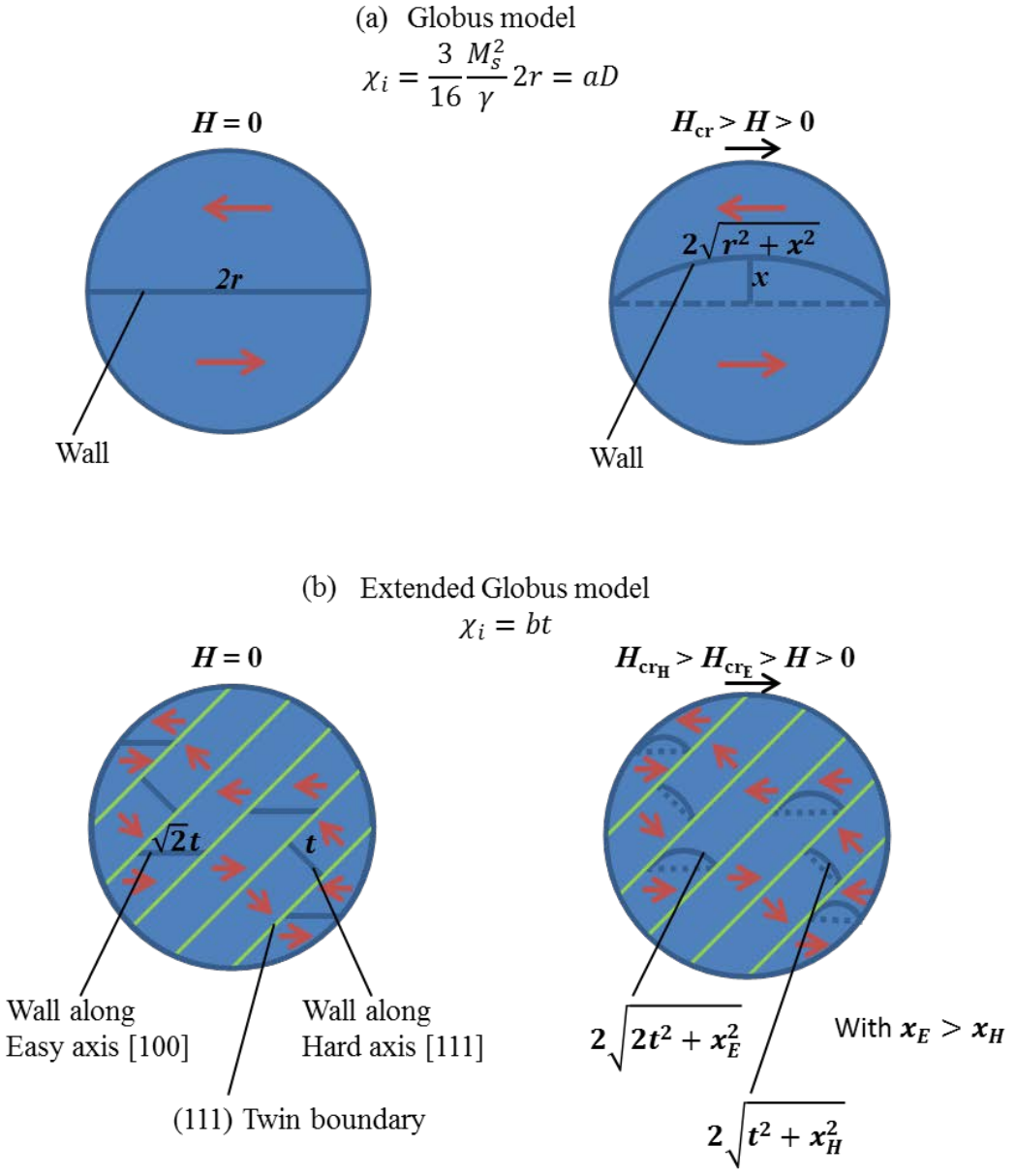

Fig. 3.15 (a) Globus model for the linear variation of the initial susceptibility (χ_i) with the grain size ($D = 2r$) [88]. In the Globus model the proportionality constant, a, is affected by the saturation magnetization (M_s) and the surface energy of the domain wall (γ). (b) In the extension of the Globus model, to the case of multiparallel-twinned grain, χ_i is directly proportional to the distance between the twinning boundaries (t) by the proportionality constant, b, which should take into account the different wall length of domain wall along the easy axes and hard axes together with the different γ values. In the image x refers to the wall bulging, H_{cr} to the field strength at which the wall starts to slip, and the subscript $_E$ and $_H$ label the easy and hard axes, respectively.

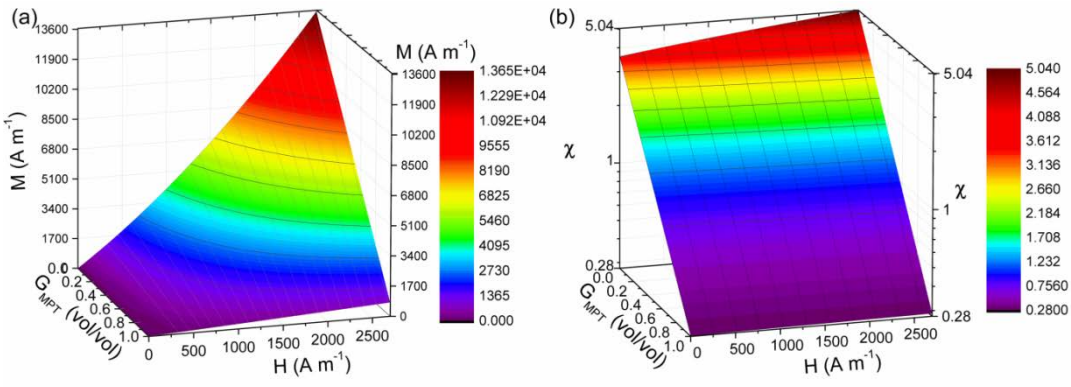

Fig. 3.16 (a) Magnetization and (b) susceptibility trend as a function of magnetic field strength (*H*), and multiparallel-twinned grains volume fraction (G_{MPT}) estimated through the mixing rule.

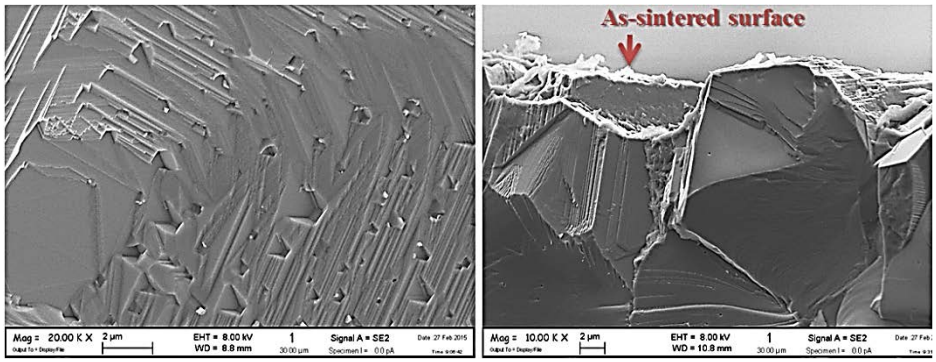

Fig. 3.17 SEM micrograph of fracture surface of cobalt ferrite sintered at 1200 °C for 2 h starting with $CF10_{ss(n)}{}^{4}$-25 powder.

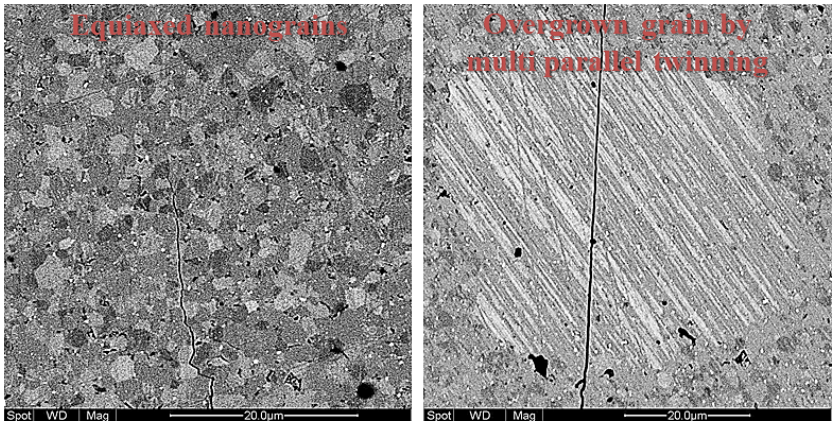

Fig. 3.18 SEM micrograph of polished surface of cobalt ferrite sintered at 1200 °C

3.2 Dielectric materials[2]

3.2.1 TiO_2 powders

Commercial Degussa P25 TiO_2 (P25) was used since it is a largely used commercial titania supplied as nanopowder. The nanopowder is a mixture of anatase and rutile in the ratio about (depending on the batch) 3:1. The existence of two different phases, their unknown precise amount, and the nanometric sized particles may give some problems during the synthesis, shaping and sintering of ceramic materials. In particular, the presence of nanosized particles, and the high density difference between anatase (size: 24.5 nm; bulk density: 3.893 g/cm^3, ICDD-PDF-2 code number 00-021-1272) and rutile (size: 44.1 nm; bulk density: 4.25 g/cm^3 ICDD-PDF-2 code number 00-021-1276), as in the case of this commercial powder, non-negligibly contribute to the chemical potential by changing the activation energy for the phase transformation and the overall volume changing during sintering, respectively [89]. In fact, as demonstrated by the Fig. 3.19, the phase transformation, due to the size distribution of anatase particles and its coarsening during the thermal treatment, occurs in a temperature range of 500-900 °C. The volume change, when the anatase is fully transformed into rutile, is about -7 vol%. In was found that, also by exploiting the anatase-to-rutile transformation in non-equilibrium conditions, *i.e.* high heating rate (300 °C/h), is not possible to get 100% of rutile particles with average crystallite size lower than 83 nm by firing TiO_2 Degussa P25 powders. In any case, it was found that by increasing the anatase-anatase contact-points, *i.e.* by cold consolidation of the powder, it is possible to obtain 100% of nanometre size rutile with reduced dispersity and aggregation of its particles with a mild thermal treatment [89].

[2]The results of this research are reported in the paper:

P. Galizia, G. Maizza, C. Galassi «Heating rate dependence of anatase to rutile transformation» *Process. Appl. Ceram.* 10:4 (2016) 235–241.

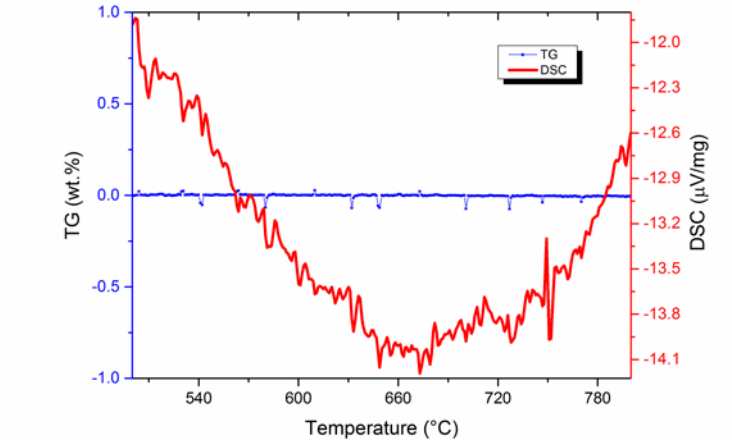

Fig. 3.19 Thermogravimetric (TG) and differential scanning calorimetry (DSC) curves of Degussa P25 titania powder (heating rate 600 °C/h).

3.2.2 TiO_2 bulks

Since titania displays a broad dispersion of its dielectric and electric properties as a consequence of the technological process a previous work was done in order to evaluate its final properties. At room temperature, polycrystalline TiO_2 has ε_r of about 100 [66,90]. Higher values of 200-400 are found by changing the sintering process [90] as a consequence of the variation of lattice defects (*i.e.* titanium and oxygen vacancies) with the different thermal treatment parameters such as soaking time and temperature [91]. Giant dielectric constant was obtained by doping the titania with donor or acceptor ions such as Ta^{5+} or Sr^{2+}. In order to obtain an initial overview on the permittivity range that can be shown by titania, eight different samples were produced at CNR-ISTEC by chancing the starting titania powders and the process parameters. For this purpose, the following starting titania powders were used:

i) Degussa **P25**; which is characterized by the anatase-to-rutile mass ratio of 3:1.
ii) Degussa **P25 cal**cined at 800 °C for 30 min in order to obtain 100 % of rutile.
iii) Huntsman International LLC **T**IO**X**IDE®; which is characterized by 15 wt% of organic compounds and the inorganic powder has the composition shown in Table 3.
iv) Huntsman International LLC **T**IO**X**IDE® **cal**cined at 800 °C for 30 min in order to burnout the organic additives. XRD analysis of as-calcined powder has shown 100% anatase.

Table 3 Chemical analysis of TIOXIDE® supplied by Huntsman International LLC

TiO_2	SiO_2	Al_2O_3	Fe_2O_3	CaO	MgO	K_2O	Na_2O	S
95.6 %	0.27 %	0.09 %	0.1 %	0.03 %	0.06 %	0.01 %	0.04 %	3.8 %

The above four powders were sintered at 1200 °C for **2 h** and **32 h**. The final dielectric properties are shown in Fig. 3.20. Colossal permittivity (ε_r = 10^4-10^5, 1 kHz) is displayed by the sample with the high level of impurities (Fig. 3.20 (b)), while the permettivity spectrum shown by sintered Degussa P25 are closer to the theoretical one. In the following, only Degussa P25 was used for the composites production. In any case the high potentials offered by the huge range of ε_r values confirms the TiO_2- based ceramics as one of the most promising candidates in the field of electronic and energy-storage devices [92].

The abnormal increase of permittivity could be due to the following reasons [90,92,93]: formation of secondary phases or solid solutions; increase of the number of oxygen vacancies with respect to a pure ceramic; formation of defect-dipole clusters; formation of Magnelli phases; effects of grain boundaries and surface effects; increase of conductivity. Another scenario could be that the giant dielectric constant is an artefact, since in most cases the observed behaviour is related to the heterogeneous electrical structure of titania ceramics with more insulating grain boundaries and more conducting grain cores. The grain boundary contribution prevails at low frequency and gives an apparent giant dielectric constant.

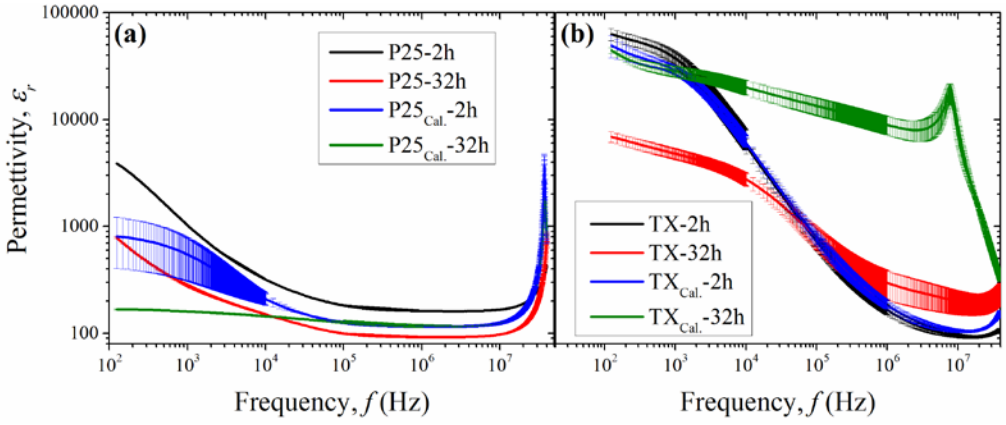

Fi g. 3.20 Dielectric permittivity from 125 Hz to 40 MHz of sintered titania samples.

3.3 Ferroelectric materials

3.3.1 Lead zirconate titanate (PZT) powders

Lead zirconate titanate (PZT) has the perovskite structure (general formula, $(A)[B]O_3$) with (A)-site (Pb^{2+}) occupying the cubo-octahedral interstices described by the [B]-site octahedral sites occupied by Zr^{4+} or Ti^{4+}:

$$(Pb^{2+})\left[Zr_x^{4+}Ti_{(1-x)}^{4+}\right]O_3^{2-} \qquad \text{Eq. 25}$$

At room temperature all compositions are ferroelectric when $x < 0.95$ [94] and display tetragonal ($x < 0.53$) or rhombohedral ($x > 53$) crystal lattice. The boundary between these two phases, called morphotropic phase boundary (MPB), is at $x \sim 0.53$. At this composition PZT displays high electromechanical coupling coefficient and dielectric constant, and finds several applications in piezoelectric sensors, actuators and electromechanical transducers [95]. The high values of piezoelectric coefficient d_{33} (> 330 pC/N) in poled PZT, in proximity of the MPB, stem from the motion of domain walls under the action of applied electric field or stress. This behaviour, termed "soft", can be enhanced by adding donor dopants such as Nb^{5+} on the [B]-site [94] which increases also permittivity, elastic compliance and coupling coefficients of the tetragonal phase [95,96]. Doping PZT with donor ions such as Nb^{5+} results in the creation of (A)-site vacancies in the perovskite lattice, which in turn result in the increasing of the mobility of the domain walls [97]. The structural formula of chosen Nb-doped PZT (PZTN) composition is:

$$\left(Pb_{\left(1-\frac{y}{2}\right)}^{2+}[\,]_{\frac{y}{2}}\right)\left[Zr_{x(1-y)}^{4+}Ti_{(1-x)(1-y)}^{4+}Nb_{(y)}^{5+}\right]O_3^{2-} \qquad \text{Eq. 26}$$

It is worth to notice that the donor doping may stabilize the oxygen vacancies, which induce a large leakage current through the low band offset between the PZT and the electrodes (see paragraph 2.2.6.). For the purposes of the PhD thesis, it was used the remarkable experience acquired in CNR-ISTEC by Galassi *et al.* since 1997 [98] for the synthesis and production of ceramics based on PZTN (x = 0.52, y = 0.024) system as one of the best performing ferroelectric and

piezoelectric materials, displaying high dielectric permittivity (ε_{33}~ 1550) and strong piezoelectric coupling (k_p~ 0.67) [95].

3.3.2 PZT bulks

In order to investigate the thermal activation of the PZT grain growth, a series of PZT compositions was characterized after sintering at 1250 °C for 2 h, and after post thermal annealing at 990°C for 5 min, and 1050 °C for 15 min (Fig. 3.21). It was found that a significant grain growth (60 ±25%) occurs after the thermal treatment at 1000 °C, which abruptly drops down to 7 ±4% with the thermal treatment at 990 °C. This result suggests that post thermal treatment at 1050 °C strongly affect the microstructure of the polished surfaces as it can be seen from the back-scattered electron micrographs (Fig. 3.22).

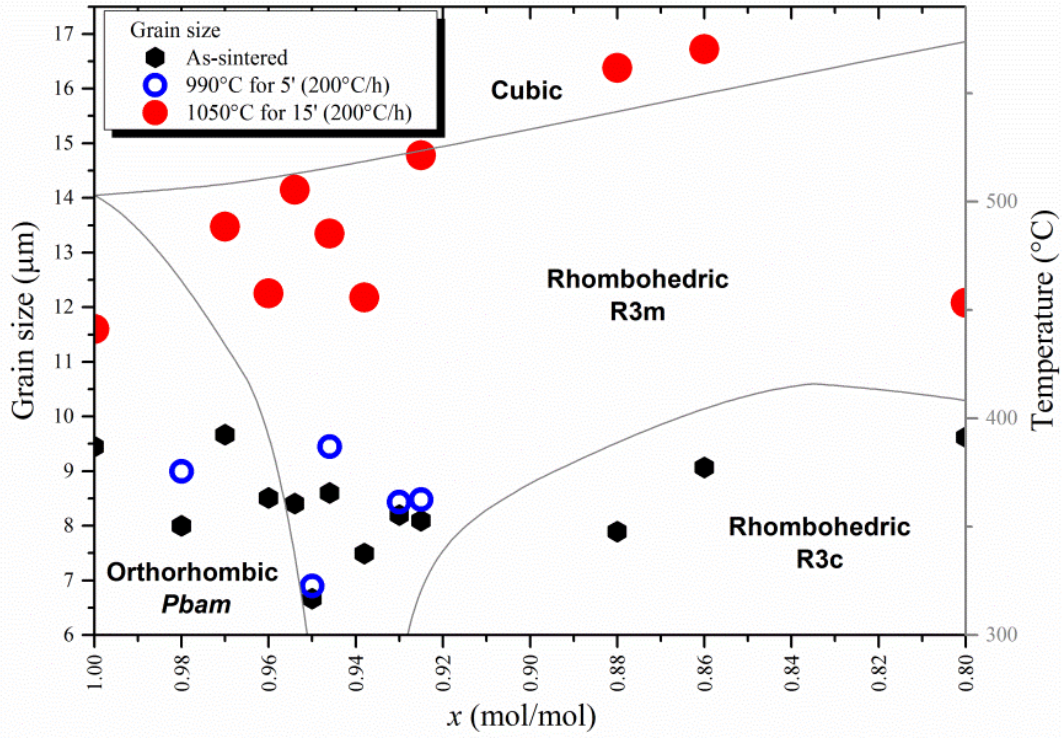

Fig. 3.21 (Left axis) Grain size vs. PZT composition, x, of as-sintered samples (black hexagons), and after heat treatment at 990 °C for 5 min (blue circumferences) and 1050 °C for 15 min (red circles). (Right axis) the corresponding phase diagram (grey lines).

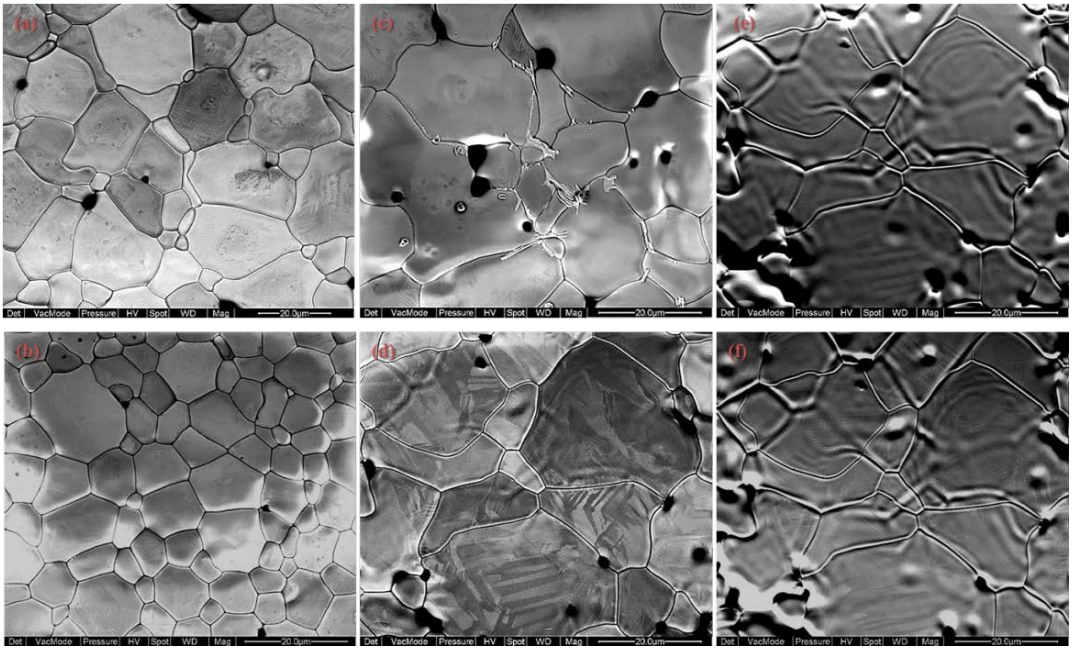

Fig. 3.22 Back-scattered electron micrographs of polished surfaces of PZT samples [(a, b) x = 0.8; (c) x = 0.88; (d-f) x = 1) after thermal annealing at 1050 °C for 15 min. All bars are 20 μm.

3.4 Multifunctional materials

3.4.1 Magnetodielectric composites: CF-TiO_2[3]

The first class of investigated composites were the magnetodielectric one. It was chosen to investigate the production of composites based on $CoFe_2O_4$-TiO_2

[3] The results of this research are reported in the papers:

P. Galizia, C. Baldisserri, C. Galassi «Microstructure development in novel titania-cobalt ferrite ceramic materials» *Ceram. Int.* 42:2 A (2016) 2634-2641.

P. Galizia, D. Gardini, S. Ortelli, C. Capiani, M. Anbinderis, R. Grigalaitis, G. Maizza, C. Galassi «Novel magnetodielectric cobalt ferrite - titania - silica ceramic composites with tunable dielectric properties» *Ceram. Int.* 42 (2016) 16650–16654.

P. Galizia, I. V. Ciuchi, M. Anbinderis, R. Grigalaitis, C. Galassi «Titania-cobalt ferrite ceramic composites for high frequency magnetic applications» IEEE-ICEAA, Turin, 2015.

since many heterostructures are based on spinel ferrites and/or titanium compounds (such as PZT materials), which are selected as starting hub of the material design for a given application. In particular both side materials, and their combination, are used in the catalysis, environmental, and energy fields [45,99]. The composites were produced by starting form $CF_{ss(n)}8^{4+2}$ powder (Table 1) mixed with commercial TiO_2 powder (DegussaP25), according to the compositional scheme:

$$(1-x)TiO_2 + xCoFe_2O_4 \qquad \text{Eq. 27}$$

with x = 0, 0.078, 0.127 , 0.146, 0.185, 0.211, 0.25, 0.313, 0.577 and 1, and sintered at 1200 °C for 2 h. It was found that this system is highly reactive and the displacement reactions, during the reactive sintering at 1200 °C, achieve the equilibrium point according with the following equations [22]:

$$\begin{cases} (1-x)TiO_2 + xCoFe_2O_4 \rightarrow (1-4x)TiO_2 + xFe_2CoTi_3O_{10} \\ (1-x)TiO_2 + xCoFe_2O_4 \rightarrow \left(\frac{4}{3}x - \frac{1}{3}\right)CoFe_2O_4 + \left(\frac{1}{3} - \frac{x}{3}\right)Fe_2CoTi_3O_{10} \\ (1-x)TiO_2 + xCoFe_2O_4 \rightarrow (2x-1)CoFe_2O_4 + (1-x)CoTiO_3 + (1-x)Fe_2O_3 \end{cases}$$

$$\begin{matrix} for\ 0 < x \leq \frac{1}{4} \\ for\ \frac{1}{4} \leq x < \frac{1}{2} \\ for\ \frac{1}{2} < x < 1 \end{matrix} \qquad \text{Eq. 28}$$

The ternary phase diagram, at T = 1200 °C and $p(O_2)$ = 0.21 atm, of the TiO_2-CoO-αFe_2O_3 system can be represented like the one drawn in Fig. 3.23 from our experimental results [22]. The investigated compositions lay on the straight line passing through the TiO_2 and $CoFe_2O_4$ points and the Eq. 28 are represented by the roman numerals, I , II, III, respectively. Thus it is possible to tailor the final microstructure of the *in-situ* composites based on Ti-Fe-Co-O system in order to produce a biphasic dielectric (I), biphasic magnetodielectric (II), or triphasic magnetoelectric materials (III) [22,102]. Once the starting composition is fixed it is quite difficult to depart for the equilibrium amount (Fig. 3.24 (a)). Only, the sintering by SPS at 950 °C for 5 min slightly shifted the reactions (Eq. 28) to the left side.

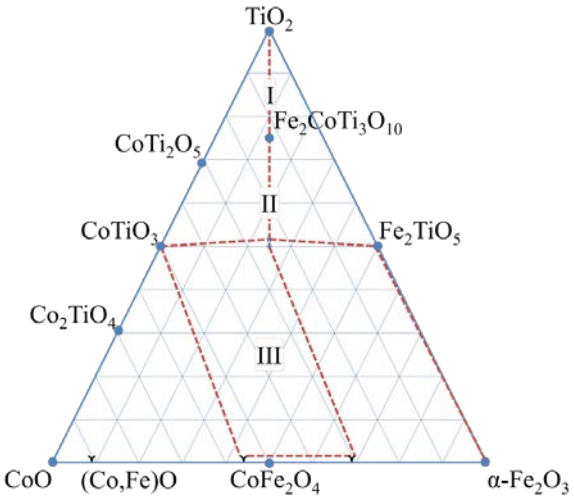

Fig. 3.23 Possible phase diagram of CoO – TiO_2 – α-Fe_2O_3 system at T = 1200 °C and $p(O_2)$ = 0.21 atm. The biphasic system of the triangle sides were drawn by starting from the Co-Ti-O [100], Fe-Ti-O [101], and Co-Fe-O (Fig. 3.1) systems.

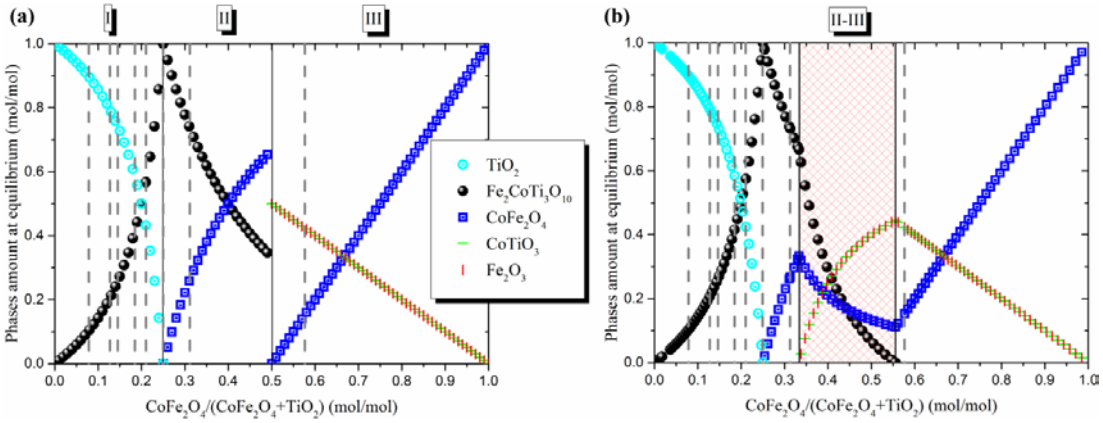

Fig. 3.24 Molar fractions at equilibrium *vs.* $CoFe_2O_4$ content in starting powder mixtures. (a) Phases equilibrium according to Eq. 28 [22]. The vertical solid lines correspond to $TiO_2/CoFe_2O_4$ molar ratio of 3 and 1 respectively and the dashed lines correspond to the investigated compositions [22] which are in agreement with the plotted phases equilibrium. (b) Supposed phases equilibrium in the range of $1/3 < x < 5/9$ according to Eq. 29. The vertical solid lines correspond to $TiO_2/CoFe_2O_4$ molar ratio of 2 and 0.8 respectively and the dashed lines correspond to the investigated compositions [22] which are in agreement with the plotted phases equilibrium.

Since only 8 samples were prepared with x = 0.8, 0.13, 0.15, 0.18, 0.21, 0.25, 0.31, 0.58, the wide region between the dashed lines at x = 0.31 and 0.58 could show a different phase equilibrium with respect that shown in Fig. 3.24 (a). In

fact, the discontinuities between II and III fields are not reasonable. A hypothesis is shown in Fig. 3.24 (b) which corresponds to the following equations:

$$\begin{cases} (1-x)TiO_2 + xCoFe_2O_4 \rightarrow (1-4x)TiO_2 + xFe_2CoTi_3O_{10} \\ (1-x)TiO_2 + xCoFe_2O_4 \rightarrow \left(\frac{4}{3}x - \frac{1}{3}\right)CoFe_2O_4 + \left(\frac{1}{3} - \frac{x}{3}\right)Fe_2CoTi_3O_{10} \\ (1-x)TiO_2 + xCoFe_2O_4 \rightarrow \frac{1}{9}CoFe_2O_4 + \left(\frac{5}{9} - x\right)Fe_2CoTi_3O_{10} + \left(2x - \frac{2}{3}\right)CoTiO_3 + \left(2x - \frac{2}{3}\right)Fe_2O_3 \\ (1-x)TiO_2 + xCoFe_2O_4 \rightarrow (2x-1)CoFe_2O_4 + (1-x)CoTiO_3 + (1-x)Fe_2O_3 \end{cases}$$

$$\begin{cases} for\ 0 < x \leq \frac{1}{4} \\ for\ \frac{1}{4} \leq x < \frac{1}{3} \\ for\ \frac{1}{3} < x < \frac{5}{9} \\ for\ \frac{5}{9} < x < 1 \end{cases} \qquad \text{Eq. 29}$$

Anyway, the existence of 4 coexisting phases in a 3 components (CoO, Fe_2O_3, TiO_2) system corresponds to zero variance. This happens only at a well-defined temperature. This situation should be proved after reaction at 1200°C for long time (in order to ensure that the final composition corresponds to equilibrium) at least in one point in the compositional range 1/3 < x < 5/9 (Eq. 29).

It is worth to notice that it was preferred to use Degussa P25 instead of 100 % rutile (the phase stable at temperature higher than ~700 °C [89]) in order to reduce the volume expansion during the sintering due to the above reactions (Fig. 3.25) and the consequent cracks formation [22].

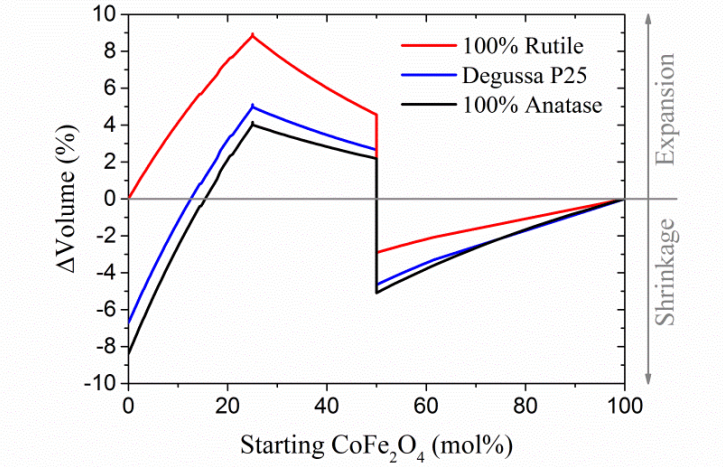

Fig. 3.25 Variations in volume predicted from the chemical reactions (Eq. 28) considering three different type of starting titania powders.

Another critical issue was the uncompleted $CoFe_2O_4$ formation in the $CF_{ss(n)}8^{4+2}$ powder (Table 1), which led to the increasing of porosity in the sintered samples (Fig. 3.26) as a consequence of the $O_{2(g)}$ formation according to Eq. 21 and the following ones [22]:

$$2Co_3O_4 + 6Fe_2O_3 + 18TiO_2 \rightarrow 6Fe_2CoTi_3O_{10} + O_{2_{(g)}} \quad \text{Eq. 30}$$

$$2Co_3O_4 + 6TiO_2 \rightarrow 6CoTiO_3 + O_{2_{(g)}} \quad \text{Eq. 31}$$

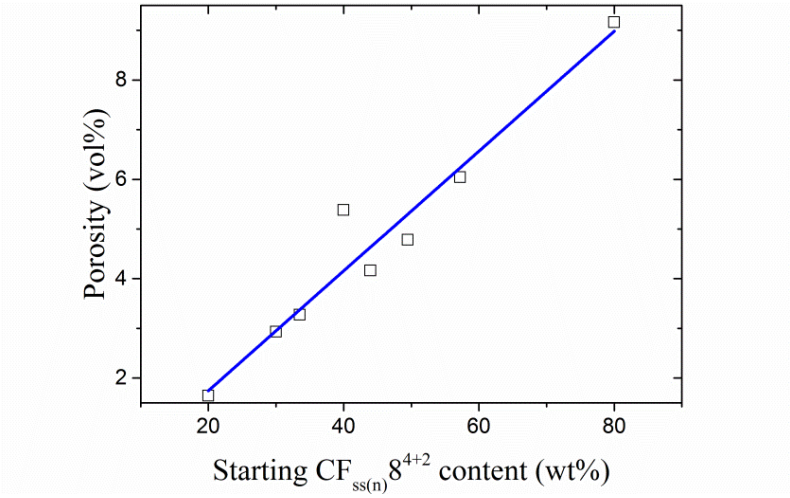

Fig. 3.26 Porosity *vs.* $CF_{ss(n)}8^{4+2}$ content in starting powder mixtures

Since magnetodielectric materials are attracting remarkable efforts for applications in telecommunication field such as miniaturized antenna, antenna radoms, generation of high power microwave pulses, cloaking, perfect lens, screens for electromagnetic compatibility, controllable filters, etc., a small deviation from the main topic (magnetoelectric multiferroic) was done in order to enhance the magnetodielectric properties of those composites and to add a further degree of freedom [103] in the designing amorphous silica was added into $CoFe_2O_4$-TiO_2 system [102]. The silica was chosen because it does not directly influence the magnetic and dielectric properties of the cobalt ferrite due to its smaller dielectric constant (Fig. 3.27) and non-magnetic nature. The addition of silica as dielectric phase not only abruptly reduces the overall dielectric permittivity and dielectric loss but also increases the cobalt ferrite amount in the composites, since no chemical reaction occurs. Therefore the normalized impedance [$Z = (\mu_r/\epsilon_r)^{1/2}$] was increased from 0.16 to 0.33 while keeping a good

miniaturization factor [$n = (\mu_r \epsilon_r)^{1/2}$] of about 4 [102,104]. However, it has been shown that the performance of microstrip antennas is better with magnetodielectric substrates with $\mu_r = \epsilon_r$ that can be obtained using soft ferromagnetic ferrites such as Mn-series spinel ferrites or hexagonal ferrites instead of hard ferromagnetic spinel cobalt ferrite [105].

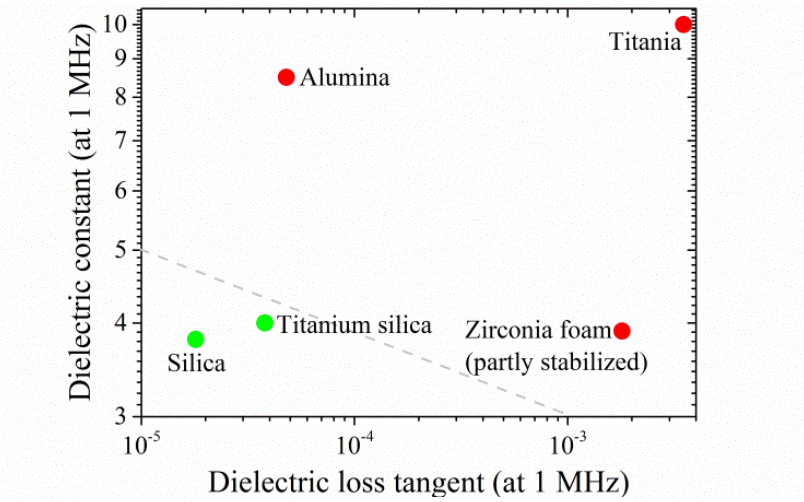

Fig. 3.27 Dielectric constant vs. dielectric loss tangent plot for alumina, silica, titania, and titanium silica (at 1 MHz). The values were taken from CES EduPack™ 2013 software's database.

The chosen of silica instead of titania was taken by considering the Ashby plot (Fig. 3.27). Moreover, in the literature, it is well know that TiO_2 is not suggested to make composite with ferrites for miniaturized antenna, where the impedance matching is needed, because it has a relatively high dielectric permittivity [105]. In fact, up to 1941, when a dielectric constants as high as 1100 were observed for a series of barium oxide-titanium oxide compositions, the rutile, with a dielectric constant of around 10^2 (at room temperature and in the range of 100 Hz to 1 MHz) showed the highest values [66]. The high value of dielectric permittivity should decrease at the temperature increasing, since it was found that high static dielectric constants which increase with decreasing temperature obeying a modified Curie-Weiss law [106]. However, the predicted permittivity value (at maximum) at 600 K is only ~25% less than that at room temperature (Fig. 3.28). Anyway the study of $CoFe_2O_4$-TiO_2 system was important in view of the production of PZT-CF composites. From this study reactivity between CF and titania was evaluated, while the possibility to tailor the final microstructure (Fig. 3.24), in terms of phases amount, in the $CoFe_2O_4$-TiO_2-$CoTiO_3$-Fe_2O_3-$Fe_2CoTi_3O_{10}$-SiO_2 system is quite important for applications in

catalysis and environmental fields [107,108,109] and adds interesting results in the frame of multifunctional materials.

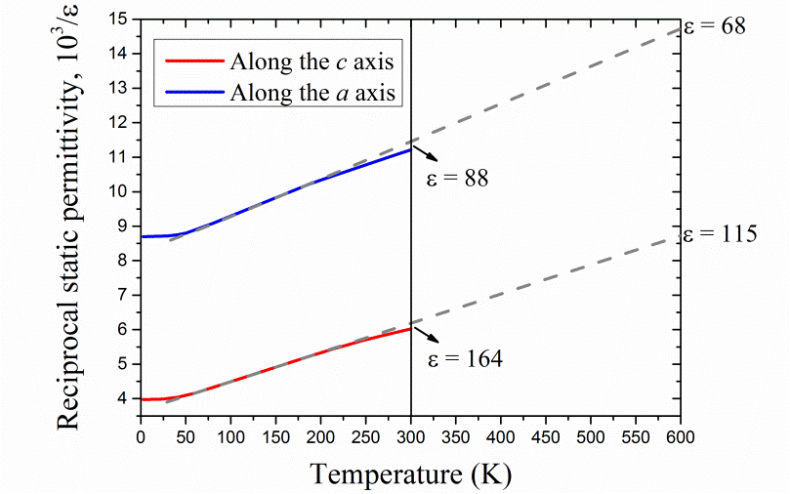

Fig. 3.28 Temperature dependences of the reciprocal static dielectric constants along *a* and *c* axes of TiO_2 rutile. The solid lines were measured by G. A. Samara P. S. Peercy [106]. The dashed lines depict was calculated through the Curie-Weiss law.

3.4.2 Magnetoelectric multiferroic composites[4]

Magnetoelectric composites based on cobalt ferrite (see paragraph 3.1.) and niobium-doped lead zirconate titanate (see paragraph 3.3.) were produced starting from as-calcined PZTN powder of the composition $Pb_{0.988}(Ti_{0.48}Zr_{0.52})_{0.976}Nb_{0.024}O_3$ sieved at 700 nm and adding 0.26, 0.32, 0.58, and 0.81 molar fraction of $CF_{ss(n)}10^4$-25 powder. The cold consolidated (by linear pressing at 100 MPa and isostatic pressing at 300 MPa) disks with ϕ = 10 mm were sintered by conventional sintering at 1200 °C and 1150 °C for 2 h, and by quite fast sintering at 1100 °C for 30 min [19]. After conventional sintering at 1200 °C the sample with higher amount of PZTN were found partially melted, while the others presented low densification (Fig. 3.29). By reducing the sintering temperature down to 1150 °C, the melting was avoided and the densification was

[4] The results of this research are reported in the papers:

P. Galizia, C. E. Ciomaga, L. Mitoseriu, C. Galassi «PZT-cobalt ferrite particulate composites: Densification and lead loss controlled by quite-fast sintering» *J. Eur. Ceram. Soc.* 37 (2017) 161–168.

improved (Fig. 3.30). Full densification was achieved by quite-fast sintering for the samples with low cobalt ferrite amount (Fig. 3.30).

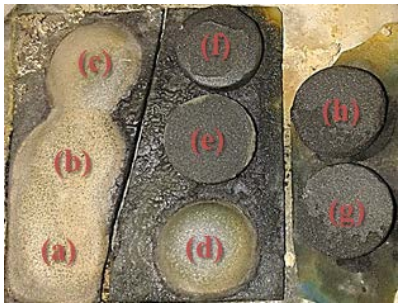

Fig. 3.29 PZTN-CF samples after thermal treatment at 1200 °C for 2 h. The samples labelled with (a, b), (c, d), (e, f), and (g, h) are characterized by cobalt ferrite molar fraction of 0.26, 0.32, 0.58, and 0.81, respectively.

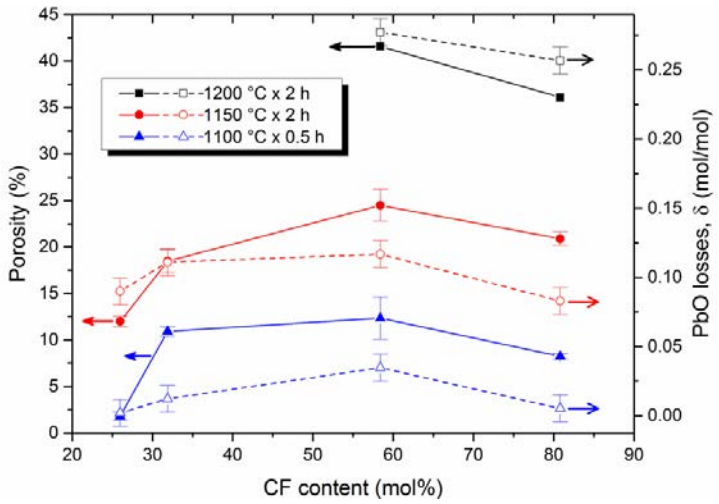

Fig. 3.30 Porosity (solid symbols) and calculated PbO loss (open symbols) vs cobalt ferrite (CF) content in the sintered composites.

The increase of densification at the decreasing of sintering temperature is most probably due to the lead loss from the PZTN phase. In fact, although lead-saturated atmosphere was supplied during the sintering process, PZTN grains can lose PbO to equilibrate the PbO activity in the atmosphere inside the closed porosity (Fig. 3.31). Moreover, even if the donor doping such as Nb^{5+} can stabilize a certain amount of Pb^{2+} vacancies, the PbO loss can cause the precipitation of ZrO_2 and/or TiO_2. The latter can react with cobalt ferrite, according to the Eq. 28, and further promote in turn the lead loss. Thus the quite-fast sintering, owing to its lower sintering temperature and time, can reduce the

amount of PbO loss and reactions. From XRD analysis, in fact, it was found that baddeleyite (ZrO_2) formation and the tetragonality changing of the perovskite phase was suppressed by quite-fast sintering (Fig. 3.32). The formation of the baddeleyite is clearly visible through its highest peak highlighted by the square symbol (Fig. 3.32).

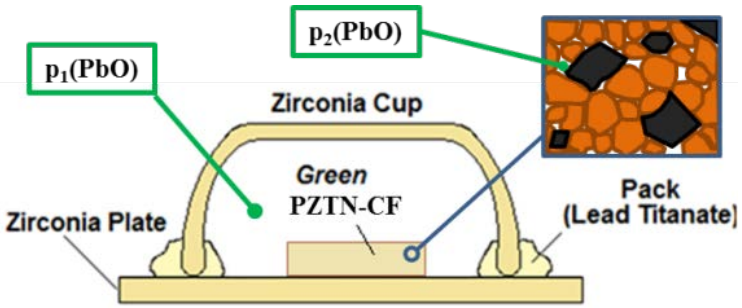

Fig. 3.31 Scheme of a green PZTN-CF sample surrounded by a mixture of PbO and $PbTiO_3$ powders (also called atmosphere powder or pack), called pack, in order to provide a positive vapour pressure in a closed zirconia cup and contain the lead loss. However, inside the porosity of the sample lead activity, $p_2(PbO)$, is different from that outside the sample, $p_1(PbO)$. In the "zoom of microstructure" the orange grains and the black ones represent the PZTN and CF, respectively.

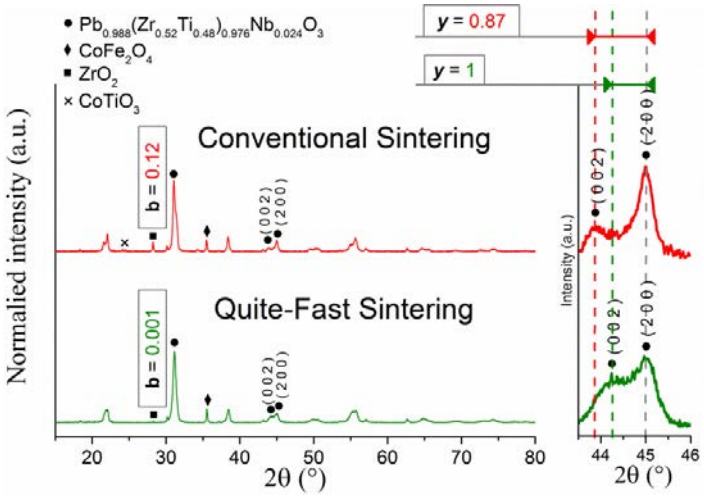

Fig. 3.32 XRD patterns of sintered PZTN-CF (x = 26) composites.

In Fig. 3.32, it can be seen that the weight percentage of the baddeleyite decreases from ~12% to ~0%, and a strong increase of tetragonality is visible in the sample sintered through the conventional way. The changing of the tetragonality is correlated to the distance between d-spacing of the (002) and (200)

diffraction peaks. In fact, according to the crystal geometry equations, which correlate the d-spacing with the Miller indices, for the tetragonal symmetry the d-spacing of the (002) diffraction peak is directly proportional to the *c* lattice parameter ($2d_{(002)} = c$) while the d-spacing of the (200) diffraction peak is directly proportional to the *a* lattice parameter ($2d_{(200)} = a$). Since, the (002) diffraction peak widens towards smaller 2θ degrees with increasing sintering temperature, whereas the *a*-axis dimension is not strongly affected, the crystal tetragonality, *c*/*a*, of the PZTN phase increases vs. increasing sintering temperature, owing to the formation of perovskite phases with lower Zr/Ti ratio. The above discussion about the PbO loss, the reactions between the perovskite and spinel phases, and the XRD evidences are taken into account by the following reactions:

$$Pb_{0.988}(Zr_{0.52}Ti_{0.48})_{0.976}Nb_{0.024}O_3 \rightarrow$$
$$\rightarrow 0.988fPbO_{(g)} + 0.012fNb_2O_5 +$$
$$+\sum_{i=1}^{n} w_i\big(0.50752(1-y_i+fy_i)\big)ZrO_2 + \sum_{i=1}^{n} w_i\big(0.46848(1-z_i+fz_i)\big)TiO_2 + \quad \text{Eq. 32}$$
$$+(1-f)\sum_{i=1}^{n} w_i Pb_{0.988}(Zr_{0.52y_i}Ti_{0.48z_i})_{0.976}Nb_{0.024}O_3$$

$$TiO_2 + CoFe_2O_4 \rightarrow CoTiO_3 + Fe_2O_3 \quad \text{Eq. 33}$$

where *f* is a molar fraction representing the amount of PbO loss; *y* and *z* are molar fractions that define the Zr/Ti molar ratio into the produced PZTN perovskite phases (characterized by an increased tetragonality). The amount of PbO loss, *f*, can be calculated from the Zr/Ti ratio variation ($0.52y/(0.48)z = 0.52y/(1-0.52y)$) and the amount of one of the products. As said above, the (002) diffraction peak's broadening toward smaller 2θ is the result of a convolution of "*n*" diffraction peaks where each of these reflects the presence of a specific amount, w_i, of perovskite phase characterised by a specific lattice elongation along the tetragonal *c*-axis which increased as the Zr/Ti ratio is decreased. This feature justifies the use of the operators summation in the above reaction in order to keep in consideration the whole range of the appeared perovskite solid solutions. For the choice of the reference product, it is convenient to consider the baddeleyite formation instead of the other products since the $ZrO_2/CoTiO_3$ molar ratio, expressed as $(0.50752\cdot(1-y+fy)) / (0.46848\cdot(1-z+fz))$, is always bigger than one when *f* is bigger than $(z-1)/z$. In particular the $lim_{f\rightarrow\frac{z-1}{z}^{+}} \frac{1-y+fy}{1-z+fz} = +\infty$, while

the ratio (1-*y*+*fy*)/(1-*z*+*fz*), when f = 1 (PbO completely depleted), is always defined by the starting Zr/Ti molar ratio which is bigger than one. It means that the amount of $CoTiO_3$ and Fe_2O_3 are negligible when PbO losses are low and matches the XRD evidence in terms of relative intensities of detected ZrO_2 peaks which are higher than those of $CoTiO_3$ phase, and the produced tetragonal phases with lower Zr/Ti molar ratio (Fig. 3.32). Even if the $CoTiO_3$ diffractions peaks are very low and, for some samples, are hidden by the noise, its formation is expected since the $TiO_2/CoFe_2O_4$ molar ratio should be lower than 0.8 [22], Fig. 3.24. Niobium oxide's stoichiometric coefficient (0.012*f*) is one order of magnitude smaller than the other phases and thus it is rather invisible to the XRD analysis. In fact, no evidence about the Nb behaviour was found by qualitative XRD analysis and thus its amount was considered constant in the PZTN. Once the baddeleyite molar fraction (*b*) and the change of the amount of Zr in each of *n* produced perovskite (y_i) have been quantified by quantitative XRD analysis, the PbO loss (δ),expressed as molar fraction, was calculated through the following equation:

$$\delta = m_{Pb} \sum_{i=1}^{n} \frac{\left(\frac{b}{m_{Zr}} - 1 + y_i\right)}{y_i} \qquad \text{Eq. 34}$$

where m_{Pb} and m_{Zr} are the stoichiometric coefficients of lead and zirconium in the starting perovskite phase, respectively. In our case, m_{Pb} = 0.988 and m_{Zr} = 0.52 * 0.976 = 0.50752. In order to simplify the Eq. 33, it could be convenient to assume that, besides the starting perovskite phase, characterized by a Zr/Ti ratio of 52/48, there is only another one with a Zr/Ti ratio of 52*y*/48*z* that should be chosen in order to get the lowest goodness of fit (χ^2) during the Rietveld refinement. In this way, *n* = 1 and, consequently, also w_1 = 1, thus the Eq. 31 and the Eq. 33 become, respectively:

$$\begin{gathered} Pb_{0.988}(Zr_{0.52}Ti_{0.48})_{0.976}Nb_{0.024}O_3 \rightarrow \\ \rightarrow 0.988fPbO_{(g)} + 0.012fNb_2O_5 + \\ +\big(0.50752(1-y+fy)\big)ZrO_2 + \big(0.46848(1-z+fz)\big)TiO_2 + \\ +(1-f)Pb_{0.988}(Zr_{0.52y}Ti_{0.48z})_{0.976}Nb_{0.024}O_3 \end{gathered} \qquad \text{Eq. 35}$$

$$\delta = m_{Pb} \frac{\left(\frac{b}{m_{Zr}} - 1 + y\right)}{y} \qquad \text{Eq. 36}$$

The equation that allows the calculation of the PbO loss from the XRD was obtained by considering that 0.988*f* mole of PbO should correspond to m_{Zr}(1-*y*+*fy*) mole of baddeleyite. Since, the latter can be calculated from the quantitative XRD analysis (*b*):

$$m_{Zr}(1-y+fy)=b \Rightarrow f=\frac{\frac{b}{m_{Zr}}-1+y}{y}=\frac{\delta}{m_{Pb}} \qquad \text{Eq. 37}$$

It can be seen that the calculated PbO loss is in agreement with the porosity calculated by the Archimedes' method (Fig. 3.30). In fact, a proportional correlation between the porosity and the PbO loss is seen in Fig. 3.30. At a given sintering temperature, the maximum values of PbO loss and porosity are seen for the samples with 0.58 molar fraction of cobalt ferrite. These results can be explained considering that the extent of lead loss (and thus that of porosity formation) is proportional, on one hand to the amount of PZTN (which is the source of PbO) and, on the other hand, is correlated to the molar fraction *x* of CF, which reacts with TiO_2 according to the Eq. 32. It is therefore reasonable that porosity and PbO curves display the maximum on the *x* axis, with the highest relative density value (about 99%) corresponding to the lowest PbO loss (0.2%) [19]. Although, quite-fast sintering strongly reduces the PbO loss, it is not enough to achieve the proper microstructure development. The PZTN grain growth is proportional to the sintering temperature and, contrary to the cobalt ferrite grains, does not depend strongly on the composition [19]. The mean size of the PZTN grains (Fig. 3.34), in the samples densified by conventional sintering, are comparable to those of pure PZTN samples sintered at the same temperatures (about 1-2 μm). Quite-fast sintering leads to a substantial reduction in the mean grain size from 1.44 μm to 146 nm. It is well known that, in niobium-doped PZT system, grain refinement below 0.8 μm marks the beginning of a drastic reduction of piezoelectric and dielectric properties [110] as a result of the electric contribution that arrives from the boundaries of ferroelectric grains [111]. The PbO loss was calculated through XRD analysis (Eq. 35) considering the amount of ZrO_2 and variation of perovskite's tetragonality. The as calculated PbO loss, reported in Fig. 3.33, shows an increase of PbO loss *vs.* decreasing relative densities ($\rho_{\%}$) of 0.74PZTN+0.26CF (triangle, $\rho_{\%}$ = 99.1 ±0.8 %), 0.87PZTN+0.13CF (circle, $\rho_{\%}$ = 99.7 ±0.1 %), and PZTN-CF composites shown in Ref. [19] (squares). The δ values of both samples are in agreement with the data

dispersion found for the PZTN-CF composites produced both conventional sintering and quite-fast sintering without the milling treatment for the mixing [19]. Anyway, the higher PbO loss in spite of the higher achieved relative densities can be ascribed to the milling step performed on the PZTN-cobalt ferrite powders mixture as result of the higher PZTN/cobalt ferrite interface surface density due to the decreased particles size and increased CF particles dispersion.

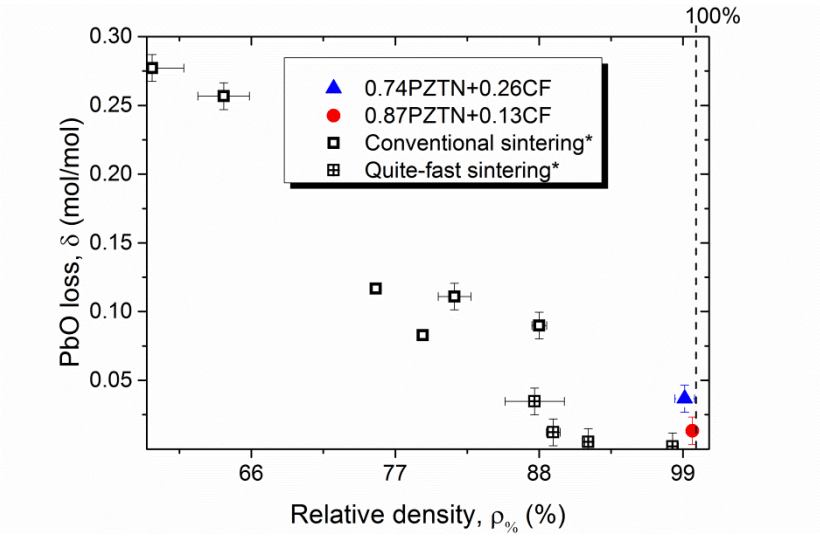

Fig. 3.33 PbO loss of 0.74PZTN-0.26CF (triangle), 0.87PZTN+0.13CF (circle), and PZTN+CF composites reported in (*) Ref. [19] (square symbols) *vs*. their relative density.

The low permittivity of the "electric" boundaries of the ferroelectric phase can make more difficult or outright the electrical poling of particulate composites, even if the percolation of ferromagnetic phase did not occur. The electric permittivity, influenced by the combination of intrinsic size effects of the ferroelectric phase, the "dilution" effect due to the nonferroelectric grain boundaries, the ferromagnetic phase, and the porosity [112], cannot be high enough to reach the saturation polarization of the ferroelectric phase in particulate ME composites (Fig. 3.35). Fig. 3.35 shows the polarization *vs.* applied electric field of samples with 0.26 molar fraction of cobalt ferrite before the electrical breakdown at room temperature (Fig. 3.35 (a)) and 120 °C (Fig. 3.35 (b)). This result suggests that, even if there is no evidence of ferroelectric behaviour, it can be convenient to optimize poling temperature in order to achieve the saturation polarization under the highest electric field below the electrical breakdown limit. Anyway, a post thermal treatment (annealing), below 900 °C, should promote the

growth of the PZTN nanograins, as discussed above in the paragraph 3.3., and improve the polarizability of such composites by decreasing the leakage currents.

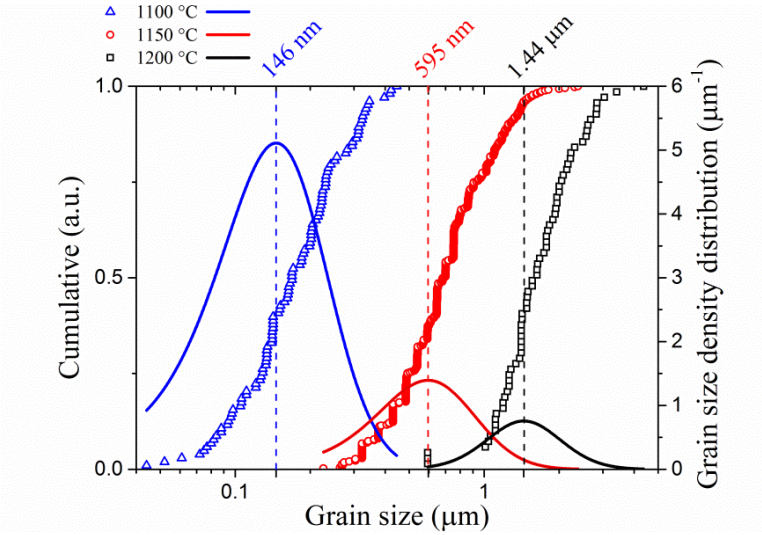

Fig. 3.34 The triangular, circular, and square symbols are the experimental measured PZTN grains of the sintered samples at 1100 °C, 1150 °C, and 1200 °C, respectively. The corresponding grain size distributions were obtained by deriving the fitting of the experimental points. The sigmoidal curves were fitted through the SGompertz model implemented in OringPro 9.1 software: $y = e^{-e^{-k(x-x_C)}}$.

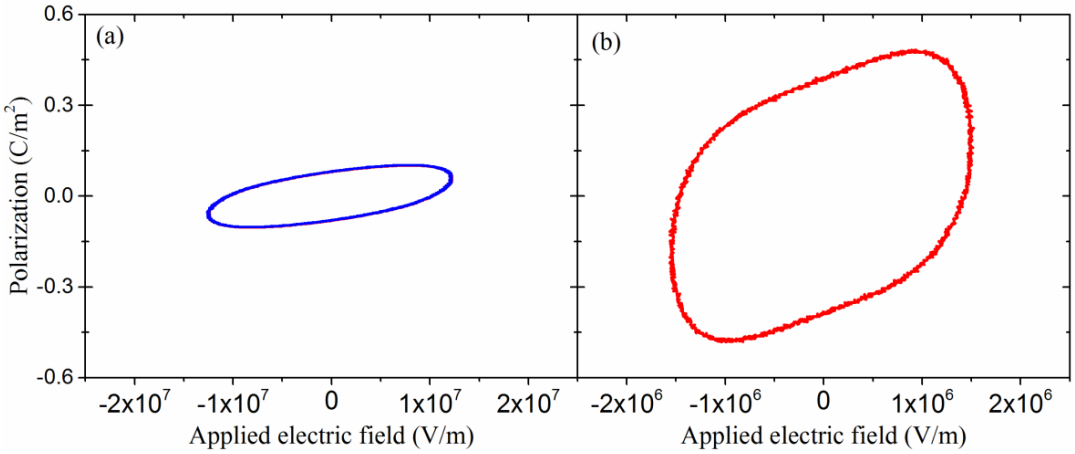

Fig. 3.35 *P*(*E*) loops at 1 Hz and before electrical breakdown of 0.74PZTN+0.26CF samples. The *P*(*E*) loop (a) and (b) was taken at room temperature and 120 °C, respectively.

Regarding the cobalt ferrite phase, it was found that the ferromagnetic hysteresis are in agreement with the literature. In particular, it was found that corcivity H_c values (Fig. 3.36) are within the range reported in the literature for bulk cobalt ferrite [36,113], and follow the inverse proportionality correlation to the grain size of cobalt ferrite (Fig. 3.36) as is expected from the theory [114]. This evidence suggests a multidomain or pseudo-single domain magnetic behaviour [19]. In fact, it is known that coercivity of cobalt ferrite increases with decreasing particle size (multidomain range), gets to a maximum when the grain size is 28 nm [115], and then decreases to zero (single domain range) [116] when superparamagnetism appears for extremely small nanoparticles (superparamagnetic range). For larger grain size (> 28 nm), coercivity decreases as the grain subdivides into domains (Fig. 3.3). The slight increase of H_c for the higher values of d_{CF} (samples sintered at 1200◦C), shown in the inset graph in Fig. 3.36, could not invalidate the trend of inverse proportionality between H_c and d_{CF}, since it should be due to the increase of overgrown cobalt ferrite grain population (G_{MPT}) which decreases the magnetic susceptibility according with the extended Globus model (Fig. 2.15 and Fig. 2.16). As said above (see paragraphs 3.1. and 3.1.2.) multiparallel-twinned grains display lower susceptibility, and thus an enhanced hard magnetic behaviour [31]. The samples sintered at 1100◦C show hard magnetic behaviour with a coercivity of 413–789 Oe and a remnant/saturation magnetization ratio of 0.244–0.382. These values are comparable with pure nanocrystalline cobalt ferrite characterized by a partially inverted spinel structure [117]. The very high coercivity values reported in Fig. 3.3 are due to the high level of strain present in the milled nanopowder (Table 2). In particular the samples 0.19PZTN+0.81CF and 0.74PZTN+0.26CF sintered at 1100 °C show H_c and M_r/M_s magnetic parameters comparable with nanocrystalline cobalt ferrite characterized by crystallite size of 35 nm and 53 nm, and a degree of inversion of 0.80 and 0.82, respectively [118]. The hard magnetic behaviour and the full densification support the view that a high value of the magnetoelectric coefficient, α^{33}_{E}, should be expected. In fact it is found in the literature [21] that for a similar composition α^{33}_{E} increases from 0.73 $mVcm^{-1}Oe^{-1}$ to 1.56 $mVcm^{-1}Oe^{-1}$ upon increase of the relative density from 92% to 97%. Since an almost fully dense material was produced, the α^{33}_{E} coefficient at room temperature should be higher than 1.56 $mVcm^{-1}Oe^{-1}$ due to better mechanical coupling. Moreover, the magnetostriction (λ) of nanocrystalline cobalt ferrite and its sensitivity to applied magnetic field ($d\lambda/dH$) should by higher than that of bulk

cobalt ferrite [118,119]. This characteristic makes the particulate composites suitable for magneto-elastic stress sensor application.

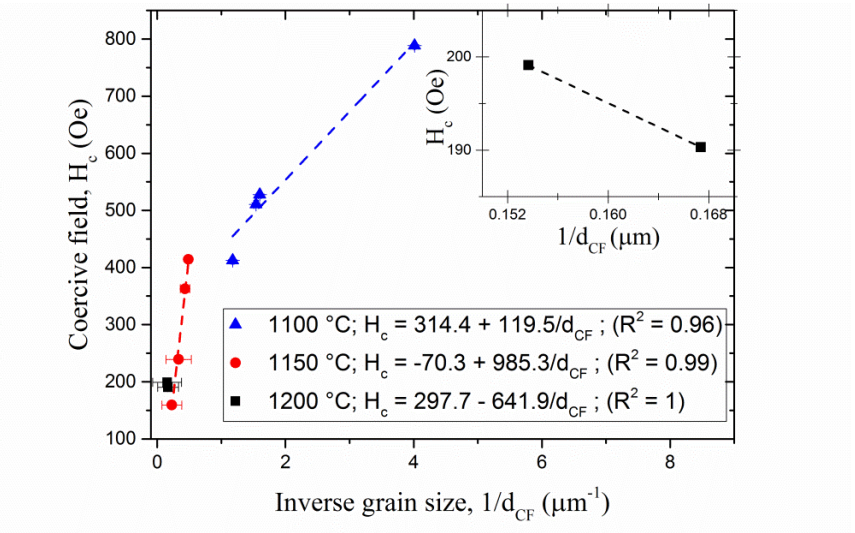

Fig. 3.36 Variation of coercive field with inverse grain size

According with Eq. 19, λ can be enhanced by increasing the uniaxial anisotropy (the stress anisotropy can be one component) which in turn can be correlated to crystallite size and strain according to Eq. 20. In order to achieve this goal a further milling treatment was designed. The milling of powders mixture aims increasing the sinterability of the sieved (at 700 nm) as-calcined PZTN powder and $CF_{ss(n)}10^4$-25 powder, and better exploits the quite fast sintering. This variation in the process produces a "*dual-particulate ceramic composite*" where the cobalt ferrite grains are dispersed in a fully dense PZT matrix with a bi-modal distribution peaked at 150 nm and 8 μm (dual-particulate), resulting in a hierarchical structure with "*wasp-waisted*" character (Fig. 3.37 (a)). Through the study of the cobalt ferrite grain morphologies it can be seen that the milling treatment boosts the growth rate of cobalt ferrite {111} faces respect to {100} ones, and leads to the development of nanograins with octahedral shape. On the other hand, the aggregated cobalt ferrite particles grow by multiple parallel twinning of the undispersed cobalt ferrite particles which can extend up to 8 μm enclosing also the PZTN particles (Fig. 3.37 (b)). The microstructures of the PZTN-CF composites can be considered as dual-particulate composite since the dispersed phase, after sintering, results in two different phases in terms of grain size and morphology. This novel structural scheme can offer a "wasp-waisted" character [120]. In fact, it is well known that cobalt ferrite displays a strongly

different magnetic behaviour in function of its grain size [19,121,122], morphology and lattice defects [31,123]. In particular since the micronic cobalt ferrite grains should display much easy movement of the domain walls respect to the cobalt ferrite nanograins, which are characterized by very-higher coercivity, an additional ferromagnetic resonance and thus further magnetoacoustic resonances are expected [5,16]. Anyway, the hierarchical CF dispersion is highly innovative and suggests that it is possible to produce dual-particulate composites with a wider magnetic response.

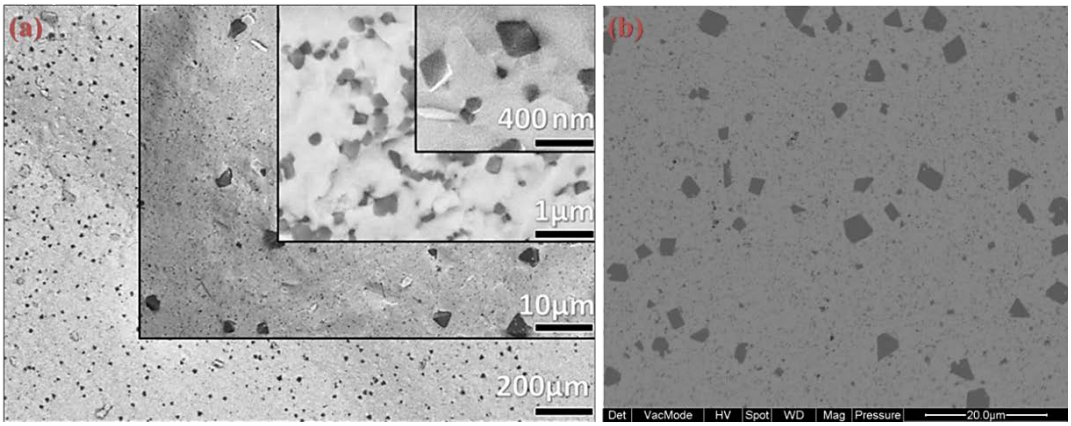

Fig. 3.37 (a) Back-scattered SEM images, at different magnifications, of fracture surfaces of sintered 0.87PZTN+0.13CF sample with bimodal size distribution of magnertic phase. (b) Its polished surface.

3.4.3 Magnetoelectric layered composites[5]

PZTN-cobalt ferrite multiferroic bilayers were produced by EPD on Ag-coated alumina. The processing consisted in a first electrophoretic deposition on silver-coated alumina substrates of $CoFe_2O_4$ dispersed in an ethanol suspension followed by a first thermal consolidation. Then, a second EPD on the formed layer from an ethanol-based PZTN suspension was performed followed by a final sintering [124]. The first deposition of CF particles from ethanol-based

[5] The results of this research are reported in the paper:

P. Galizia, I. V. Ciuchi, D. Gardini, C. Baldisserri, C. Galassi «Bilayer thick structures based on $CoFe_2O_4/TiO_2$ composite and niobium-doped PZT obtained by electrophoretic deposition» *J. Eur. Ceram. Soc.* 36 (2016) 373-380.

suspension created a layer 20 μm thick (Fig. 3.38). After heat treatment at 500°C, the deposited cobalt ferrite layer was homogeneously cracked in “islands” wetted by the silver diffused from the electrode [124]. The subsequent EPD of PZTN showed a typical deposition trend characterized by a current density steadily decreasing and resulted in a sintered layer (at 900 °C) of about 75 μm thickness (Fig. 3.38). No evidence of new phase formation among the deposited cobalt ferrite and PZTN phases during the heat treatments was observed. The dielectric permittivity (ε_r) and the loss tangent (tanδ) of the bilayer structure *vs.* frequency are shown in Fig. 3.39 (a). At the frequency of 1 MHz, ε_r and tanδ values change of -69% and +4%, respectively, by adding the cobalt ferrite layer with respect to the PZTN monolayer obtained with the same procedure. There is a lack in literature regarding the dielectric properties of PZTN thick layers, but anyway, ε_r values are one order of magnitude higher to those obtained for PZTN thin layers prepared by the oxide precursor method [125]. Higher losses at lower frequencies can be related to extrinsic conductivity. The remnant polarization P_r and the coercive field E_c change of -75% and +1%, respectively, by adding the cobalt ferrite layer (Fig. 3.39 (b)). The lacked full saturation is probably associated with conductivity effects caused by the presence of the spinel magnetic phase. The interface between the electrode and the PZTN layer and the space charges (e.g., oxygen vacancies at the interfaces between electrodes and layers) may also affect the measured values of the ferroelectric parameters. The piezoelectric properties were confirmed through the d_{33} piezoelectric constant (Fig. 3.40). It should be noted that such a value (50 pC/N) is only indicative of piezoelectric response as this method is not appropriate for layer characterization (Fig. 2.30). Though a value of the d_{33} coefficient in the range of several tens of pC/N provides unequivocal evidence of useful piezoelectric activity, in the present case such a low value could be due to the clamping to the substrate that constrains the lateral expansion of PZTN layer [73,74]. The ferromagnetic properties (Fig. 3.39 (c)) are reasonable values for that structure, since 250 Oe of coercivity well matches the expected value for micrometric cobalt ferrite grains (Fig. 3.36) and the magnetization reflects the low cobalt ferrite weight fraction. The large grain size and the low coercivity should improve the joule magnetostriction caused by the unimpeded domain wall motion and domain rotation [13]. The produced bilayers are reasonably well-structured and display unequivocal evidence of ferroelectric and ferromagnetic orders. Moreover, such bilayers show good repeatability and reliability giving the concrete possibility to be exploited in the production of many electronic devices, once the magnetoelectric coupling between the magnetic and piezoelectric phases will be optimized.

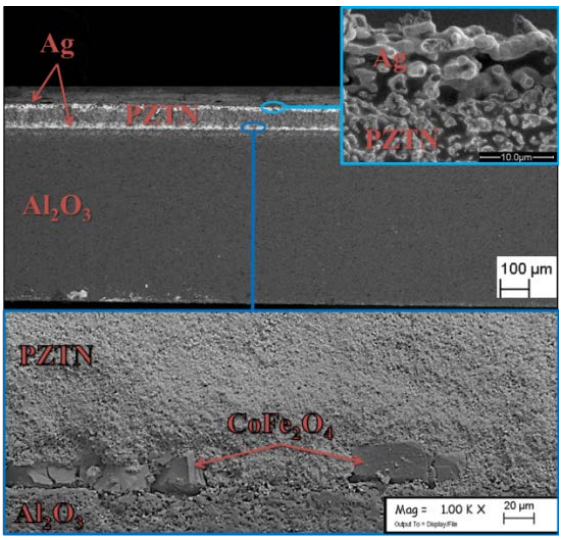

Fig. 3.38 Backscattered electron micrograph of fracture surface of magnetoelectric layered composite. All the insets are secondary electron micrograph.

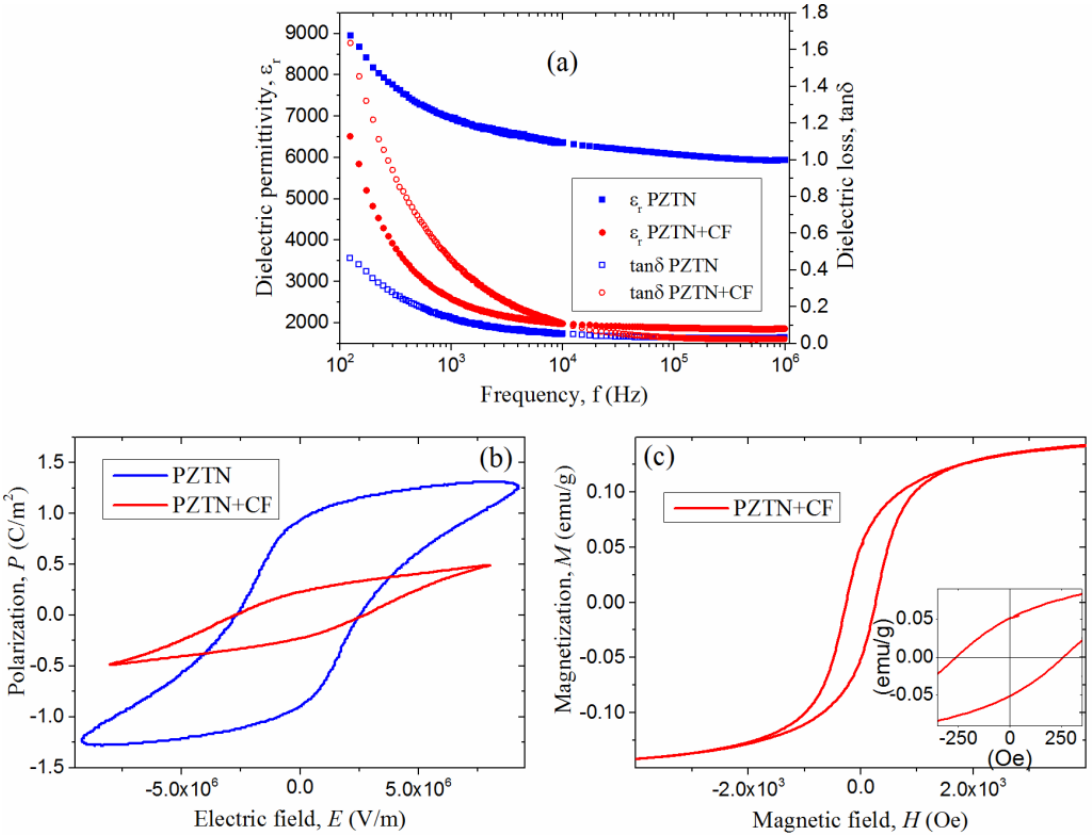

Fig. 3.39 (a) Dielectric permittivity (ε_r) and loss tangent (tanδ) for the PZTN-cobalt ferrite bilayer *vs.* frequency. (b) and (c) electric and magnetic hysteresis loops, respectively, taken at room temperature.

Fig. 3.40 The device is formed by top silver electrode, PZTN layer, cobalt ferrite layer, bottom silver layer, alumina substrate, brass foil electrically contacted to the bottom silver layer.

Chapter 4

Conclusions

Magnetoelectric multiferroic composites were produced as, in form of particulate and layered structure by quite-fast sintering and electrophoretic deposition, respectively. Particulate PZT-CF composites with CF content lower than 26 mol% display full density, homogeneous microstructure, and homogeneous distribution of ferroelectric phase, and are characterized by an overall hard magnetic behaviour. Since there was not a perfect dispersion of cobalt ferrite nanoparticles (probably due the stronger collective interaction of single domain magnetic particles), the cobalt ferrite grains size populations have a bi-modal distribution peaked at about 10^2 nm and 10^4 nm ("*dual-particulate*") resulting in a hierarchical structure with expected "wasp-waisted" character. The ferroelectric phase was partially poled by applying 1.5 kV/mm at 120 °C. A further increase of the applied electric field led to the electric breakdown. This phenomenon could be due to the dead-layer of the nanograins of PZT rather than cobalt ferrite leakage currents. An annealing treatment at 950 °C can promote the PZT grain growth and improve the ferroelectric properties of the PZT-CF composites produced by quite fast sintering. The layered PZT-CF composites, although not achieving the full densification, were poled up to the saturation owing to the "full dielectric" configuration. The layered composites show a softer magnetic behaviour respect to the particulate composites. This is mainly due to the larger cobalt ferrite grain size that was permitted in the layered structure since the CF particles were not dispersed. Both the produced microstructures are highly innovative and peculiar at the state of art in magnetoelectric multiferroic composites. These results were achieved through the development of the quite-fast sintering and the optimization of the milling treatment. For the "quality control" of the thermal treatment it was developed an equation that allows the PbO loss to be calculated through XRD analysis (Eq. 36). This equation can be extended to all the lead zirconate titanate compounds or adapted to others compound with volatile elements. The milling efficiency was investigated through the crystallite size and strain level calculated by Rietveld refinement. An indicative value of the milling efficiency was also elaborated and used starting from particle size distribution curves (Eq. 5). The study of the single compounds led to "secondary" important results. From the study of the milling efficiency on the CF particles it was found an empirical law that correlates the spin-canting-

angle white the crystallite size and strain level (Eq. 20). The study of the different microstructure evolution as function of the physical state of the CF powders led to the understanding of a peculiar grain growth mechanism of the CF that was called “multi parallel twinning overgrowth”. Moreover through the comparison of the different bulk CF microstructure, in terms of amount of multiparallel-twinned grains, an extension of the Globus model was proposed (it is summarized in Fig. 3.15 and Eq. 23). From the study of the thermal treatment effect on the titania powders, kinetic considerations on the anatase-to-rutile transformation under non-equilibrium conditions were published (Ref. [89]), while the giant dielectric constants of bulk titania are still under study and will be published soon. The study of the CF-titania system, which gives an important contribution to the production of the PZT-CF composites and in particular on the chemical reactions that can occur in such composites, led to the production of magnetodielectric composites by reactive sintering of cobalt ferrite and titania mixture and to the draft of a pseudo phase diagram of $TiO_2 – CoFe_2O_4 – O_2$, (at $p(O_2) = 0.21$ atm, and T = 1200 °C), system (Fig 3.24).

Others contributions were produced during the PhD thesis work. All the published articles during the PhD years are reported in the references paragraph and highlighted with boldface style. Despite all the results obtained there is still an open issues list. So in conclusion it can be possible to say: land ahoy! But there is still much to row...[6]

[6] It is worth noting that, even if the PhD activity covers a large aspects array of the production and characterization of the magnetoelectric multiferroic composites, it is definitely not exhaustive. Further work is still in progress and the accepted application (proposal number: 346) at the NFFA•EUROPE project will give the possibility to get free access to the infrastructures where it is possible to perform magneoeletric characterizations. The access to the best suited instruments and support competences for performing the research should give a remarkable developed of the presented work.

References

[1] N. A. Spaldin, M. Fiebig «The renaissance of magnetoelectric multiferroics» *Science* **309** (2005) 391-392.

[2] M. Fiebig «Revival of the magnetoelectric effect» *J. Phys. D: Appl. Phys.* **38** (2005) R123–R152.

[3] T. Kijima T. Aoyama, H. Miyazawa, Y. Hamada, K. Ohashi, M. Nakayama, E. Natori, T. Shimoda «Novel Si codoped $Pb(Zr,Ti,Nb)O_3$ thin film for high-density ferroelectric random access memory» *Jpn. J. Appl. Phys.***44** (2005) 267-274.

[4] J.-M. Hu, T. Nan, N. X. Sun, L.-Q. Chen «Multiferroic magnetoelectric nanostructures for novel device applications» *MRS Bull.* **40** (2015) 728-735.

[5] M. M. Vopson «Fundamentals of Multiferroic Materials and Their Possible Applications» *Crit. Rev. Solid State Mater. Sci.* **4**:40 (2015) 223-250.

[6] J. Gubbi, R. Buyya, S. Marusic, M. Palaniswami «Internet of things (IoT): A vision, architectural elements, and future directions» *Future Gener. Comp. Sy.* **29** (2013) 1645-1660.

[7] C. M. Fernández-Posada, A. Castro, J.-M. Kiat, F. Porcher, O. Peña, M. Alguero, H. Amorín. «A novel perovskite oxide chemically designed to show multiferroic phase boundary with room-temperature magnetoelectricity» *Nat. Commun.* **7**: 12772 (2016) 1–9.

[8] W. Eerenstein, N. D. Mathur, J. F. Scott «Multiferroic and magnetoelectric materials» *Nature* **442** (2006) 759–765.

[9] J. G. Wan, X. W. Wang, Y. J. Wu, M. Zeng, Y. Wang, H. Jian, W. Q. Zhou, G. H. Wang, J. H. Liu «Magnetoelectric $CoFe_2O_4$–$Pb(Zr,Ti)O_3$ composite thin films derived by a sol–gel process» *Appl. Phys. Lett.* **86** (2005) 122501–1225013.

[10] J. P. Zhou, H. C. He, Z. Shi, G. Liu, C. W. Nan «Dielectric, magnetic, and magnetoelectric properties of laminated $PbZr_{0.52}Ti_{0.48}O_3/CoFe_2O_4$ composite ceramics» *J. Appl. Phys.* **100** (2006) 094106–0941066.

[11] S. Ren, M. Wuttig «Magnetoelectric nano-$Fe_3O_4/CoFe_2O_4||PbZr_{0.53}Ti_{0.47}O_3$ composite» *Appl. Phys. Lett.* **92** (2008) 083502.

[12] S. Ren, R. M. Briber, M. Wuttig «Diblock copolymer based self-assembled nanomagnetoelectric» *Appl. Phys. Lett.* **93** (2008) 73507–73513.

[13] G. Srinivasan «Magnetoelectric composites» *Annu. Rev. Mater. Res* **40** (2010) 153-178.

[14] M. Khodaei, A. Eshghinejad, S. A. Seyyed Ebrahimi, S. Baik «Nanoscale magnetoelectric coupling study in (111)-oriented PZT-Co ferrite multiferroic nanobilayer thin film using piezo response force microscopy: Effect of Co ferrite composition» *Sens. Actuators A* **242** (2016) 92-98.

[15] X. Y. Li, J. Liu, N. Zhang «Magnetoelectric coupling by acoustic wave guide» *J. Appl. Phys.***119** (2016) 134105-5.

[16] C.-W. Nan, M. I. Bichurin, S. X. Dong, D. Viehland, G. Srinivasan «Multiferroic magnetoelectric composites: Historical perspective, status, and future directions» *J. Appl. Phys.* **103**:3 (2008) 031101.

[17] Y. Koutsawa , F. Biscani, S. Belouettar, H. Nasser, E. Carrera «Toward micromechanics of coupled fields materials containing functionally graded inhomogeneities: multi-coating approach» *Mech. Adv. Mate. Struct.* **18** (2011) 524-530.

[18] B. Patel, T. I. Zohdi «Numerical estimation of effective electromagnetic properties for design of particulate composites» *Mater. Design* **94** (2016) 546–553.

[19] P. Galizia, C. E. Ciomaga, L. Mitoseriu, C. Galassi «PZT-cobalt ferrite particulate composites: Densification and lead loss controlled by quite-fast sintering» *J. Eur. Ceram. Soc.* 37 (2017) 161–168.

[20] J. H. Peng, M. Hojamberdiev, H. Q. Li, D. L. Mao, Y.-J. Zhao, P. Liu, J. P. Zhou, G. Q. Zhu «Electrical, magnetic, and direct and converse magnetoelectric properties of $(1-x)Pb(Zr_{0.52}Ti_{0.48})O_3-(x)CoFe_2O_4$ (PZT-CFO) magnetoelectric composites» *J. Magn. Magn. Mater.* **378** (2015) 298-305.

[21] C. P. Fernández, F. L. Zabotto, D. Garcia, R. H. Kiminami «In situ sol-gelco-synthesis under controlled pH and microwave sintering of PZT/$CoFe_2O_4$ magnetoelectric composite ceramics» *Ceram. Int.* **42** (2016) 3239–3249.

[22] P. Galizia, C. Baldisserri, C. Galassi «Microstructure development in novel titania-cobalt ferrite ceramic materials» *Ceram. Int.* 42:2 A (2016) 2634-2641.

[23] C. Ponzoni, M. Cannio, R. Rosa, T. Chudoba, E. Pietrzykowka, V. Buscaglia, E. Finocchio, P. Nanni, W. Łojkowski, C. Leonelli «Effect of low-temperature high-pressure sintering on $BiFeO_3$ density, electrical magnetic and structural properties» *Phase Transitions* **86**:11 (2013) 1104–1114.

[24] F. Maglia, U. Anselmi-Tamburini, G. Chiodelli, H. E. Çamurlu, M. Dapiaggi, Z. A. Munir «Electrical, structural, and microstructural characterization of nanometric $La_{0.9}Sr_{0.1}Ga_{0.8}Mg_{0.2}O_{3-\delta}$ (LSGM) prepared by high-pressure spark plasma sintering» *Solid State Ionics* **180**:1 (2009) 36-40.

[25] S. Grasso, T. Saunders, H. Porwal, B. Milsom, A. Tudball, M. Reece «Flash Spark Plasma Sintering (FSPS) of α and β SiC» *J. Am. Ceram. Soc.* **99**:5 (2016) 1534–1543.

[26] X. X. Li, J. J. Zhou, J. X. Deng, H. Zheng, L. Zheng, P. Zheng, H. B. Qin «Synthesis of Dense, Fine-Grained YIG Ceramics by Two-Step Sintering» *J. Electron. Mater.* **45**:10 (2016) 4973-4978.

[27] X.-H. Wang, X.-Y. Deng, H.-L. Bai, H. Zhou, W.-G. Qu, L.-T. Li «Two-step sintering of ceramics with constant grain-size, II: $BaTiO_3$ and Ni-Cu-Zn ferrite» *J. Am. Ceram. Soc.* **89**:2 (2006) 438-443.

[28] M. Cologna, J. S. Francis, R. Raj «Field assisted and flash sintering of alumina and its relationship to conductivity and MgO-doping» *J. Eur. Ceram. Soc.* **31** (2011) 2827–2837.

[29] S. Grasso, Y. Sakka, N. Rendtorff, C. Hu, G. Maizza, H. Borodianska, O. Vasylkiv «Modeling of the temperature distribution of flash sintered zirconia» *J. Ceram. Soc. Jpn.* **119**:2 (2011) 144-146.

[30] R. I. Todd, E. Zapata-Solvas, R. S. Bonilla, T. Sneddon, P. R. Wilshaw «Electrical characteristics of flash sintering: thermal runaway of Joule heating» *J. Eur. Ceram. Soc.* **35** (2015) 1865–1877.

[31] P. Galizia, C. Baldisserri, C. Capiani, C. Galassi «Multiple parallel twinning overgrowth in nanostructured dense cobalt ferrite» *Mater. Design* 109 (2016) 19-26.

[32] H. Maiwa, O. Kimura, K. Shoji, H. Ochiai «Low temperature sintering of PZT ceramics without additives via an ordinary ceramic route» *J. Eur. Ceram. Soc.* **25** (2005) 2383–2385.

[33] Y. Zhou, D. Maurya, Y. Yan, G. Srinivasan, E. Quandt, S. Priya «Self-biased magnetoelectric composites: An overview and future prospectives» *Energy Harvesting and Systems* July 2015.

[34] A. R. Boccaccini, S. Keim, R. Ma, Y. Li, I. Zhitomirsky «Electrophoretic depositionof biomaterials» *J. R. Soc. Interface* **7** (2010) S581–S613.

[35] M. N. Rahaman, Ceramic Processing and Sintering, New York: Marcel Dekker, inc., 2003.

[36] M. Cernea, P. Galizia, I. V. Ciuchi , G. Aldica, V. Mihalache, L. Diamandescu, C. Galassi «$CoFe_2O_4$ magnetic ceramic derived from gel and densified by spark plasma sintering» *J. All. Comp.* 656 (2016) 854-862.

[37] M. Yoshimura «Recent developments in soft, solution processing: one step fabrication of functional double oxide films by hydrothermal–electrochemical methods» *J. Mater. Chem.* **9** (1999) 77-82.

[38] M. Yoshimura «Soft solution processing: concept and realization of direct fabrication of shaped ceramics (nano-crystals, whiskers, films, and/or patterns) in solutions without post-firing» *J. Mater. Sci*. **41** (2006) 1299.

[39] A. P. A. Oliveira, J.-F. Hochepied , F. Grillon, M.-H. Berger «Controlled Precipitation of Zinc Oxide Particles at Room Temperature» *Chem. Mater.* **15**:16 (2003) 3202–3207.

[40] C. Jeffrey Brinker, G. W. Scherer, Sol-gel Science: the Physics and Chemistry of sol-gel processing, London: Academic press, inc., 1990.

[41] Y. Cedeño-Mattei, O. Perales-Pérez, O. N. C. Uwakweh «Synthesis of high-coercivity non-stoichiometric cobalt ferrite nanocrystals: Structural and magnetic characterization» *Mater. Chem. Phys.* **132** (2012) 999-1006.

[42] A. L. Costa, G. Montanari, C. Galassi, M. Cernea, F. Bezzi, S. Albonetti «Synthesis of Nb doped lead zirconate titanate by chemical methods» *Adv. Eng. Mater.* **8**:6 (2006) 572-576.

[43] C. Baldisserri, D. Gardini, C. Galassi «A controlled colloidal destabilization approach for the electrophoretic deposition (EPD) from cobalt ferrite and magnetite nanoparticles suspensions in duethylene glycol» *Key Eng. Mater.* **507** (2012) 85-88.

[44] M. T. Buscaglia, V. Buscaglia, L. Curecheriu, P. Postolache, L. Mitoseriu, A. C. Ianculescu, B. S. Vasile, Z. Zhe, P. Nanni «Fe_2O_3@$BaTiO_3$ core-shell particles as reactive precursors or the preparation of multifunctional composites containing different magnetic phases»*Chem.Mater.***22**(2010)4740–4748.

[45] H. K. D. Reddy, Y.-S. Yun «Spinel ferrite magnetic adsorbents: Alternative future materials for water purification?» *Coord. Chem. Rev.* **315** (2016) 90-111.

[46] W. Gan, L. Gao, W. Zhang, J. Li, L. Cai, X. Zhan «Removal of oils from water surface via useful recyclable $CoFe_2O_4$/sawdust composites under magnetic field» *Mater. Design* **98** (2016) 194-200.

[47] A. Wypych, I. Bobowska, M. Tracz, A. Opasinska, S. Kadlubowski, A. Krzywania-Kaliszewska, J. Grobelny, P. Wojciechowski «Dielectric properties and characterisation of titanium dioxide obtained by different chemistry methods» *J. Nanomater.* 2014.

[48] W. Chiron, A. Fernandes-Alba, A. Rodriguez, E. Garcia-Calvo «Pesticide chemical oxidation: state-of-the-art» *Water Res.* **34** (2000) 366–377.

[49] M. A. Anderson «Applications in photocatalytic purification of air» *Stud. Surf. Sci. Catal.* **103** (1997) 445–461.

[50] D. Gumy, C. Morais, P. Bowen, C. Pulgarin, S. Giraldo, R. Hajdu, J. Kiwi «Catalytic activity of commercial of TiO_2 powders for the abatement of

the bacteria (E. coli) under solar simulated light: Influence of the isoelectric point» *Appl. Catal. B: Environ.* **63** (2006) 76-84.

[51] L. P. Argani, D. Misseroni, A. Piccolroaz, Z. Vinco, D. Capuani, D. Bigoni «Plastically-driven variation of elastic stifness in green bodies during powder compaction. Part I: Experiments and elastoplastic coupling» *J. Eur. Ceram. Soc.* **36** (2016) 2159-2167.

[52] L. P. Argani, D. Misseroni, A. Piccolroaz, D. Capuani, D. Bigoni «Plastically-driven variation of elastic stifness in green bodies during powder compaction. Part II: Micromechanical modelling» *J. Eur. Ceram. Soc.* **36** (2016) 2169-2174.

[53] E. Bosi, A. Piccolroaz, M. Gei, F. Dal Corso, A. Cocquio, D. Bigoni «Experimental investigation of the elastoplastic response of aluminium silicate spray dried powder during cold compaction» *J. Eur. Ceram. Soc.* **34** (2014) 2633-2642.

[54] S. Stupkiewicz, A. Piccolroaz, D. Bigoni «Elastoplastic coupling to model cold ceramic powder compaction» *J. Eur. Ceram. Soc.* **34** (2014) 2839-2848.

[55] R. Bjørk, V. Tikare, H. L. Frandsen, N. Pryds «The effect of particle size distributions on the microstructural evolution during sintering» *J. Am. Ceram. Soc.* **96**:1 (2013) 103-110.

[56] P. Le Brun, L. Froyen, L. Delaey «The modelling of the mechanical alloying process in a planetary ball mill: comparison between theory and in-situ observations» *Mater. Sci. Eng.* **A161** (1993) 75-82.

[57] I. Amato, L. Montanaro, Lezioni dal corso di scienza e tecnologia dei materiali ceramici, vol. II, Turin, Italy: Cortina (Torino), 1997.

[58] P. Bowen «Particle size distribution measurement from millimeters to nanometers and from rods to platelets» *J. Dispers. Sci. Technol.* **23**:5 (2007) 631–662.

[59] W. Hajjaji, S. Andrejkovicova, C. Zanelli, M. Alshaaer, M. Dondi, J. A. Labrincha, F. Rocha «Composition and technological properties of

geopolymers based on metakaolin and red mud» *Mater. Design* **52** (2013) 648-654.

[60] E. Papa, V. Medri, E. Landi, B. Ballarin, F. Miccio «Production and characterization of geopolymers based on mixed compositions of metakaolin and coal ashes» *Mater. Design* **56** (2014) 409-415.

[61] P. Palmero, A. Formia, P. Antonaci, S. Brini, J.-M. Tulliani «Geopolymer technology for application-oriented dense and lightened materials. Elaboration and characterization» *Ceram. Int.* **41**:10A (2015) 12967-12979.

[62] P. Bowen, C. Carry «From powders to sintered pieces: forming, transformations and sintering of nanostructured ceramic oxides» *Powder Technol.* **128**:2-3 (2002) 248-255.

[63] S. Grasso, Y. Sakka, G. Maizza «Electric current activated/assisted sintering (ECAS): a review of patents 1906-2008» *Sci. Technol. Adv. Mater.* **10**:5 (2009) 053001.

[64] F. Inam, H. Yan, T. Peijs, M. J. Reece «The sintering and grain growth behaviour of ceramic-carbon nanotube nanocomposites» *Compos. Sci. Technol.* **70**:6 (2010) 947-952.

[65] A. Fais, G. Maizza «Densification of AISI M2 high speed steel by means of capacitor discharge sintering (CDS)» *J. Mater. Process. Technol.* **202**:1-3 (2008) 70-75.

[66] B. Jaffe, W. R. Cook, H. Jaffe, Piezoelectric ceramics, Academic Press London and New York, 1971.

[67] C. Herring «Effect of chanbe of scale on sintering phenomina» *J. Appl. Phys.* **21** (1950) 301.

[68] A. R. Boccaccini, B. Ferrari, J. H. Dickerson, C. Galassi «Special issue: Electrophoretic deposition of ceramics» *J. Eur. Ceram. Soc.* **36** (2016) 263.

[69] A. R. Boccaccini, J. H. Dickerson, B. Ferrari, O. Van der Biest, T. Uchikoshi, Electrophoretic Deposition: Fundamentals and applications V, vol. 654, K.

E. Materials, A cura di, Pfaffikon, Switzerland: Trans Tech Publications Ltd., 2015.

[70] P. Galizia, C. Galassi «Electrophoretic deposition of bilayer based on sacrificial titanium dioxide and lead zirconate titanate on bare silicon wafer» *Key Eng. Mater.* 654 (2015) 132-135.

[71] B. Ferrari, R. Moreno «EPD kinetics: a review» *J. Eu. Ceram. Soc.* **30** (2010) 1069-1078.

[72] V. Fridkin, Ferroelectric semiconductors, Plenum Publishing Corporation, 1980.

[73] Y. Nemirovsky, A. Nemirovsky, P. Muralt, N. Setter «Design of novel thin-filmpiezoelectric accelerometer» *Sen. Actuators A* **56** (1996) 239–249.

[74] P. Glynne-Jones, S. P. Beeby, P. Dargie, T. Papakos, N. M. White «An investigation into the effect of modified firing profiles on the piezoelectric properties of thick-film PZT layers on silicon» *Meas Sci. Technol.* **11** (2000) 526–531.

[75] B. H. Toby, R. B. Von Dreele «GSAS-II: the genesis of a modern open-source all purpose crystallography software package» *J. Appl. Crystallogr.* **46** (2013) 544-549.

[76] S. Hillier «Accurate quantitative analysis of clay and other minerals in sandstones by XRD: comparison of a Rietveld and a reference intensity ratio (RIR) method and the importance of sample preparation» *Clay Miner.* **35** (2000) 291–302.

[77] F. Cordero, F. Craciun, F. Trequattrini, P. Galizia, C. Galassi «Elastic aging from coexistence and transformations of ferroelectric and antiferroelectric states in PZT» *J. Appl. Phys.* 120:6 (2016) 064104.

[78] M. Gromada, D. Gardini, P. Galizia, C. Galassi «Processing and characterization of screen printing $Ba_{0.5}Sr_{0.5}Co_{0.8}Fe_{0.2}O_{3-\delta}$ inks» *Bull. Mater. Sci.* 39:2 (2016) 559-567.

[79] R. S. Davis «Determining the magnetic properties of 1 kg mass standards» *J. Res. Natl. Inst. Stand. Technol.* **100** (1995) 209-226.

[80] P. Galizia, C. Galassi «Use of the susceptometer and data processing» CNR-ISTEC, Report N° 02/2016, 26 February 2016.

[81] H. A. Kunkel, S. Locke, B. Pikeroen «Finite-element analysis of vibrational modes in piezoelectric ceramic disks» *IEEE Trans. Ultrason., Ferroelect., Freq. Control* **37**:4 (1990) 316-328.

[82] W. S. Choi, H. Y. Chung, B. R. Yoon, S. S. Kim «Applications of grinding kinetics analysis to fine grinding characteristics of some inorganic materials using a composite grinding media by planetary ball mill» *Powder Technol.* **115** (2001) 209–214.

[83] W. Peukert «Material properties in fine grinding» *Int. J. Miner. Process.* **74S** (2004) S3-S17.

[84] B. H. Liu, J. Ding, Z. L. Dong, C. B. Boothroyd, J. H. Yin, J. B. Yi «Microstructural evolution and its influence on the magnetic properties of $CoFe_2O_4$ powders during mechanical milling» *Phys. Rev. B* **74** (2006) 184427-10.

[85] R. Becke, W. Döring, Ferromagnetismus, Berlin: Springer, 1939, p. 171.

[86] J. Garcı´a-Otero, A. J. Garcı´a-Bastida, J. Rivas «Influence of temperature on the coercive field of non-interacting fine magnetic particles» J. Magn. Magn. Mater. **189**:3 (1998,) 377–383.

[87] A. Franco, F. C. Silva «High temperature magnetic properties of cobalt ferrite nanoparticles» *Appl. Phys. Lett*. **96** (2010) 172505-3.

[88] A. Globus, P. Duplex, M. Guyot «Determination of initial magnetization curve from crystallites size and effective anisotropy field» *IEEE Trans. Magn. Magn.* **7**:3 (1971) 617–622.

[89] P. Galizia, G. Maizza, C. Galassi «Heating rate dependence of anatase to rutile transformation» *Process. Appl. Ceram.* 10:4 (2016) 235–241.

[90] S. Marinel, D. H. Choi, R. Heuguet, D. Agrawal, M. Lanagan «Broadband dielectric characterization of TiO_2 ceramics sintered through microwave and convetntional processes» *Ceram. Int.* **39** (2013) 299-306.

[91] F.-M. Meng, F. Lu, L. Xiao, Z.-Q. Sun «Influence of soaking time on nonlinear electrical behaviour and dielectric properties of TiO_2-based varistor ceramics» *J. Cent. South. Univ. Technol.* **16** (2009) 0897-0901.

[92] Z. Li, J. Wu, D. Xiao, J. Zhu, W. Wu «Colossal permittivity in titanium dioxide ceramics modified by tantalum and trivalent elements» *Acta Materialia* **103** (2016) 243–251.

[93] R. C. Pullar, S. J. Penn, X. Wang, I. M. Reaney, N. M. Alford «Dielectric loss caused by oxygen vacancies in titania ceramics» *J. Eu. Ceram. Soc.* **29** (2009) 419-424.

[94] H. Zheng, I. M. Reanev, W. E. Lee, N. Jones, H. Thomas «Effects of substitution in Nb-doped PZT ceramics» *J. Eu. Ceram. Soc.* **21** (2001) 1371-1375.

[95] G. Montanari, A. L. Costa, S. Albonetti, C. Galassi «Nb-doped PZT material by sol-gel combustion» *J. Sol-Gel Sci. Technol.* **36** (2005) 203–211.

[96] A. L. Costa, C. Galassi, E. Roncari «Direct synthesis of PMN samples by spray-drying» *J. Eu. Ceram. Soc.* **22**:13 (2002) 2093–2100.

[97] M. Cernea, G. Montanari, C. Galassi, A. L. Costa «Synthesis of La and Nb doped PZT powder by the gel-combustion method» *Nanotechnology* **17** (2006) 1731–1735.

[98] C. Galassi, E. Roncari, C. Capiani, P. Pinasco «PZT-based suspensions for tape casting» *J. Eu. Ceram. Soc.* **17** (1997) 367-371.

[99] D. Beydoun, R. Amal, G. K. C. Low, S. Mc Evoy «Novel photocatalyst: titania-coated magnetite. Activity and photo dissolution» *J. Phys. Chem. B* **104** (2000) 4387–4396.

[100] B. Brezny, A. Muan, *J. Inorg. Nucl. Chem.* **31**:3 (1969) 651.

[101] M. D. Karkhanavala, A. C. Momin, *J. Am. Ceram. Soc.* **42**:8 (1959) 400.

[102] P. Galizia, D. Gardini, S. Ortelli, C. Capiani, M. Anbinderis, R. Grigalaitis, G. Maizza, C. Galassi «Novel magnetodielectric cobalt ferrite - titania - silica ceramic composites with tunable dielectric properties» *Ceram. Int.* 42 (2016) 16650–16654.

[103] H. Su, X. Tang, H. Zhang, Y. Jing, F. Bai «Low-loss magneto-dielectric materials: approaches and developments» *J. Electron. Mater.* **43**:2 (2014) 299-307.

[104] P. Galizia, I. V. Ciuchi, M. Anbinderis, R. Grigalaitis, C. Galassi «Titania-cobalt ferrite ceramic composites for high frequency magnetic applications» IEEE-ICEAA, Turin, 2015.

[105] L. B. Kong, Z. W. Li, L. Liu, R. Huang, M. Abshinova, Z. H. Yang, C. B. Tang, P. K. Tan, C. R. Deng, S. Matitsine «Recent progress in some composite materials and structures for specific electromagnetic applications» *Int. Mater. Rev.* **58**:4 (2013) 203-259.

[106] G. A. Samara, P. S. Peercy «Pressure and temperature dependence of the static dielectric constants and Raman spectra of TiO_2 (rutile)» *Phys. Rev. B* **7**:3 (1973) 1131–1148.

[107] F. A. Harraza, R. M. Mohameda, M. M. Rashada, Y. C. Wangd, W. Sigmund «Magnetic nanocomposite based on titania–silica/cobalt ferrite for photocatalytic degradation of methylene blue dy» *Ceram. Int.* **40** (2014) 375–384.

[108] X. Gao, K. M. K. Yu, K. Y. Tam, S. C. Tsang «Colloidal stable silica encapsulated nano-magnetic composite as a novel bio-catalyst carrier» *Chem. Commun.* (2003) 2998–2999.

[109] I. J. Bruce, J. Taylor, M. Todd, M. J. Davies, E. Borioni, C. Sangregorio, T. Sen «Synthesis, characterization and application of silica-magnetite nanocomposites» *J. Magn. Magn. Mater.* **284** (2004) 145–160.

[110] C. A. Randall, N. Kim, J.-P. Kucera, W. Cao, T. R. Shrout «Intrisic and extrinsic sizeeffects in fine-grained morphotropic-phase-boundary lead zirconate titanateceramics» *J. Am. Ceram. Soc.* **81** (1998) 677–688.

[111] Z. Zhao, V. Buscaglia, M. Viviani, M. T. Buscaglia, L. Mitoseriu, A. Testino, M. Nygren, M. Johnsson, P. Nanni «Grain-size effects on the ferroelectric behaviour of dense nanocrystalline $BaTiO_3$ ceramics» *Phys. Rev. B* **70** (2004) 024107–024108.

[112] R. Stanculescu, C. E. Ciomaga, L. Padurariu, P. Galizia, N. Horchidan, C. Capiani, C. Galassi, L. Mitoseriu «Study of the role of porosity on the functional properties of (Ba,Sr)TiO_3 ceramics» *J. All. Comp.* 643 (2015) 79-87.

[113] T. Gaudisson, M. Artus, U. Acevedo, F. Herbst, S. Nowak, R. Valenzuela, S. Ammar «On the microstructural and magnetic properties of fine-grained $CoFe_2O_4$ ceramics produced by combining polyol process and spark plasma sintering» *J. Magn. Magn. Mater*. **370** (2014) 87-95.

[114] G. F. Dionne, Magnetic Oxides, Springer US, 2009, p. 253.

[115] K. Maaz, A. Mumtaz, S. K. Hasanain, A. Ceylan «Synthesis and magnetic properties of cobalt ferrite ($CoFe_2O_4$) nanoparticles prepared by wet chemical route» J. Magn. Magn. Mater. **308** (2007) 289–295.

[116] S. Singh, N. Khare «Defects/strain influenced magnetic properties and inverse of surface spin canting effect in single domain $CoFe_2O_4$ nanoparticles» Appl. Surf. Sci. **364** (2016) 783–788.

[117] Y. M. Abbas, S. A. Mansour, M. H. Ibrahim, S. E. Ali «Microstructure characterization and cation distribution of nanocrystalline cobalt ferrite» J. Magn. Magn. Mater. **323** (2011) 2748–2756.

[118] V. R. Monaji, D. Das «Influence of Zr doping on the structural, magnetic and magnetoelastic properties of cobalt-ferrites» J. All. Comp. **634** (2015) 99-103.

[119] K. Khaja Mohaideen, P. A. Joy «High magnetostriction and coupling coefficient for sintered cobalt ferrite derived from superparamagnetic nanoparticles» Appl. Phys. Lett. **101** (2012) 072405-4.

[120] O. Condurache, I. Turcan, L. Curecheriu, C. E. Ciomaga, P. Postolache, G. Ciobanu, L. Mitoseriu «Towards novel functional properties by interface reaction in mixtures of $BaTiO_3$-Fe_2O_3 composite ceramics» *Ceram. Int.* (article in press).

[121] D. Carta, M. F. Casula, A. Falqui, D. Loche, G. Mountjoy, C. Sangregorio, A. Corrias «A Structural and Magnetic Investigation of the Inversion

Degree in Ferrite Nanocrystals MFe_2O_4 (M = Mn, Co, Ni)» *J. Phys. Chem. C* **113** (2009) 8606–8615.

[122] S. Diodati, L. Pandolfo, A. Caneschi, S. Gialanella, S. Gross «Green and low temperature synthesis of nanocrystalline transition metal ferrites by simple wet chemistry routes» *Nano Research* **7**:7 (2014) 1027–1042.

[123] L. Yan, Y. Wang, J. Li, A. Pyatakov, D. Viehland «Nanogrowth twins and abnormal magnetic behavior in $CoFe_2O_4$ epitaxial thin films» *J. Appl. Phys.* **104** (2008) 123910.

[124] P. Galizia, I. V. Ciuchi, D. Gardini, C. Baldisserri, C. Galassi «Bilayer thick structures based on $CoFe_2O_4/TiO_2$ composite and niobium-doped PZT obtained by electrophoretic deposition» *J. Eur. Ceram. Soc.* 36 (2016) 373-380.

[125] E. B. Araújo, J. A. Eiras «Structural, dielectric and ferroelectric properties of Nb-doped PZT thin films produced by oxide precursor method» *Ferroelectrics* 270:1 (2001) 51–56.